

AD-A142 648

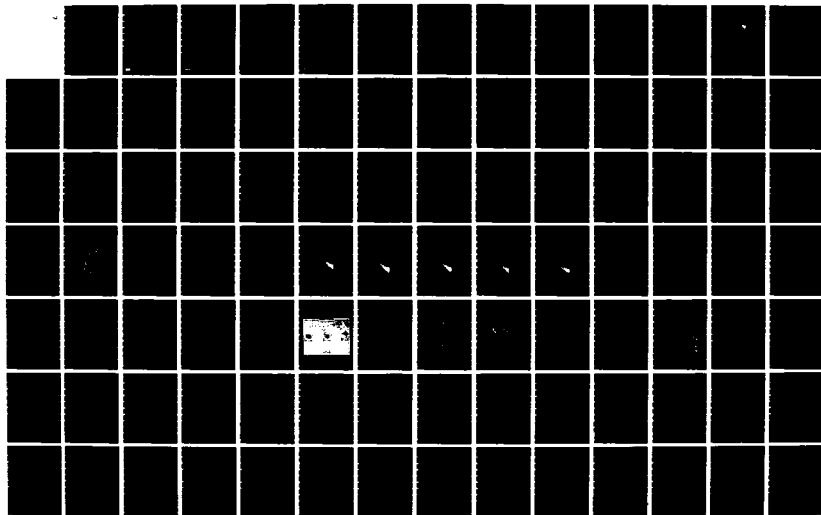
HIGH-LATITUDE IONOSPHERIC IRREGULARITIES(U) SRI  
INTERNATIONAL MENLO PARK CA J F VICKREY ET AL.  
10 MAY 84 AFOSR-TR-84-0510 F49620-83-K-0025

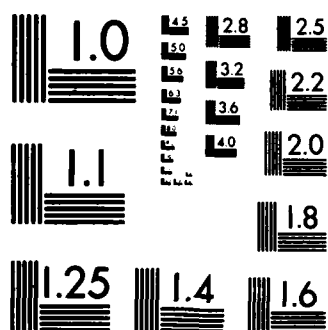
1/2

UNCLASSIFIED

F/G 4/1

NL





MICROCOPY RESOLUTION TEST CHART  
NATIONAL BUREAU OF STANDARDS-1963-A

(12)

May 1984

AD-A142 648

## HIGH-LATITUDE IONOSPHERIC IRREGULARITIES

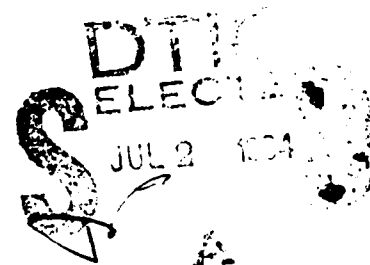
By: JAMES F. VICKREY  
NANCY B. WALKER

ROBERT M. ROBINSON  
ROBERT C. LIVINGSTON

*Prepared for:*

DEPARTMENT OF THE AIR FORCE  
AIR FORCE OFFICE OF SCIENTIFIC RESEARCH (AFOSR)  
BOLLING AIR FORCE BASE  
WASHINGTON, DC 20332  
Attention: LT. COL. TED S. CRESS

CONTRACT F49620-83-K-0025



DTIC FILE COPY



333 Ravenswood Avenue  
Menlo Park, California 94025 U.S.A.  
(415) 326-6200  
Cable: SRI INTL MPK  
TWX: 910-373-2046

Approved for public release,  
distribution unlimited

84 06 28 009

# SRI International

May 1984

## HIGH-LATITUDE IONOSPHERIC IRREGULARITIES

By: JAMES F. VICKREY  
NANCY B. WALKER

ROBERT M. ROBINSON  
ROBERT C. LIVINGSTON

*Prepared for:*

DEPARTMENT OF THE AIR FORCE  
AIR FORCE OFFICE OF SCIENTIFIC RESEARCH (AFOSR)  
BOLLING AIR FORCE BASE  
WASHINGTON, DC 20332  
Attention: LT. COL. TED S. CRESS

CONTRACT F49620-83-K-0025

SRI Project 5741

AIR FORCE OFFICE OF SCIENTIFIC RESEARCH  
NOTICE OF ACHIEVEMENT TO DIO  
115  
CHIEF, Technical Information Division

*Approved by:*

ROBERT S. LEONARD, *Director*  
*Radio Physics Laboratory*

DAVID D. ELLIOTT, *Vice President*  
*Research and Analysis Division*



333 Ravenswood Avenue • Menlo Park, California 94025 • U.S.A.  
(415) 326-6200 • Cable: SRI INTL MPK • TWX: 910-373-2046

UNCLASSIFIED

SECURITY CLASSIFICATION OF THIS PAGE (When Data Entered)

8 Dec 84

REPORT DOCUMENTATION PAGE		READ INSTRUCTIONS BEFORE COMPLETING FORM	
1. REPORT NUMBER <b>AFOSR-TR- 84-0510</b>		3. RECIPIENT'S CATALOG NUMBER	
4. TITLE (and Subtitle)  High-Latitude Ionospheric Irregularities		5. TYPE OF REPORT & PERIOD COVERED  Annual Scientific Report 03/01/83 to 29 Feb 84	
7. AUTHOR(s)  J. F. Vickrey                      R. M. Robinson R. C. Livingston                N. B. Walker		6. PERFORMING ORG. REPORT NUMBER  SRI Project 5741	
9. PERFORMING ORGANIZATION NAME AND ADDRESS SRI International 333 Ravenswood Avenue Menlo Park, California 94025		8. CONTRACT OR GRANT NUMBER(s)  F49620-83-K-0025	
11. CONTROLLING OFFICE NAME AND ADDRESS Department of the Air Force/A.F.O.S.R./AC Bolling Air Force Base Washington, DC 20332		10. PROGRAM ELEMENT, PROJECT, TASK AREA & WORK UNIT NUMBERS  61102F 2310/AD	
14. MONITORING AGENCY NAME & ADDRESS (if diff. from Controlling Office)		12. REPORT DATE 05/10/84	13. NO. OF PAGES 160
		15. SECURITY CLASS. (of this report)  Unclassified	
		15a. DECLASSIFICATION/DOWNGRADING SCHEDULE	
16. DISTRIBUTION STATEMENT (of this report)  <b>Approved for public release, distribution unlimited</b>			
17. DISTRIBUTION STATEMENT (of the abstract entered in Block 20, if different from report)			
18. SUPPLEMENTARY NOTES			
19. KEY WORDS (Continue on reverse side if necessary and identify by block number)  Ionospheric structure, scintillation, cross-field diffusion			
20. ABSTRACT (Continue on reverse side if necessary and identify by block number)  This document briefly summarizes the scientific progress made during the first year of our research on the morphology of ionospheric structure at high latitudes. Our program encompasses both theoretical and experimental investigations into this rapidly developing field. Because of the vast range of scale sizes (hundreds of kilometers to centimeters) that make up the structure, and the need for time-continuous observations, we employ a diverse set of observational techniques. These include in situ observations from rockets and			

UNCLASSIFIED

SECURITY CLASSIFICATION OF THIS PAGE (When Data Entered)

UNCLASSIFIED

SECURITY CLASSIFICATION OF THIS PAGE (When Data Entered)

19. KEY WORDS (Continued)

20 ABSTRACT (Continued)

satellites as well as radio propagation and scattering measurements. Because of the breadth of this research effort, we have provided a brief summary of the key results in the first three sections of the report. The Appendices contain the detailed results.



Accession For	
DTIC	<input checked="" type="checkbox"/>
TAR	<input type="checkbox"/>
Unrecorded	<input type="checkbox"/>
Classification	
Distribution/	
Availability Codes	
Dist	Avail and/or Special
A1	

UNCLASSIFIED

SECURITY CLASSIFICATION OF THIS PAGE (When Data Entered)

## CONTENTS

LIST OF ILLUSTRATIONS . . . . .	iv
I INTRODUCTION . . . . .	1
II F-REGION CROSS-FIELD DIFFUSION PROCESSES . . . . .	2
III HIGH-LATITUDE CONDUCTIVITY AND FIELD- ALIGNED CURRENT SYSTEMS . . . . .	7
IV CUMULATIVE LIST OF JOURNAL PUBLICATIONS PRODUCED UNDER SUPPORT FROM THIS CONTRACT . . . . .	10
A. Journal Publications . . . . .	10
B. Manuscripts in Preparation . . . . .	11
REFERENCES . . . . .	12
APPENDICES:	
A. Low-Altitude Image Striations Associated with Bottomside Equatorial Spread F--Observations and Theory . . . . .	A-1
B. Irregularity Decay in an Isolated Plasma Bubble . . . . .	B-1
C. Electrical Coupling Effects on the Temporal Evolution of F-Layer Plasma Structure . . . . .	C-1
D. Aurora and Electrojet Configuration in the Early Morning Sector . . . . .	D-1
E. Auroral Zone Conductivities Within the Field-Aligned Current Sheets . . . . . <i>848 p</i> . . . . .	E-1
F. $K_p$ Dependence of Auroral Zone Field-Aligned Current Intensity . . . . .	F-1

## ILLUSTRATIONS

1. Empirically Derived, Scale-Size Dependent  
Diffusion Rate Based on the Observations  
of Livingston et al. (Appendix B) . . . . . 4
2. Comparison on in situ Observations and  
Theoretically Derived Image Irregularity  
Spectra (from Vickrey et al., Appendix A) . . . . . 5
3. The Limiting Pedersen Current in the  
Ionosphere as a Function of  $K_p$  . . . . . 9



## I INTRODUCTION

Under support from the Air Force Office of Scientific Research, we have begun a broad-based program of research into the origin, lifetime, and redistribution by convection of ionospheric structure at high latitudes. Structure in plasma concentration ranging from scale sizes of hundreds of kilometers to meters is commonplace at high latitudes and has a variety of sources [Vickrey and Kelley, 1983].\* The amplitude of ionospheric irregularities observed at any point is a strong function of the local electrodynamics (including convection speed and velocity structure, field-aligned currents, and conductivity) as well as the history of the convecting flux tubes to which the structure is tied. Thus, our research program is by necessity rather diverse.

Our ultimate goal is to develop an accurate predictive physical model of ionospheric structure at high latitudes. Such a model would benefit the Air Force because ionospheric structure affects radio signals and degrades Air Force communications and surveillance systems. Although the framework for such a model exists [Vickrey and Kelley, 1983], our present understanding does not even include knowledge of which magnetospheric processes affect structure at different scale sizes most. Our present efforts are aimed at identifying these processes.

This report is organized as follows: Section II describes recent observations and theory of the diffusion processes that ultimately remove plasma structure. Section III contains the results of an attempt to better specify the ionospheric electrodynamic environment in different time sectors and magnetic activity levels. Section IV is a list of journal publications produced under this contract; the Appendices A through F contain those publications.

---

\*References not included as appendices are listed at the end of this report.

## II F-REGION CROSS-FIELD DIFFUSION PROCESSES

The ultimate spectrum of fluctuations in plasma concentration that is observed experimentally is a balance between the strength and scale size dependencies of the structure sources and sinks. The sources of plasma structure at high latitudes are many, and their scale-size dependence is largely unknown. We have begun, therefore, to examine this balance through the scale-size dependence of this structure removal process--cross field diffusion. Our hope is that through accurate modelling of diffusion, comparisons of observations with models will help reveal the more complicated (presumably) scale-size dependencies of the source mechanisms. Our modelling has shown that a scale-size dependent cross-field diffusion rate is a natural consequence of magnetic field line coupling to the E layer.

The effects of E-region conductivity on the cross-field diffusion of plasma gradients in the F-region has been studied by Vickrey and Kelley [1982]. They showed that for an insulating E region, F-region diffusion may only proceed at the electron rate, but that the diffusion rate increases as the E-region conductivity increases. In a perfectly conducting E-region, F-region diffusion proceeds at the ion rate. Their analysis did not consider, however, any scale-size dependence to the diffusion rate  $D_{\perp}$ .

The first indication that  $D_{\perp}$  was, indeed, a function of scale size came from the work of Livingston et al. [1984] (Appendix B). They presented complex signal scintillation observations through an isolated and decaying equatorial plasma bubble. Multiple scans through the bubble made from the Air Force Geophysics Laboratory (AFGL) Airborne Ionospheric Observatory, showed evolution of irregularity energy over a broad range of scale sizes. At wavelengths larger than about 4 km, the energy remained nearly constant with time. At shorter scale sizes, the spectrum maintained an approximate power law form ( $f^{-n}$ ) and  $n$  increased with time.

This behavior suggests that the cross-field diffusion rate in the F region depends on scale size. Figure 1 shows the empirically derived diffusion rate based on their measurements.

In parallel with these efforts, Vickrey et al. [1984] (Appendix A), have investigated the production of "image" plasma density irregularities in the E region caused by the polarization electric fields associated with F-layer structure. They showed that the image formation process preferentially produces E-region structure at kilometer scales. Their theoretical power spectrum was in good agreement with near equatorial rocket observations. A comparison between the observations of images and theory is shown in Figure 2.

The situation modelled by Vickrey et al. [1984] was driven, not purely decaying as would be appropriate for comparison to the Livingston et al. [1984] observations. Nevertheless, Vickrey et al. [1984], argued that image striations would also be produced in the nondriven case. Moreover, because the image structure grows at the expense of F layer plasma, the image spectrum should reflect the scale-size dependence of the effective diffusion rate in the F layer. Thus, their model could explain, at least qualitatively, the observations of Livingston et al. [1984].

This encouraging agreement led Heelis et al. [1984] (Appendix C) to develop a fully time-dependent model of a decaying F-region irregularity spectrum that includes magnetic field line coupling to an E-region plasma.

This modelling effort is showing that the E region can produce fundamental changes in the temporal evolution of F layer structure that were not anticipated by Vickrey and Kelley [1982] or Vickrey et al. [1984]. For example, the classical effect on the F-region spectrum expected from diffusion, classical or anomalous, is to increase the slope of the F-region spectrum at all scale sizes with increasing time. The model of Heelis et al. [1984] shows, however, that when the E-region ion concentration is low, image amplitude  $\Delta N^E/N_O^E$  saturates at a value determined by the amplitude of the F-layer driving structure and the temperatures in the two regions. When this occurs, the E- and F-region spectral

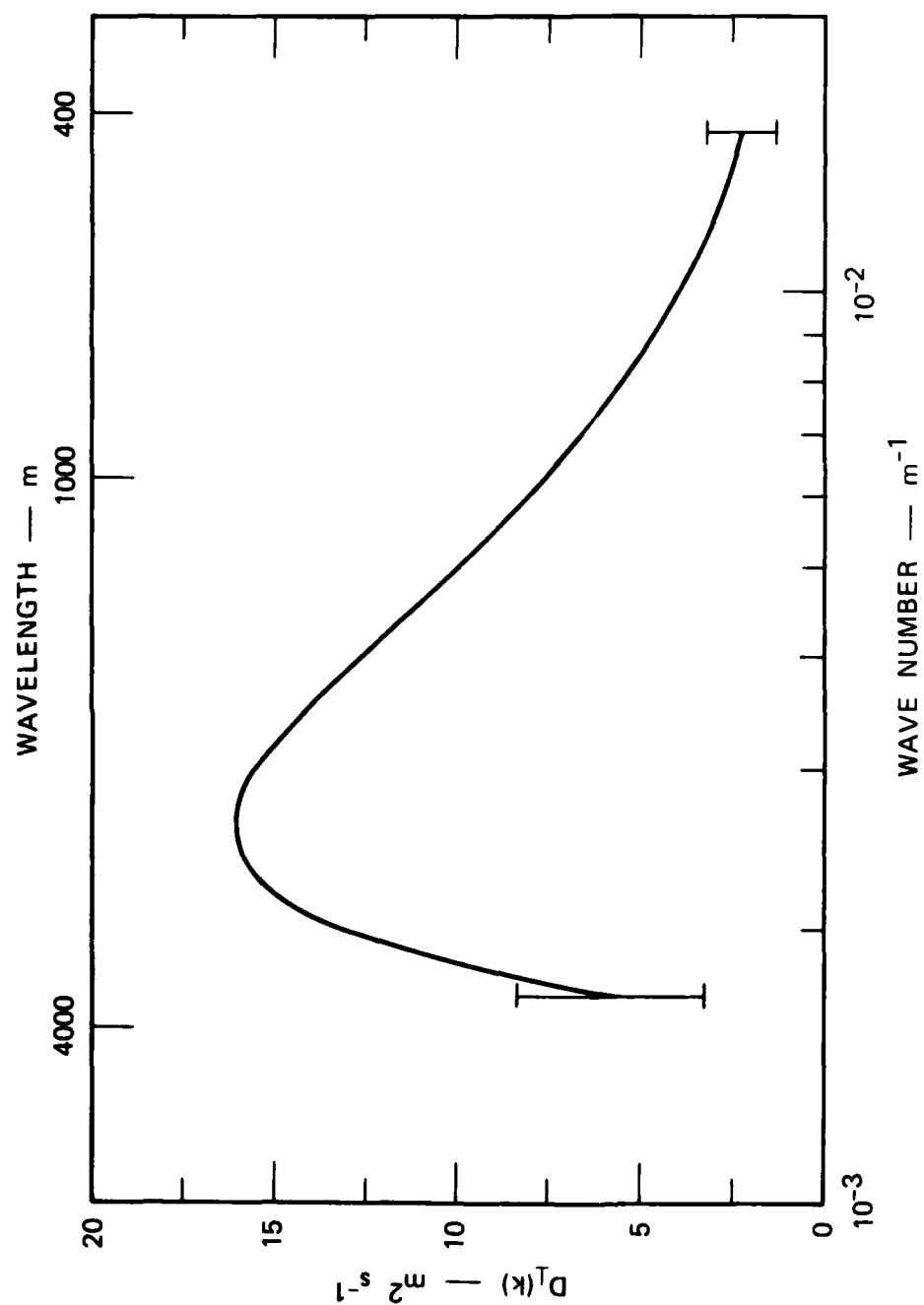


FIGURE 1 EMPIRICALLY DERIVED, SCALE-SIZE DEPENDENT DIFFUSION RATE BASED ON THE OBSERVATIONS OF LIVINGSTON et al. (APPENDIX B)

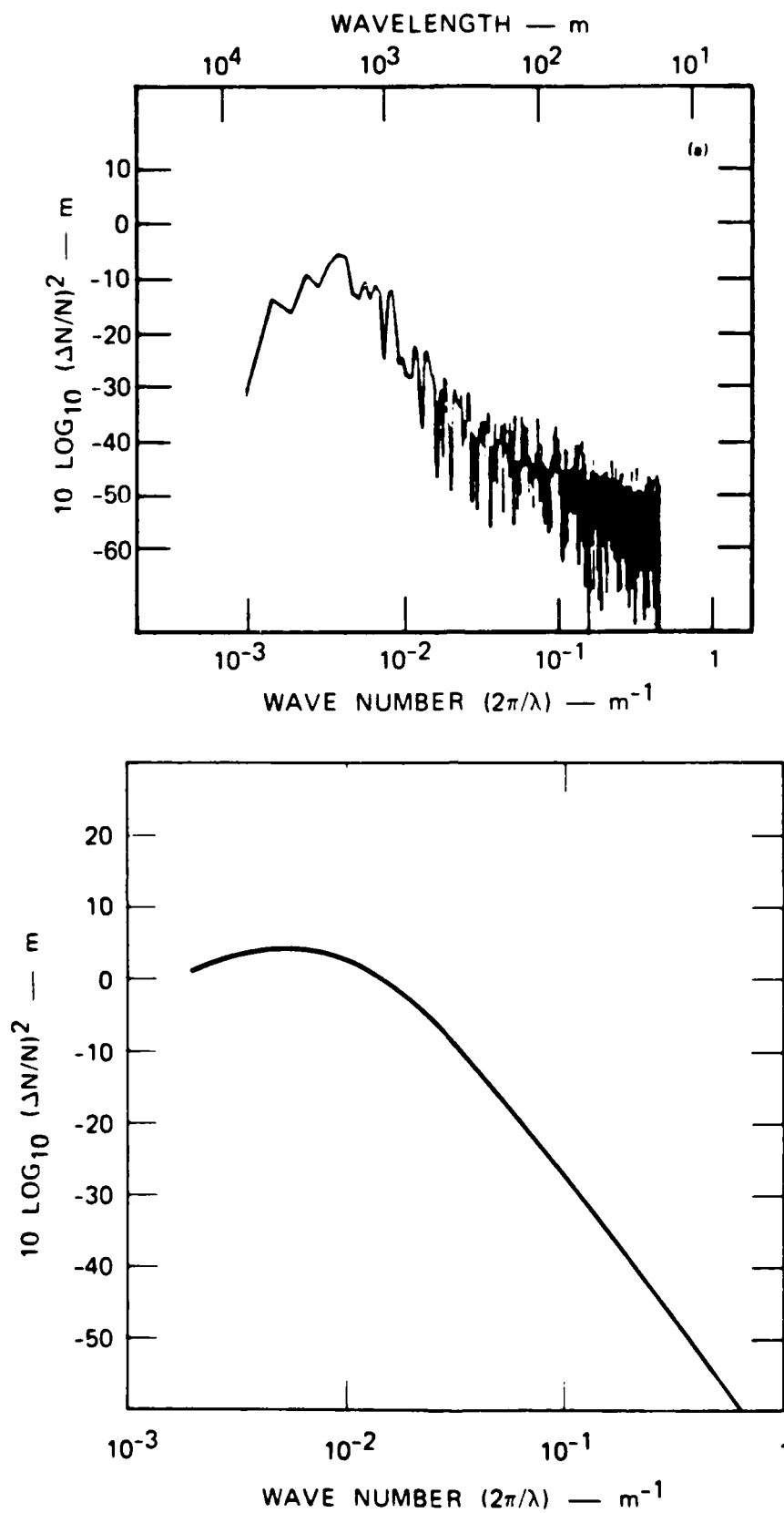


FIGURE 2 COMPARISON ON IN SITU OBSERVATIONS AND THEORETICALLY DERIVED IMAGE IRREGULARITY SPECTRA (FROM VICKREY et al., APPENDIX A)

shapes differ only by a multiplicative constant. Moreover, they decay in amplitude at a rate that is nearly independent of scale size and hence, their common spectral form is retained. The decay rate in this situation is a simple function of the chemical recombination rate in the E layer. This saturated condition may be routinely achieved in the winter polar cap, in equatorial spread F, and perhaps in barium clouds.

### III HIGH-LATITUDE CONDUCTIVITY AND FIELD-ALIGNED CURRENT SYSTEMS

Strong sources of structured F-region plasma at high latitudes include the  $\vec{E} \times \vec{B}$  and current convective instabilities that are driven by the convection electric field and magnetic-field-aligned currents. In addition to influencing the lifetime of structure, the E region can be a strong damper of these instabilities. Thus, the morphological relationship between the conductivity pattern and current systems is important for understanding the distribution of high-latitude plasma structure.

Robinson et al. [1984] (Appendix E), have examined the relationship between field-aligned current and conductivity in the morning- and evening-sector Region 2 current sheet and in the evening-sector Region 1 current sheet. They found little correlation between the field-aligned current density and conductivity along the same flux tube. The direction of the field-aligned current, however, does influence the conductance in that upward currents favor the formation of parallel potential drops and hence, auroral arcs.

Of interest from a structure point of view is the fact that only in the morning-sector Region 2 current sheet do the energetic electrons carry a large fraction of the upward current. Also, the parallel current in auroral arcs is often too large to be carried by precipitating electrons alone. The significance of this is that only that portion of the total field aligned current that is carried by thermal particles is destabilizing to the current convective instability. Thus, except for the morning-sector Region 2, magnetometer measurements of the magnitude of  $j_{\parallel}$  can be used to calculate the growth rate of the current convective instabilities.

The relationships between field aligned currents, electric fields, and conductivities in the morning sector auroral zone have received relatively little attention in comparison to the evening sector. Kamide et al. [1984] (Appendix D) have examined the electric field, current, and

conductivity patterns as well as visible aurora in the early morning sector. They found, in agreement with Kamide and Vickrey [1983] that the westward electrojet has a dual character depending on latitude in that local-time sector. Namely, the dominant contributor to the amplitude of the westward electrojet in its poleward half is a relatively intense southward electric field. In the equatorward half, high Hall conductivity associated with bright visible aurora dominated the electrojet amplitude. This has the interesting implication that only the equatorward half of the westward "auroral" electrojet is actually associated with visible aurora. In terms of structure morphology, we would expect relatively more structure in the poleward half of the electrojet because the driver  $E_{\text{south}}$  is large and the damping by E-region conductivity is low.

We have noted above that (1) the ultimate goal of structure modelling is to construct a physical, predictive model of structure morphology and (2) that field-aligned currents can be a strong source of structure. A key input to such a model, then, is the dependence of field-aligned current intensity on magnetic activity. Using a simple model for the closure of field-aligned currents by meridional Pedersen currents, Robinson [1984] (Appendix F) has derived an empirical relationship between the global field-aligned current intensity,  $J_o$  and the  $K_p$  index:

$$J_o \text{ (A/km)} = 97 + 71 \times K_p \quad (1)$$

Making use of the correlation between  $K_p$  and the polar cap potential drop,  $\phi_o$ , given by Reiff et al. [1981],  $J_o$  can be related to  $\phi_o$ :

$$J_o \text{ (A/km)} = 6.5 \times \phi_o - 90 \quad (2)$$

These relationships are illustrated in Figure 3. Robinson further shows that these expressions can be used to show that the maximum ionospheric Joule heating rate increases as the square of the polar cap potential provided  $\phi_o \gg 15$  kV.



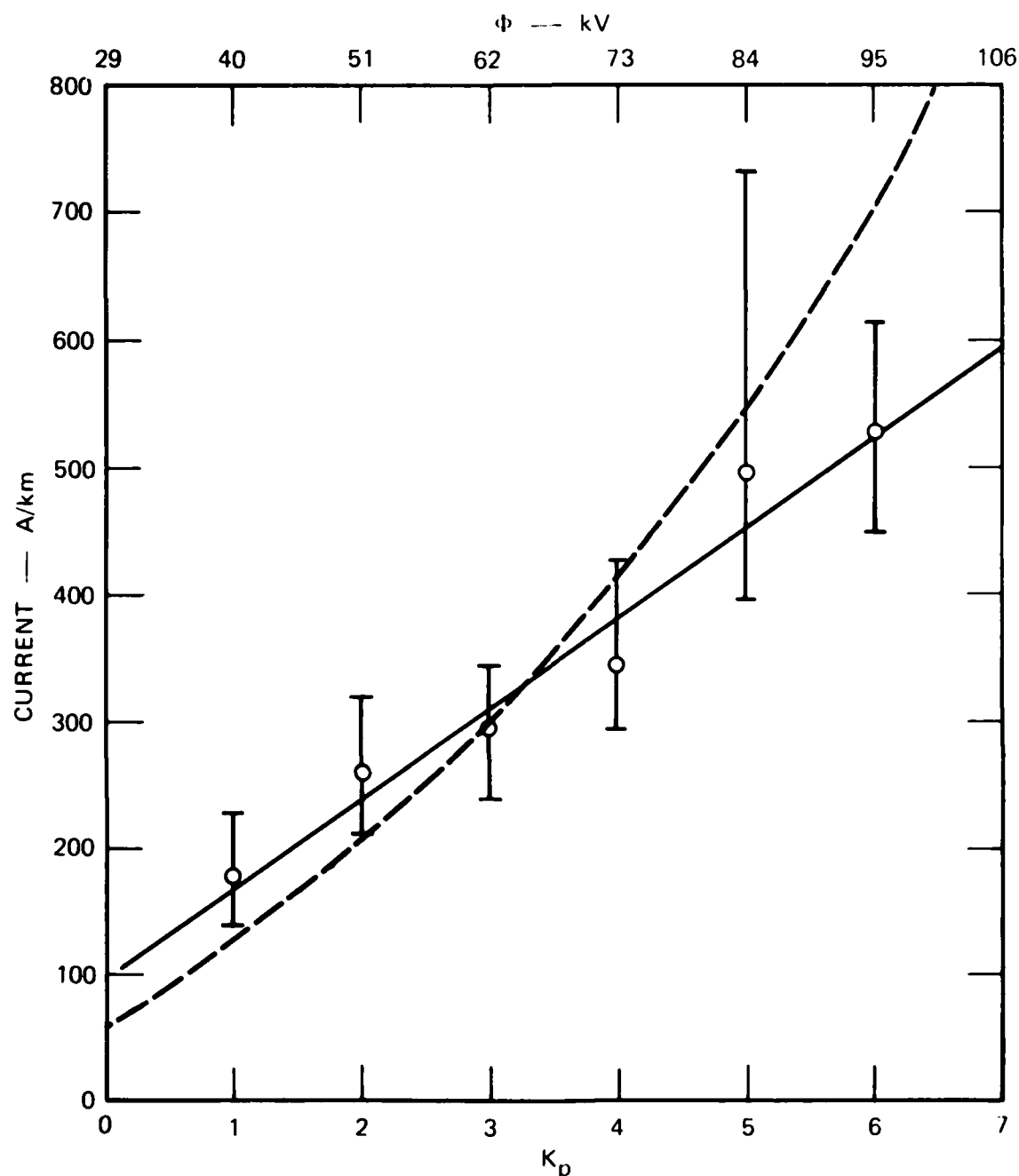


FIGURE 3 THE LIMITING PEDERSEN CURRENT IN THE IONOSPHERE AS A FUNCTION OF  $K_p$ . The upper scale shows the value of the polar cap potential drop as deduced by Reiff et al. [1981]. The straight line is a weighted, linear least-squares fit to the six data points. The dashed curve represents a quadratic dependence of current on potential drop forced to agree for  $K_p = 3$ .

IV CUMULATIVE LIST OF JOURNAL PUBLICATIONS PRODUCED  
UNDER SUPPORT FROM THIS CONTRACT

A. Journal Publications

Copies or reprints of the papers discussed in the text are contained in Appendices A through F.

Vickrey, J. F., M. C. Kelley, R. Pfaff, and S. R. Goldman, "Low Altitude Image Striations Associated with Bottomside Equatorial Spread F-- Observations and Theory," in press, J. Geophys. Res., 1984.

Livingston, R. C., J. F. Vickrey, M. C. Kelley, E. J. Weber, and J. Buchau, "Irregularity Decay in an Isolated Plasma Bubble," Submitted for publication, J. Geophys. Res., 1984.

Heelis, R. A., J. F. Vickrey, and N. B. Walker, "Electrical Coupling Effects on the Temporal Evolution of F-Layer Plasma Structure," Submitted for publication, J. Geophys. Res., 1984.

Kamide, Y., R. M. Robinson, S.-I. Akasofu, and T. A. Potemra, "Auroral and Electrojet Configuration in the Early-Morning Sector," J. Geophys. Res., 89, A1, 389-393, 1984.

Robinson, R. M., R. R. Vondrak, and T. A. Potemra, "Auroral-Zone Conductivities Within the Field-Aligned Current Sheets," submitted for publication, J. Geophys. Res., 1984.

Robinson, R. M., " $K_p$  Dependence of Auroral Zone Field-Aligned Current Intensity," J. Geophys. Res., 89, A3, 1743-1748, 1984.

Rino, C. L., R. C. Livingston, R. T. Tsunoda, R. M. Robinson, J. F. Vickrey, C. Senior, M. D. Cousins, J. Owen, and J. A. Klobuchar, "Recent Studies of the Structure and Morphology of Auroral Zone F-Region Irregularities," Radio Sci., 18, 6, 1167-1180, 1983.

B. Manuscripts in Preparation

Kelly, J. D., and J. F. Vickrey, "Radar Measurements of the F-Region Ionization Structure Associated with Antisunward Flow Near the Dayside Polar Cusp," to be submitted, Geophys. Res. Letts., 1984.

Robinson, R. M., T. A. Potemra, D. S. Evans, and J. D. Kelly, "Radar and Satellite Measurements of an F-Region Ionization Enhancement in the Post-Noon Sector," to be Submitted, J. Geophys. Res., 1984.

#### REFERENCES

- Kamide, Y., and J. F. Vickrey, "Relative Contribution of Ionospheric Conductivity and Electric Field to the Auroral Electrojets," J. Geophys. Res., 88, A10, 7989-7996, 1983.
- Reiff, P. H., R. W. Spiro, and T. W. Hill, "Dependence of Polar Cap Potential Drop on Interplanetary Parameters," J. Geophys. Res., 86, 7639-7648, 1981.
- Vickrey, J. F. and M. C. Kelley, "The Effects of a Conducting E Layer on Classical F-Region Cross-Field Plasma Diffusion," J. Geophys. Res., 87, A6, 4461-4468, 1982.
- Vickrey, J. F. and M. C. Kelley, "Irregularities and Instabilities in the Auroral F Region," in High-Latitude Space Plasma Physics, Edited by B. Hultqvist and T. Hagfors, (Plenum Publishing Corp.) 1983.

APPENDIX A

LOW-ALTITUDE IMAGE STRIATIONS ASSOCIATED WITH  
BOTTOMSIDE EQUATORIAL SPREAD F -- OBSERVATIONS AND THEORY

by

James F. Vickrey  
SRI International  
Radio Physics Laboratory  
Menlo Park, CA 94025

Michael C. Kelley and Robert Pfaff  
Cornell University  
School of Electrical Engineering  
Ithaca, New York 14853

S. Robert Goldman  
Los Alamos National Laboratory  
Los Alamos, New Mexico 87545

## ABSTRACT

Ionospheric plasma instabilities are usually discussed in terms of local parameters. However, because electric fields of scale size  $\lambda \gtrsim 1$  km map along magnetic field lines, plasma populations far away from a locally unstable region may be affected by the instability process and vice-versa. We present observations of electron density variations in the  $F_1$  region of the ionosphere at two locations near the magnetic equator. Oscillations in electron number density that were confined to a narrow wavelength regime were observed in a region of the ionosphere with a very weak vertical density gradient. Since magnetic flux tube interchange instabilities cannot create structure in such an environment we suggest that these are "images" of instabilities occurring elsewhere along the magnetic field line. A simple steady state theory of image formation is developed which is in good agreement with the observations. Moreover, this theory predicts a scale-size dependent "effective-diffusion" process in the F region which may dominate over classical cross-field diffusion at kilometer scale sizes. Such a scale-size dependent diffusion process is required to explain recent scintillation observations of decaying equatorial plumes.

## I INTRODUCTION

Ionospheric plasma instabilities are often discussed in terms of local parameters. However, magnetic field lines can link unstable regions to other plasma populations that may affect the evolution of the instability process. An example is the role of a conducting E region in diffusive damping of F-region structure and in the suppression of electrostatic instabilities [Volk and Haerendel, 1971; Goldman et al., 1976; Vickrey and Kelley, 1982].

Another effect most often studied in conjunction with F-region barium-cloud striations is the generation of image striations in the background medium. As discussed in more detail below, an image forms at altitudes where the ion gas is compressible, namely, the E and lower  $F_1$  regions. To date the existence of images has not been experimentally verified although computer simulations have predicted their generation [Goldman et al., 1976; Lloyd and Haerendel, 1973].

The data discussed here come from fixed bias Langmuir probes flown on two rockets launched just off the magnetic equator during equatorial spread F conditions. One, a Javalin sounding rocket, was launched by NASA from Natal, Brazil, on 18 November 1973 at 2122 UT [Kelley et al., 1976, 1979a; Costa and Kelley, 1978]. The second, a Terrier-Malemute designated as PLUMEX I, was launched by the Defense Nuclear Agency from Kwajalein Atoll on 17 July 1979 at 1233 UT [Szuszczewicz et al., 1980; Rino et al., 1981; Kelley et al., 1982]. We will show that the spectrum of density



structure observed in the  $F_1$ -layer valley (160 to 200 km altitude) off the magnetic equator is consistent with that expected from the image formation process (which depends on scale length and density) driven by the gravitational Rayleigh-Taylor instability operating on the bottomside F layer at the equator itself.

## II DATA PRESENTATION

A plasma density profile from the downleg of the Natal rocket flight is reproduced in Figure 1(a) with an expanded plot of the F-layer valley and E-region density profiles in Figure 1(b) (upleg data is not available in these flights in the low altitude region due to the timing of sensor deployment). The plasma density profile was extremely structured throughout the flight. Near and just below the F-region peak, the turbulence has been interpreted in terms of the non-linear gravitational Rayleigh-Taylor instability [see earlier references]. The low-altitude layered (90 to 130 km) structure is typical of the equatorial E region and is not produced by the "image" process. Of interest to the present study are the quasi-sinusoidal fluctuations in the  $F_1$ -layer valley (170 to 200 km) where the local zero-order vertical plasma density gradient nearly vanishes. Because of the finite dip angle at Natal, these fluctuations project along magnetic field lines to the magnetic equator at heights ranging from 280 to 315 km. Note that this altitude range corresponds to heights where the local equatorial F region is suspected to be unstable to the gravitational Rayleigh-Taylor process. The geometry is illustrated schematically in Figure 2. Of course, we do not have simultaneous F region observations directly at the equator but it is highly likely that bottomside spread-F was occurring there also.

Another example from the PLUMEX I rocket downleg is presented in Figure 3. Again, quasi-sinusoidal oscillations were observed in the  $F_1$ -layer valley region at heights that map to the magnetic equator in the altitude range at which the local equatorial spread F fluctuations were detected. The detector used in the present study was not deployed during the upleg of PLUMEX I. However, Narcisi and Szuszczewicz [1981] have presented profiles from the upleg and from PLUMEX II. Although some variations in density exist in the "valley," a strong quasi-sinusoidal signal was not present. Concerning rocket flights nearly on the magnetic equator, the Equion [Morse et al., 1977] rocket did not detect such fluctuations nor did two flights from India [Prakash, private communication, 1982], nor the more recent launches (2) from Peru [Kelley, private communication, 1983]. Thus, two out of four of the available off-equatorial rocket data sets have shown sinusoidal structures in the valley region while four on-equator flights did not.

A series of spectra corresponding to different altitude ranges from Figure 1 are presented in Figures 4 and 5. The Figure 4 spectra all correspond to bottomside equatorial spread F. The spectrum from the lowest altitude displays a form that varies as  $k^{-2}$  over the regime from  $\lambda = 5000$  m to  $\lambda = 50$  m, where the instrument noise level was reached. The highest altitude spectrum seems to have a somewhat shallower spectral form at the long wavelengths (500 to 5000 m). These results are in good agreement with the PLUMEX I results reported by Rino et al., [1981] and Kelley et al. [1982] as well as a number of others [see Fejer and Kelley, 1980 for references].

The  $F_1$ -layer valley spectra in Figure 5 are quite different from those in Figure 4, as are the waveforms. The spectra are peaked at wavelengths of 700 to 1400 m as one would expect from the sinusoidal nature of the waveforms. We show in the next section that such a peak in the spectra is consistent with the image formation process.

### III ANALYSIS

#### A. The F-Layer Gravitational Rayleigh-Taylor Instability:

##### A Source for the Structures

The mechanisms whereby plasma irregularities are formed in the F-layer ionosphere can be studied by considering the continuity equation:

$$\frac{\partial n^F}{\partial t} + \nabla \cdot (n^F \underline{v}) = P - L \quad (1)$$

where  $n$  is the electron density,  $\underline{v}$  is the flow velocity,  $P$  the production rate and  $L$  the loss rate. In the nighttime F layer, the latter two terms can be ignored yielding

$$\frac{\partial n^F}{\partial t} + \underline{v} \cdot \nabla n^F + n^F (\nabla \cdot \underline{v}) = 0 \quad (2)$$

Ignoring variations along the direction of the magnetic field, the ion velocity in the F region is given by  $\underline{E} \times \underline{B}/B^2$ , which is divergence free, and thus

$$\frac{\partial n^F}{\partial t} = - \underline{v} \cdot \nabla n^F \quad (3)$$

In effect, the irregularities are formed by incompressibly mixing an existing background density gradient by means of the perturbation electric fields generated in the instability process. These processes are reasonably well understood and well documented [see recent reviews by Fejer and Kelley, (1980) and Ossakow (1981)]. For our purposes here, we need only describe the perturbation electric field (or equivalent velocity) structure in the unstable F layer because it is this structure that maps to lower altitudes and drives the image process.

It can be shown from nonlinear Rayleigh-Taylor instability theory with no zero order zonal electric field [Keskinen and Ossakow, 1981], that the electric-field and density fluctuations are related by

$$\delta E = \frac{gB}{v_{in}^F} \left[ \frac{\delta n}{n} \right]^F \quad (4)$$

where  $g$  is gravitational acceleration,  $B$  is the magnetic-field strength,  $v_{in}^F$  is the ion-neutral collision frequency, and  $\left[ \frac{\delta n}{n} \right]^F$  are density fluctuations such as those whose spectra are shown in Figure 3. Thus, the velocity turbulence that drives image formation can be specified in terms of our measurements of the density fluctuations. Our goal then is to show that the spectrum of image irregularities observed is the result of a balance between this driver, which depends on scale size, and the image formation and diffusive damping processes, which are also scale size dependent.

Note that the Rayleigh-Taylor process operating on the same magnetic field line will not create local structure in the F-layer valley if the zero-order density gradient vanishes. The electric field will still map to the region where density structure is observed, but with no density gradient the stirring will not produce structured density. In fact, to first order in the small parameter  $(v_i/\Omega_i)$  the flux tube in the valley will also drift rigidly attached to the F layer source. Thus we can perform our analysis in a frame moving with the flux tube.

#### B. The Image Formation Process

To understand the formation of images, we must examine a more complicated version of the continuity equation. As will be discussed in more detail below, images form at altitudes where the incompressibility assumption utilized above breaks down. Compressibility arises from non-negligible Pedersen drifts  $\left(v_p = \frac{\sigma_p}{nq} E\right)$ , which must be added to the  $\bar{E} \times \bar{B}$  flow considered above. Here  $\sigma_p$  is the Pedersen conductivity, which for E and F<sub>1</sub> layer heights, is given by

$$\sigma_p = \frac{nq^2 v_{in}^E}{m_i \Omega_i^2} \quad (5)$$

where  $q$  is the electron charge;  $m_i$  and  $\Omega_i$  are the ion mass and gyrofrequency, respectively, and  $v_{in}^E$  is the ion neutral collision frequency at the image altitude. Throughout the following, the superscript E denotes

quantities at the image altitude even though we are concentrating principally on the  $F_1$ -layer valley region. Additional complications to the continuity equation include the effects of relatively rapid cross-field plasma diffusion and chemical recombination. If we include these effects, Equation (2) becomes

$$\frac{\partial n^E}{\partial t} + \left( \frac{\bar{g}}{v_{in}^E} + \frac{\bar{E} \times \bar{B}}{B^2} \right) \cdot \nabla_z n_o^E - n_o^E \frac{q v_{in}^E}{m_i \Omega_i^E} \nabla \cdot \bar{E} - D_{\perp} \nabla_{\perp}^2 n^E - \alpha n_o^E{}^2 = 0 \quad (6)$$

where we have ignored any horizontal variation in electron density but have, for completeness, included a vertical gradient term, which is weak in the valley region.  $D_{\perp}$  is the cross-field plasma diffusion rate and  $\alpha$  is the effective recombination coefficient. In this expression  $\bar{E}$  represents the sum of a possible zero-order electric field  $\bar{E}_0$  and the electric field  $\delta E$  due to the Rayleigh-Taylor process operating at the dip equator. The second term in Equation (6) vanishes if the local density gradient does. In our two examples the smallest value for  $L = \left( \frac{1}{n} \frac{dn_o^E}{dz} \right)^{-1}$  was 60 km. Thus, if we calculate the growth rates of the local Rayleigh-Taylor instability ( $g/v_{in}^E L$ ) or the  $\bar{E} \times \bar{B}$  instability ( $E_0/B L$ ) we find  $\gamma = 8 \times 10^{-5} s$  and  $2.5 \times 10^{-4}$  respectively, where we have taken  $E_0/B = 15$  m/s upward as observed during the Natal flight. These values are quite small and hence, we are justified in neglecting these local instability mechanisms. (Note, moreover, that during the PLUMEX I flight the ionosphere was descending and thus, was stable on the bottomside to the  $\bar{E} \times \bar{B}$  process.)



We now consider the effect of a finite driving electric field,  $\delta E$ , on the  $F_1$ -layer plasma, where  $\delta E$  is due to a fully developed plasma instability on the same magnetic field lines. For the moment we ignore the question of the mapping efficiency of the electric field; we will return later to discuss the effect of finite parallel resistivity. To proceed we partition  $k$  space into equal intervals of width  $\Delta k$  which we choose to be smaller than the bandwidth of the spectral peaks in Figures 5(a) and 5(b). Using Equation (4) the magnitude of the driving electric field at some value of  $k_0$  is thus

$$\delta E(k_0) = \frac{gB}{v_F^{\text{in}}} \left[ \int_{k_0 - \Delta k/2}^{k_0 + \Delta k/2} P^2(k) dk \right]^{1/2} = \frac{gB}{v_F^{\text{in}}} \frac{\delta n^F}{n} (k_0, \Delta k) \quad (7)$$

where  $P^2(k)$  is the power spectrum of the density fluctuations  $\left[ \frac{\delta n^F}{n} \right]^2(k)$ . As shown in Figure 3, the power spectrum is well represented by the an equation of the form

$$P^2(k) = \frac{1}{1 + (k/k_c)^2} (m) \quad (8)$$

The dashed line corresponds to  $k_c \approx 3 \times 10^{-3} \text{ m}^{-1}$ . Recall that we do not know the actual  $P^2(k)$  at the source since the rockets necessarily detected the local (off-equatorial) bottomside spread-F spectrum. Nonetheless Equation (8) is a reasonably good approximation to all of the reported bottomside spread-F spectra (e.g., Morse et al., 1977; Kelley et al., 1979). Now, if we consider the process to be in a steady state ( $\partial n^E / \partial t = 0$ ), we can calculate the amplitude of an image structure at wavenumber  $k$ ,

$$+ n_o^E \frac{q v_{in}^E}{m_i \Omega_i^E} \frac{k g B}{v_{in}^F} \left\{ \frac{\delta n^F}{n} (k, \Delta k) \right\} - k^2 D_{\perp} n_1^E - 2 \alpha n_o^E n_1^E = 0 \quad (9)$$

We have expressed the local density in the low altitude region in terms of a zero order part and a fluctuating part  $n^E = n_o^E + n_1^E$  and we assume  $n_1^E \ll n_o^E$ . Solving for the local density fluctuation yields

$$\left| \frac{n_1^E}{n_o^E} \right| = \left( \frac{v_{in}^E}{\Omega_i^E} \right) \left( \frac{g}{v_{in}^F} \right) k \frac{\frac{\delta n^F}{n} (k, \Delta k)}{(k^2 D_{\perp} + 2 \alpha n_o^E)} \quad (10)$$

Before analyzing this result we should question the steady state assumption. It seems reasonable that if the growth rate of driven images is comparable to the Rayleigh-Taylor process itself, then observed saturated F region structures ( $\delta n/n \approx$  tens of percent) should be associated with saturated images. The Rayleigh-Taylor growth rate is given by  $g/v_{in}^F L_F$ , where  $L_F$  is the vertical density gradient on the bottomside of the F layer. The ratio of image to Rayleigh-Taylor growth rates deduced from Equation (6) is thus

$$R = \frac{\gamma_{image}}{\gamma_{RT}} = \frac{k \left( \frac{v_{in}^E}{\Omega_i^E} \right) \left( \frac{g}{v_{in}^F} \right) \left( \frac{\delta n^F}{n} (k, \Delta k) \right)}{\left( \frac{g}{v_{in}^F} \right) \left( \frac{1}{L_F} \right)} \quad (11)$$

where

$$\frac{\delta n^F}{n}(k, \Delta k) = \left[ \int_{k_o - \Delta k/2}^{k_o + \Delta k/2} P^2(k) dk \right]^{\frac{1}{2}} \quad (12)$$

Because  $\frac{\delta n^F}{n}(k, \Delta k)$  is about five percent in the bandpass interval  $\Delta k$  of the observed images,  $(v_{in}^E/\Omega_i) \sim 0.1$ ,  $L_F \sim 20$  km, and the value of  $k_o$  at the peak of the image growth rate is  $\sim 10^{-2} \text{ m}^{-1}$ ,  $R \approx 1$ . Thus, the growth of images should occur on a similar time scale to that of the "parent" striations. The growth rate of images is even faster at lower altitudes for comparable electron densities. Thus, because the occurrence of bottomside spread F is well known and documented, the formation of image striations should be rapid and our steady state analysis reasonable.

In order to directly compare the result given in Equation (10) with the measurements we must take its absolute value squared and divide by  $\Delta k$ , yielding the predicted power spectral density. Using parameters suitable for the equatorial ionosphere:  $v_{in}^E/\Omega_i = .1$ ;  $g/v_{in}^F = 25$  m/s;  $D_1 = 10 \text{ m}^2/\text{s}$ ;  $\alpha_{eff} = 1 \times 10^{-7} \text{ cm}^3 \text{ s}^{-1}$  and  $n_o^E = 10^4 \text{ cm}^3$ , yields the result plotted in Figure 6. The plot displays a spectral shape that is similar to the observations shown in Figure 5, although our theory predicts a higher amplitude of irregularities than was actually observed. The amplitude could be made to agree more closely by adjusting some of the poorly known quantities such as  $\alpha_{eff}$  or  $v_{in}$ . However, our point here is to establish the validity of the theory and point out some consequences of the physical process. To do so we need not reproduce data exactly.

### C. Electric Field Mapping Considerations

We turn now to the question of electric field mapping. Qualitatively the effect should be only to steepen the drop off in spectral intensity at large  $k$  since the mapping efficiency is best for large wavelengths. Being slightly more quantitative we can use Farley's [1959] result for high latitudes since we are considering an F region source at the dip equator mapped along magnetic field lines which are perpendicular to the source region. The only change is that the field maps in two directions which reduces the mapping length by a factor of two. Farley showed that the crucial parameter in this regard is the reduced height

$$dz' = (\sigma_p/\sigma_o)^{1/2} dz$$

where  $\sigma_p$  is the Pedersen conductivity,  $\sigma_o$  is the parallel conductivity, and  $dz$  and  $dz'$  are parallel to  $\underline{B}$ .

In a coordinate system with  $z$  replaced by  $z'$ , spatial variations in the electric potential in the  $x$  and  $y$  direction will be accompanied by variations of comparable scale in the direction parallel to  $\underline{B}$ . That is, the potential distribution will be isotropic in the reduced coordinate system. Physically, the variation is due to the finite conductivity of the medium in the direction parallel to  $\underline{B}$  and the resulting finite potential drop along the magnetic field. For an equatorial F region source at 300 km, as hypothesized in the present paper, the reduced height factor is given by

$$(\sigma_o/\sigma_p)^{1/2} = 1686 (10^5/n)^{1/2}$$

where  $n$  is the electron density in  $\text{cm}^{-3}$ .

In contrast to the Farley [1959] case which only dealt with E region sources, the height reduction factor is very large for an F region source. Thus, sub-kilometer scale structure will map for large distances from an F region source and can act upon the lower altitude plasma in the manner discussed above.

#### D. Effects of Image Formation on F-Layer Structure

Up to this point we have emphasized the effects on the image region of a plasma instability operating elsewhere along the magnetic field line. However, because the system is closely coupled, the formation of images has important ramifications for the evolution of the F layer "parent" structure as well. As an example, let us consider the simple case of a decaying (i.e., non-driven) cylindrical density irregularity in the F layer. The processes involved in image formation for this situation are illustrated schematically in Figure 7. Diffusion acts to move plasma away from the high density region (assumed near the center of the cylinder in Figure 7) and into the less dense regions outside. The inherent diffusion rate of ions is higher than for electrons. Ion diffusion is restrained, however, by an electric field which maintains charge neutrality in the plasma. In our cylindrically symmetric case, this electric field is directed inward everywhere inside the cylinder. Because this electric field maps to low altitudes where the ion-neutral collision frequency is high, E-region ions Pedersen drift toward the center of the cylinder and the ion gas is compressed. Provided the E region electron density is low enough, an image striation can grow against recombination [see discussion in Vickrey and Kelley, 1982].

It is important to keep in mind that the electrons are highly magnetized even in the E region. Therefore, the electron gas behaves as an incompressible fluid throughout the altitude region under discussion. Although electrons are tied to a given field line, they can move easily along that field line. Charge neutrality is preserved in the plasma (even though the ion gas is being compressed in the E region and the electron gas is not), by electron motion along magnetic field lines. Thus, the F-region cross-field plasma diffusion process changes the altitude distribution but not the total number of electrons on a given flux tube. The net loss of electrons from the F region portion of a flux tube exactly balances the net gain of ions in the E region image. Since, as we have shown, the image growth rate is scale size dependent, the effective cross-field diffusion rate in the F layer should also be affected differently for different scales. Indeed, to explain recent scintillation observations of a decaying equatorial F layer plume one must invoke an effective diffusion rate that has such a scale size dependence [Livingston et al., 1983].

## IV SUMMARY

In this paper we have presented what we believe is the first evidence for the formation of image irregularities in the ionospheric medium. We have also computed a saturated power spectral density for the structure and find that the amplitude and wavelength dependence matches the observed spectra quite well.

The case we have studied involves images of F-region irregularities created by the Rayleigh-Taylor process in equatorial spread F. A similar analysis should apply, however, to any process that produces structure in the electric field perpendicular to B. At auroral latitudes image striations may not form because chemical damping due to recombination is large due to particle precipitation (Vickrey and Kelley, 1982). Exceptions might be in the winter polar cap or in the region just equatorward of the nighttime diffuse auroral zone where the E-region density should be comparable to mid-latitude values.

The formation of image striations depends upon the compressibility of the ion gas in the E region. However, because the electron gas is incompressible even at E region heights, the image formation process redistributes electrons in altitude along the magnetic field. This redistribution results in an effective diffusion rate in the F region which is scale size dependent. Thus, field line coupling to the E region will affect the temporal evolution of plasma structure all along the flux tube.

ACKNOWLEDGMENT: We wish to acknowledge very helpful discussions with Dr. Rod Heelis. This work was supported by the Defense Nuclear Agency under contract DNA001-83-C-0034 and by the Air Force Office of Scientific Research under contract no. F49620-83-K-0025.



## REFERENCES

- Costa, E., and M. C. Kelley, "On the Role of Steepened Structures and Drift Waves in Equatorial Spread F," J. Geophys. Res., 83, 4359, 1978.
- Farley, D. T., Jr., "A Theory of Electrostatic Fields in a Horizontally Stratified Ionosphere Subject to a Vertical Magnetic Field," J. Geophys. Res., 64, 1225, 1959.
- Fejer, B. G., and M. C. Kelley, "Ionospheric Irregularities," Rev. Geophys. & Space Phys., 18, 401, 1980.
- Goldman, S. R., L. Baker, S. L. Ossakow, and A. J. Scannapieco, "Striation Formation Associated with Barium Clouds in an Inhomogeneous Ionosphere," J. Geophys. Res., 81, 5097, 1976.
- Kelley, M. C., G. Haerendel, H. Kappler, A. Valenzuela, B. B. Balsley, D. A. Carter, W. L. Ecklund, C. W. Carlson, B. Hausler, and R. Torbert, "Evidence for a Rayleigh-Taylor Type Instability and Upwelling of Depleted Density Regions During Equatorial Spread F," Geophys. Res. Letts., 3, 48, 1976.
- Kelley, M. C., K. D. Baker, and J. C. Ulwick, "Late Time Barium Cloud Striations and their Relationships to Equatorial Spread F," J. Geophys. Res., 84, 1898, 1979.
- Kelley, M. C., R. Pfaff, K. D. Baker, J. C. Ulwick, R. Livingston, C. Rino and R. Tsunoda, "Simultaneous Rocket Probe and Radar Measurements of Equatorial Spread F--Transitional and Short Wavelength Results," J. Geophys. Res., 87, 1575, 1982.
- Keskinen, M. J., and S. L. Ossakow, "On the Spatial Power Spectrum of the E X B Gradient Drift Instability in Ionospheric Plasma Clouds," J. Geophys. Res., 86, 6947, 1981.

## REFERENCES concluded

- Lloyd, J. H., and G. Haerendel, "Numerical Modeling of the Drift and Deformation of Ionospheric Plasma Clouds and of their Interaction with Other Layers of the Ionosphere," J. Geophys. Res., 78, 7389, 1973.
- Livingston, R. C., J. F. Vickrey, E. J. Weber, and J. Buchau, "Irregularity Decay in an Isolated Plasma Bubble," to be submitted, J. Geophys. Res., 1983.
- Morse, F. A., B. C. Edgar, H. C. Koons, C. J. Rice, W. J. Heikkila, J. H. Hoffman, B. A. Tinsley, J. D. Winningham, A. B. Christensen, R. F. Woodman, J. Pomalaza, and R. N. Teixeira, "Equion, An Equatorial Ionospheric Irregularity Experiment," J. Geophys. Res., 72, 578, 1977.
- Narcisi, R., and E. P. Szuszcwicz, "Direct Measurements of Electron Density, Temperature, and Ion Composition in an Equatorial Spread F Ionosphere," J. Atmos. Terr. Phys., 43, 463, 1981.
- Ossakow, S. L., "Spread-F Theories--A Review," J. Atmos. Terr. Phys., 43, 437, 1981.
- Rino, C. L., R. T. Tsunoda, J. Petriceks, R. C. Livingston, M. C. Kelley and K. D. Baker, "Simultaneous Rocketborne Beacon and in situ measurements of Equatorial Spread-F--Intermediate Wavelength Results," J. Geophys. Res., 86, 2411, 1981.
- Szuszcwicz, E. P., R. T. Tsunoda, R. Narcisi, and J. C. Holmes, "Coincident Radar and Rocket Observations of Equatorial Spread F," Geophys. Res. Letts., 7, 537, 1980.
- Vickrey, J. F., and M. C. Kelley, "The Effects of a Conducting E Layer on Classical F Region Cross-Field Plasma Diffusion," J. Geophys. Res., 87, 4461, 1982.
- Volk, H. J., and G. Haerendel, "Striations in Ionospheric Ion Clouds, 1," J. Geophys. Res., 76, 4541, 1971.

## FIGURE CAPTIONS

Figure 1 (a) Downleg Plasma Density Data Measured During the Natal Rocket Flight. Fluctuations in the topside data above 330 km are spurious but those below that height are valid.

(b) Expanded Plot of F-Layer Valley and E-Region Density Profiles from (a).

Figure 2 Schematic Diagram of the Magnetic and Field Mapping Geometry we Propose to Explain the Image Mechanism.

Figure 3 Plasma Density Data Measured During the Downleg of PLUMEX I.

Figure 4 (a) Waveform and Spectrum of Irregularities Between 303 and 322 km Altitude Corresponding to Figure 1(a).

(b) Waveform and Spectrum of Irregularities Between 294 and 312 km Altitude Corresponding to Figure 1(a)

(c) Waveform and Spectrum of Irregularities Between 267 and 287 km Altitude Corresponding to Figure 1(a)

Figure 5 (a) Waveform and Spectrum of Irregularities Observed Between 194 and 204 km Altitude Corresponding to Figure 1(a).

(b) Waveform and Spectrum of Irregularities Observed Between 173 and 184 km Altitude Corresponding to Figure 1(a).

Figure 6 Theoretical Steady-State Spectrum of Image Fluctuations Predicted by Equation (10)

Figure 7 Schematic Diagram Showing the Redistribution of Electrons Along the Magnetic Field During the Image Formation Process.

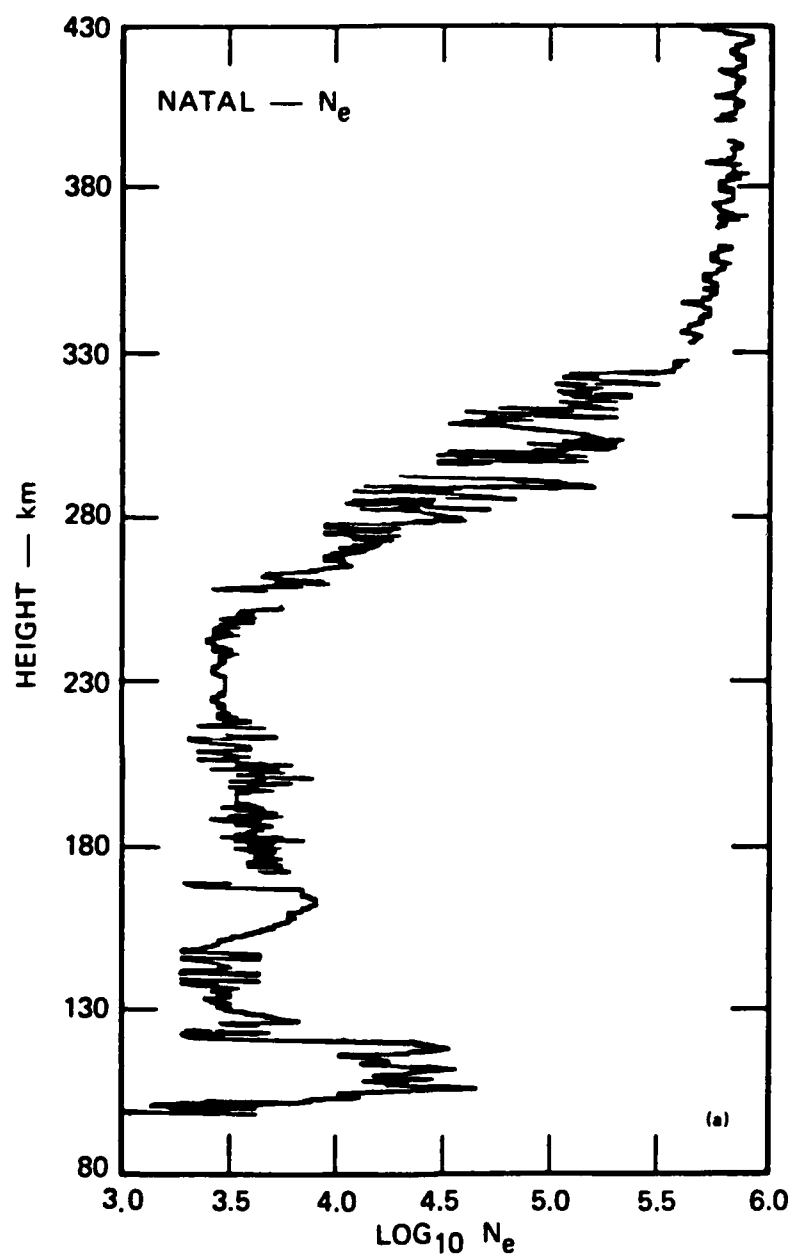


Figure 1(a)

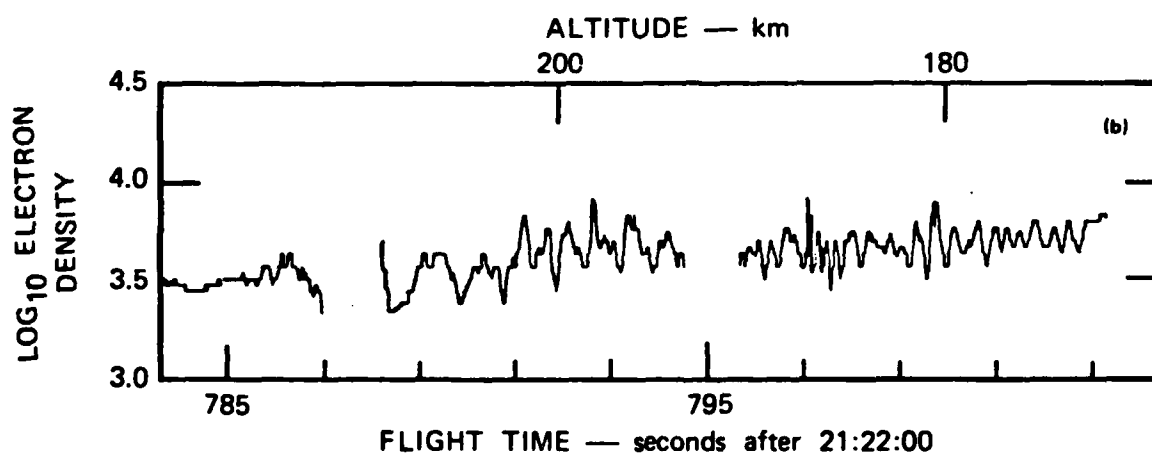


Figure 1(b)

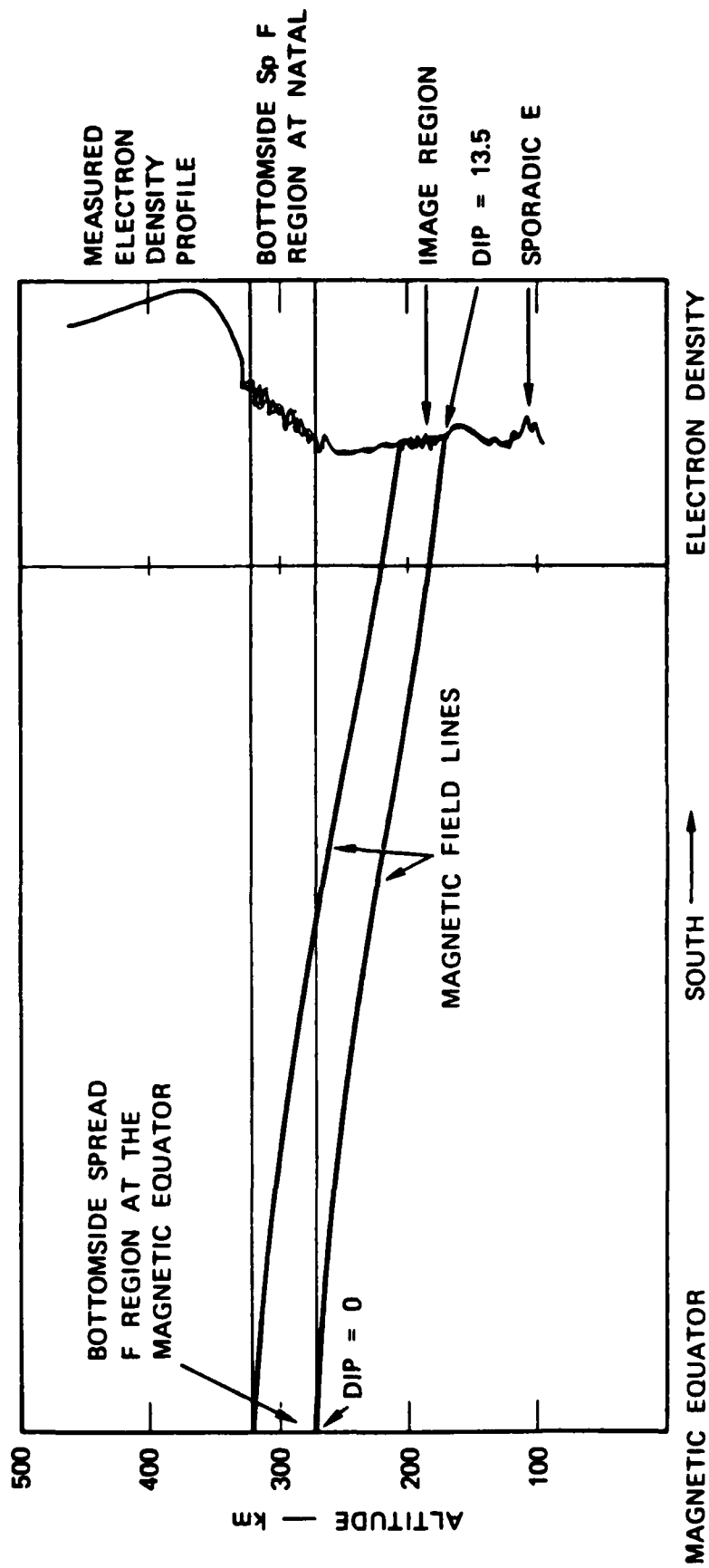


Figure 2

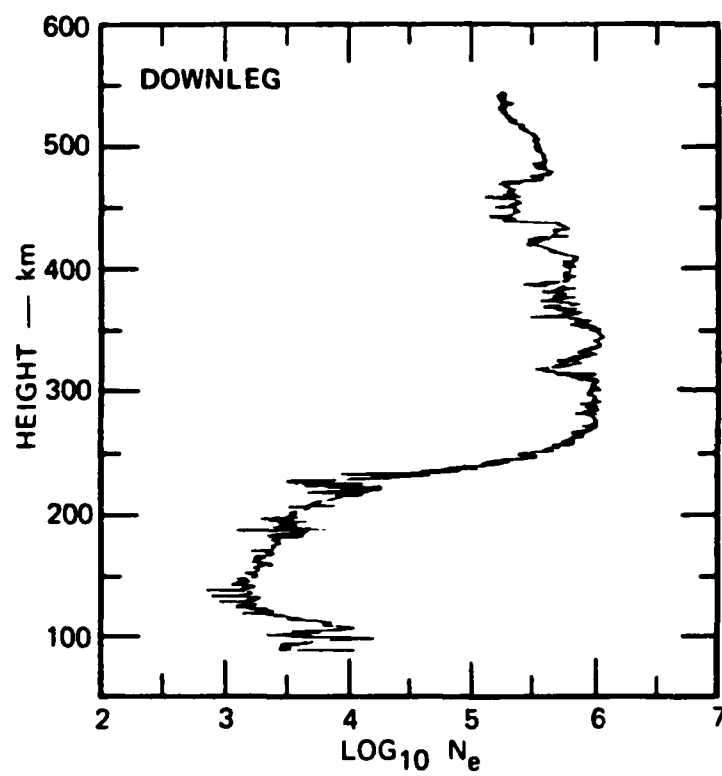


Figure 3

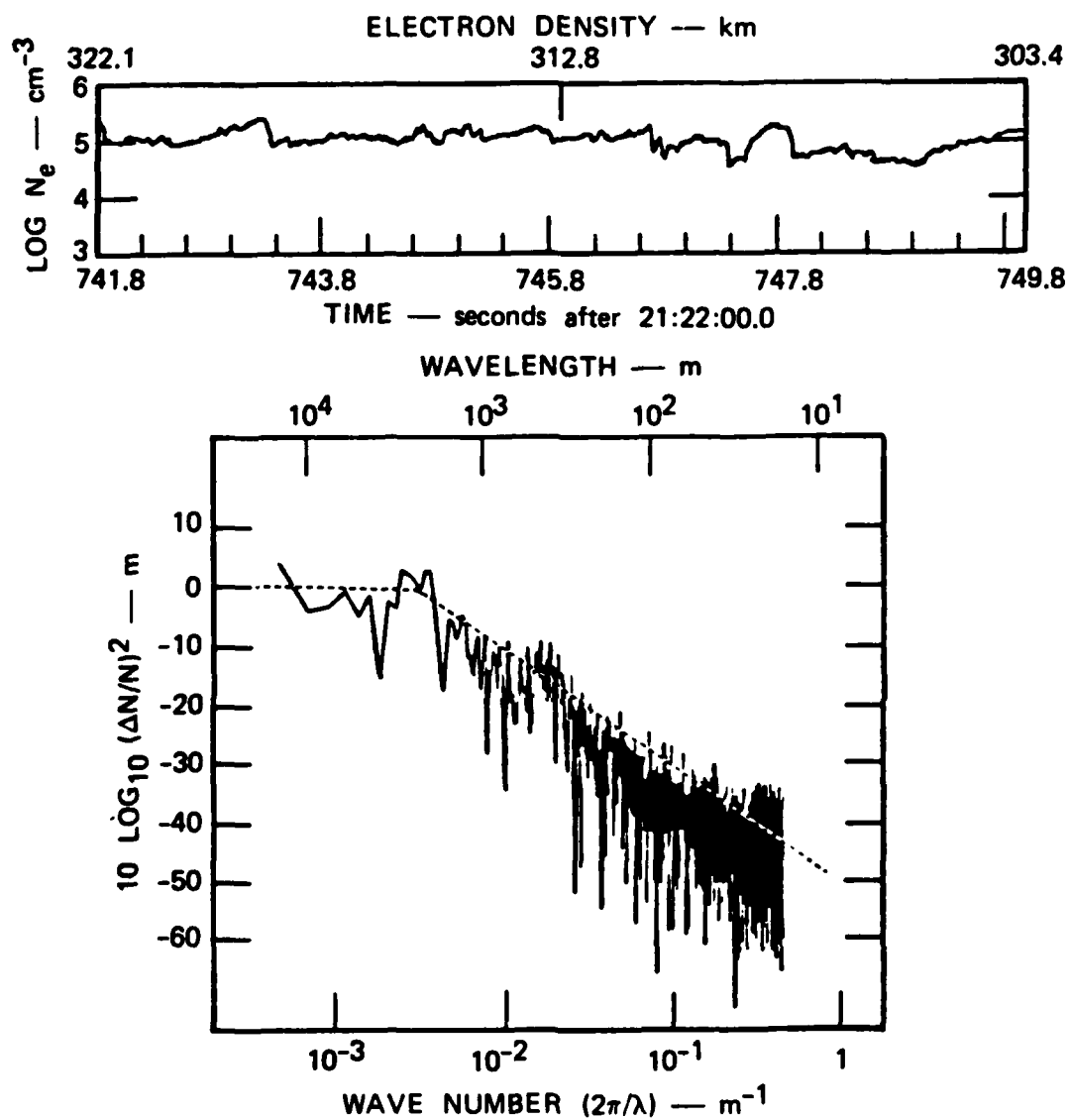


Figure 4(a)



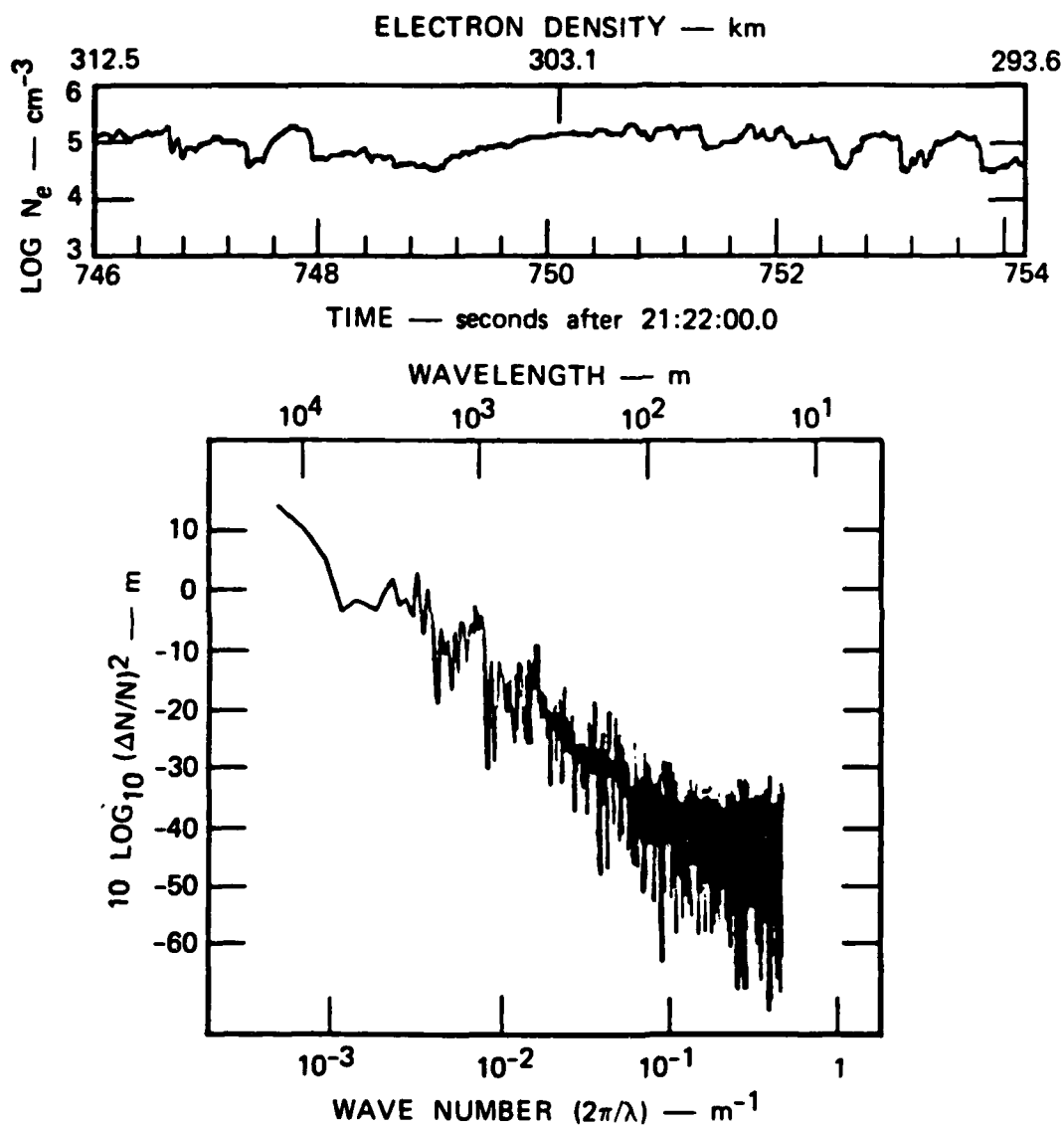


Figure 4(b)

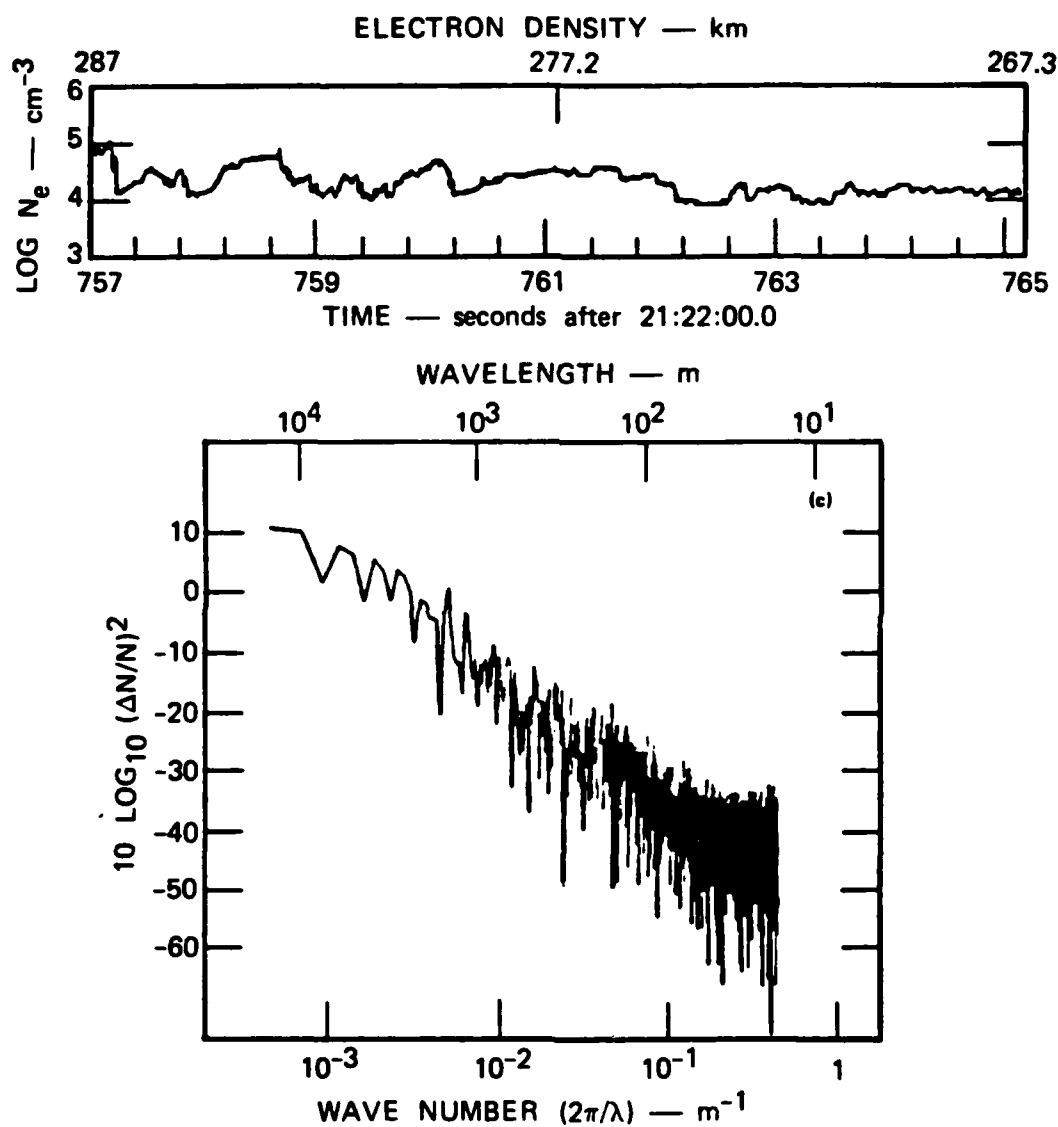


Figure 4(c)

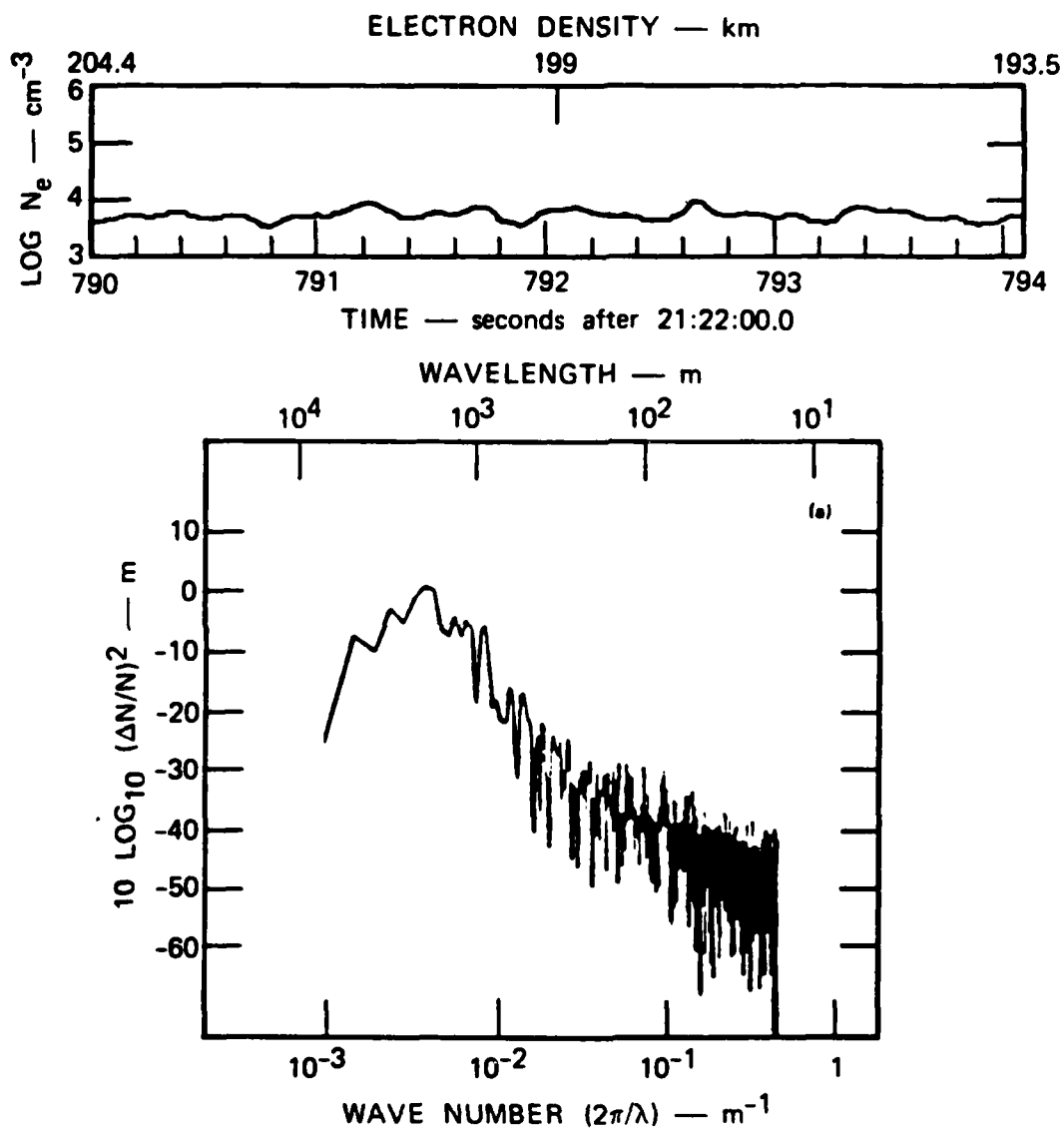


Figure 5(a)

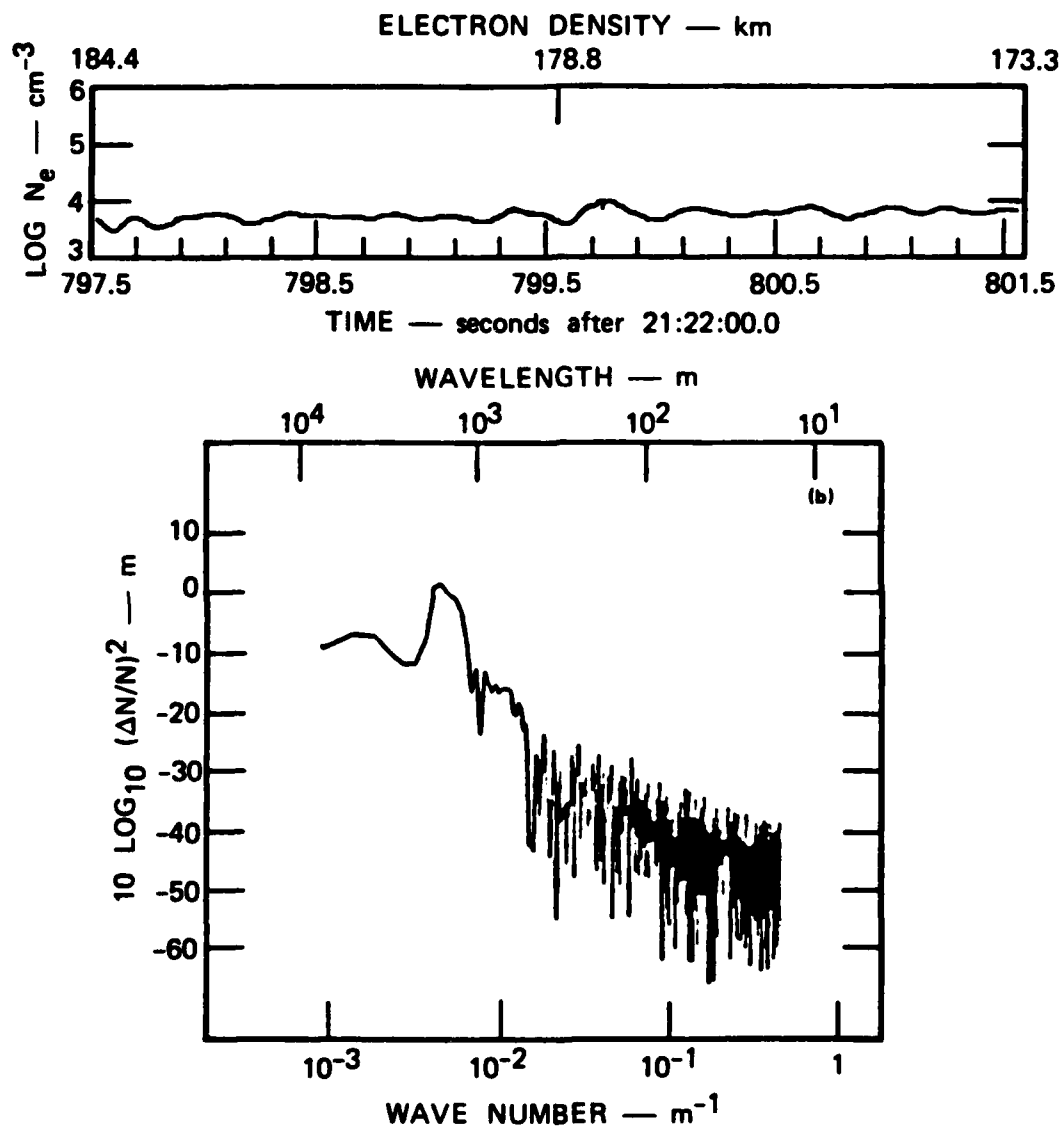


Figure 5(b)

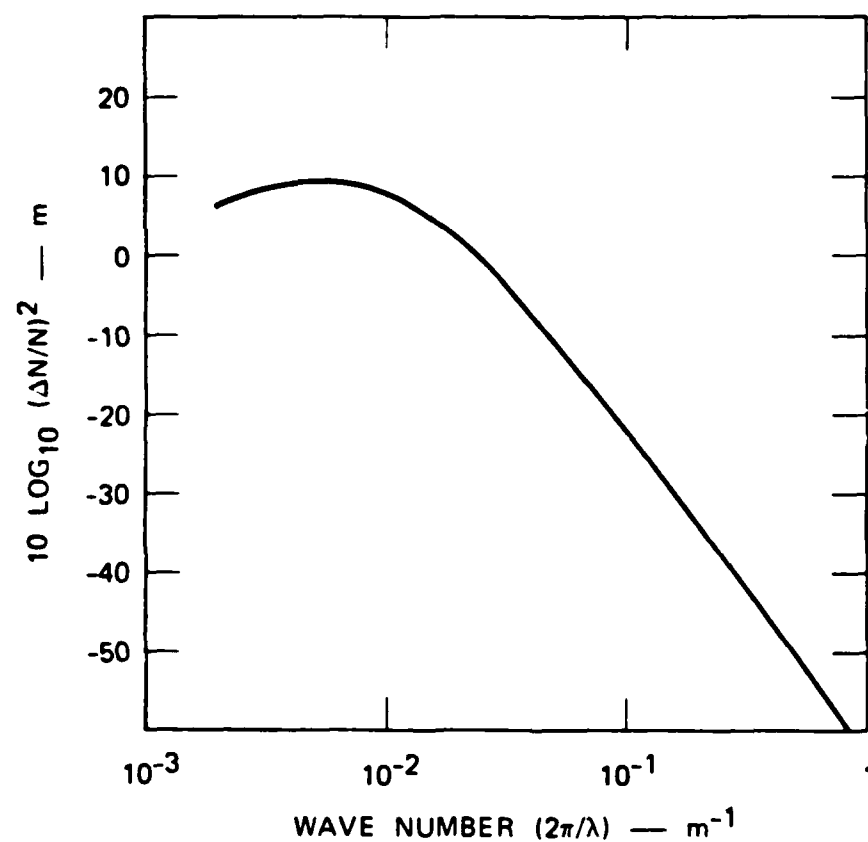


Figure 6

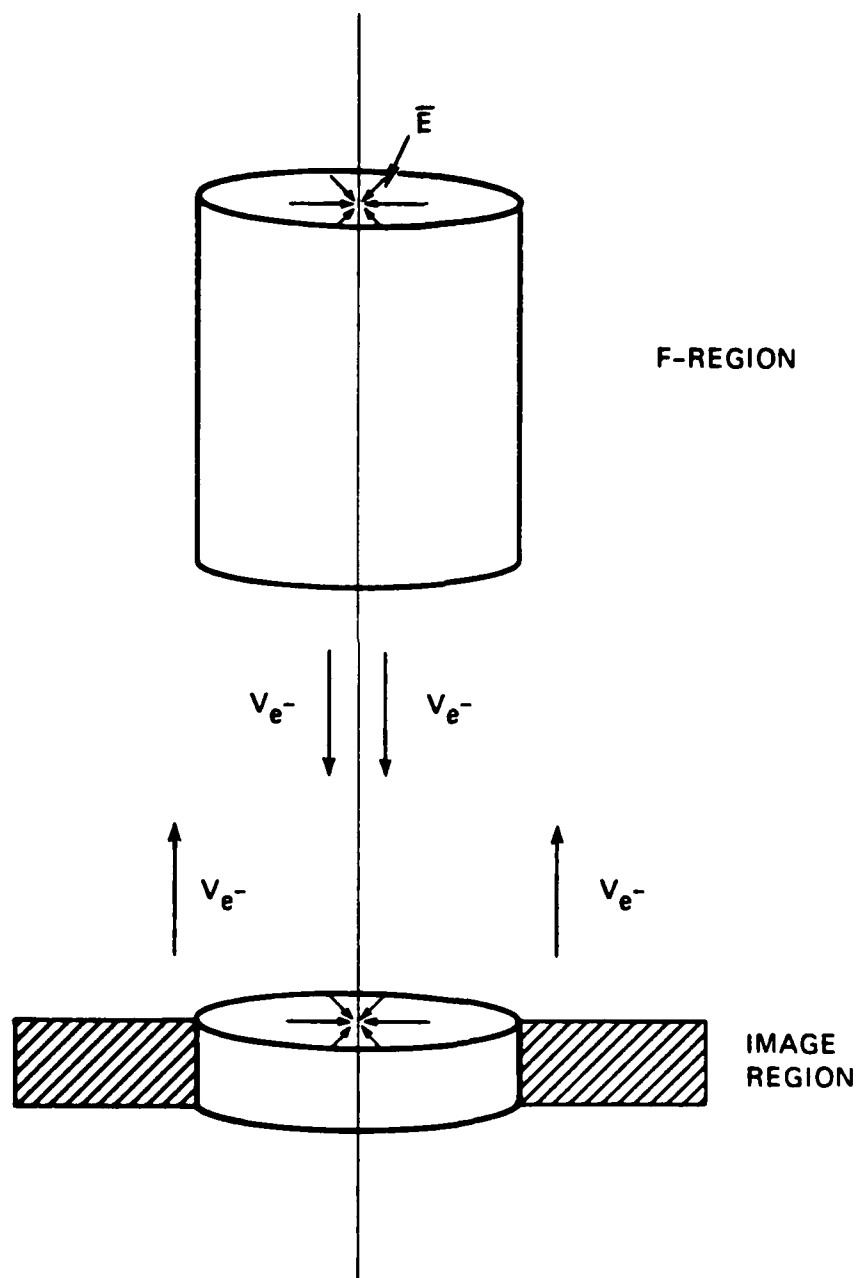


Figure 7

APPENDIX B

IRREGULARITY DECAY IN AN ISOLATED PLASMA BUBBLE

R. C. Livingston and J. F. Vickrey

SRI International  
Menlo Park, CA 94025

M. C. Kelley

School of Electrical Engineering  
Cornell University  
Ithaca, NY 14853

E. J. Weber and J. Buchau

Air Force Geophysics Laboratory  
Hanscom Air Force Base, MA 01731



# ABSTRACT

Complex signal scintillation observations of an isolated and decaying equatorial plasma bubble are described. Multiple scans through the bubble made from the Air Force Geophysics Laboratory (AFGL) Airborne Ionospheric Observatory, show evolution of irregularity energy over a broad range of scale sizes. At wavelengths larger than about 4 km, the energy remains nearly constant with time. At shorter scale sizes the spectrum maintains an approximate power law form ( $f^{-n}$ ) and  $n$  increases with time. This behavior suggests that the effective cross-field diffusion rate in the F region is scale size dependent. A scale size dependence of the diffusion rate has recently been predicted theoretically [Vickrey et al., 1983] and is the result of magnetic field line coupling to the E layer.

## 1. INTRODUCTION

Irregularity generation in the nighttime equatorial F-region is dominated by the large scale electron density structures which have come to be known as plasma bubbles. These depleted regions and the irregularities they produce as they develop, are clearly associated with radar backscatter, ionogram spread-F, airglow depletions and radiowave scintillation [Ossakow, 1979, and references cited therein]. Typically, the experimental effort has been directed toward the growth and full development phases of plasma bubbles in the early evening local time sector. In this paper we describe measurements of a much weaker, decay phase bubble. By making repeated scans through that bubble, detailed changes in its irregularity content have been measured.

The observations were made using the Air Force Geophysics Laboratory's Airborne Ionospheric Observatory. Previous measurements using the aircraft have established the bottomside airglow, spread-F and intensity scintillation signatures of equatorial plasma bubbles [e.g., Weber et al., 1980]. In early 1979, the scintillation measurement capability of the aircraft was expanded to provide complex signal measurements from CW satellite sources using a technique outlined in Livingston [1983]. The phase of a transionospherically propagated signal is not strongly affected by diffraction at the frequencies and perturbation levels of interest here [Rino, 1979], and its power spectrum provides an almost direct mapping of the in-situ irregularity continuum. The inherent sensitivity of the phase measurements also makes it possible to observe subtle changes in that

continuum over a large range of spatial scales. This time/wavelength dependence of spectral energy is an essential element in the definition of irregularity decay.

## 2. EXPERIMENT BACKGROUND

The observations included in this paper were made during a flight from Ascension Island on 27/28 March, 1979; the objective of that flight was to locate an isolated, eastward-drifting plasma depletion, and to make repeated scintillation measurements through the disturbance as it decayed. A route was selected far enough south of the magnetic equator to ensure high enough background 6300 Å airglow intensities to contrast with the plasma bubbles and associated airglow depletions. Early in the flight, one moderate airglow depletion was observed, but the structure had decayed before any propagation raypaths intersected the disturbance. A second depletion was encountered shortly thereafter, and, at local times between 2300 to 0130 hours, a series of east-west legs were flown to make repeated scintillation and optical measurements of the bubble as it decayed.

Figure 1 is a map of the F-region (350 km) penetration point scanned by the aircraft during the multiple east-west flight legs. The successive tracks are nearly parallel, and each is at a constant dip latitude near  $13^{\circ}$ . The radio scintillation source used throughout the scintillation measurements was a 249 MHz signal from a geostationary satellite located due west of the aircraft at an elevation of  $73^{\circ}$ . The aircraft speed was nearly constant in both eastward and westward directions producing a cross field penetration velocity component of slightly greater than 200 m/s at F region altitudes.

Figure 1. Map of 350 km Altitude Ionospheric Penetration

Point for Consecutive East-West Flight Legs

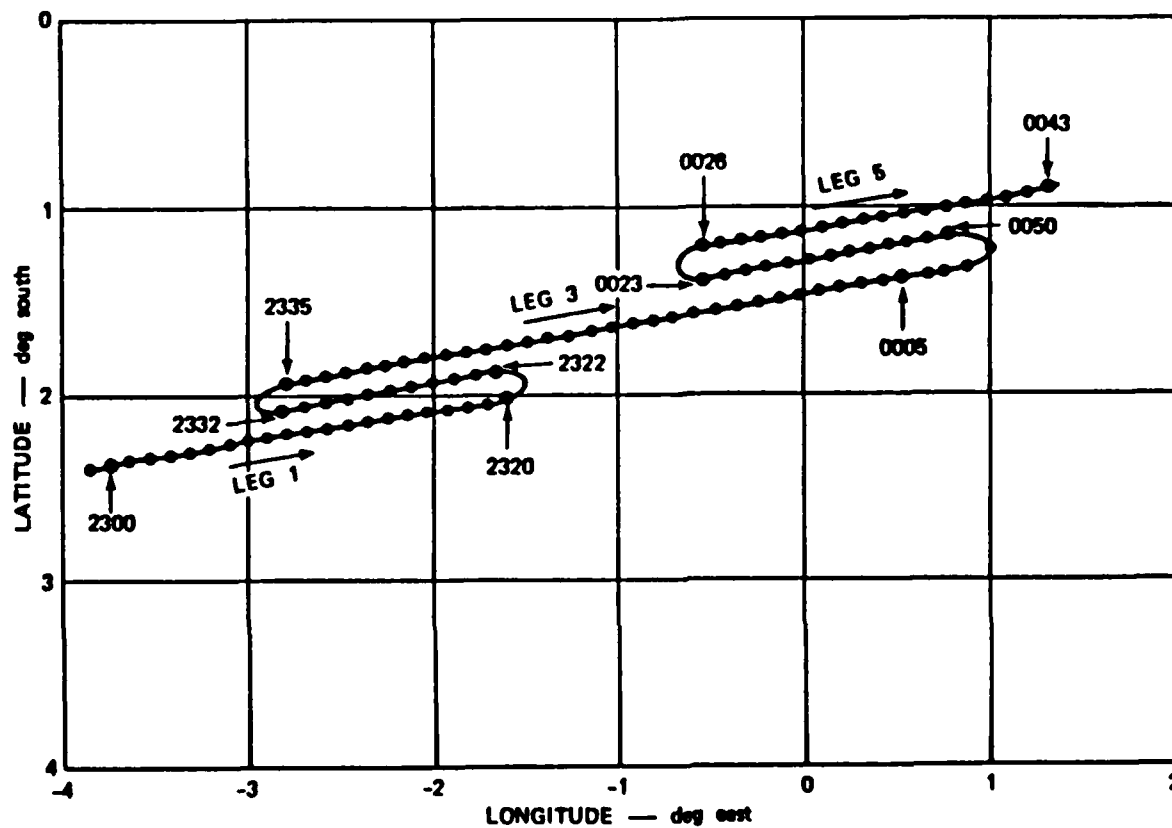
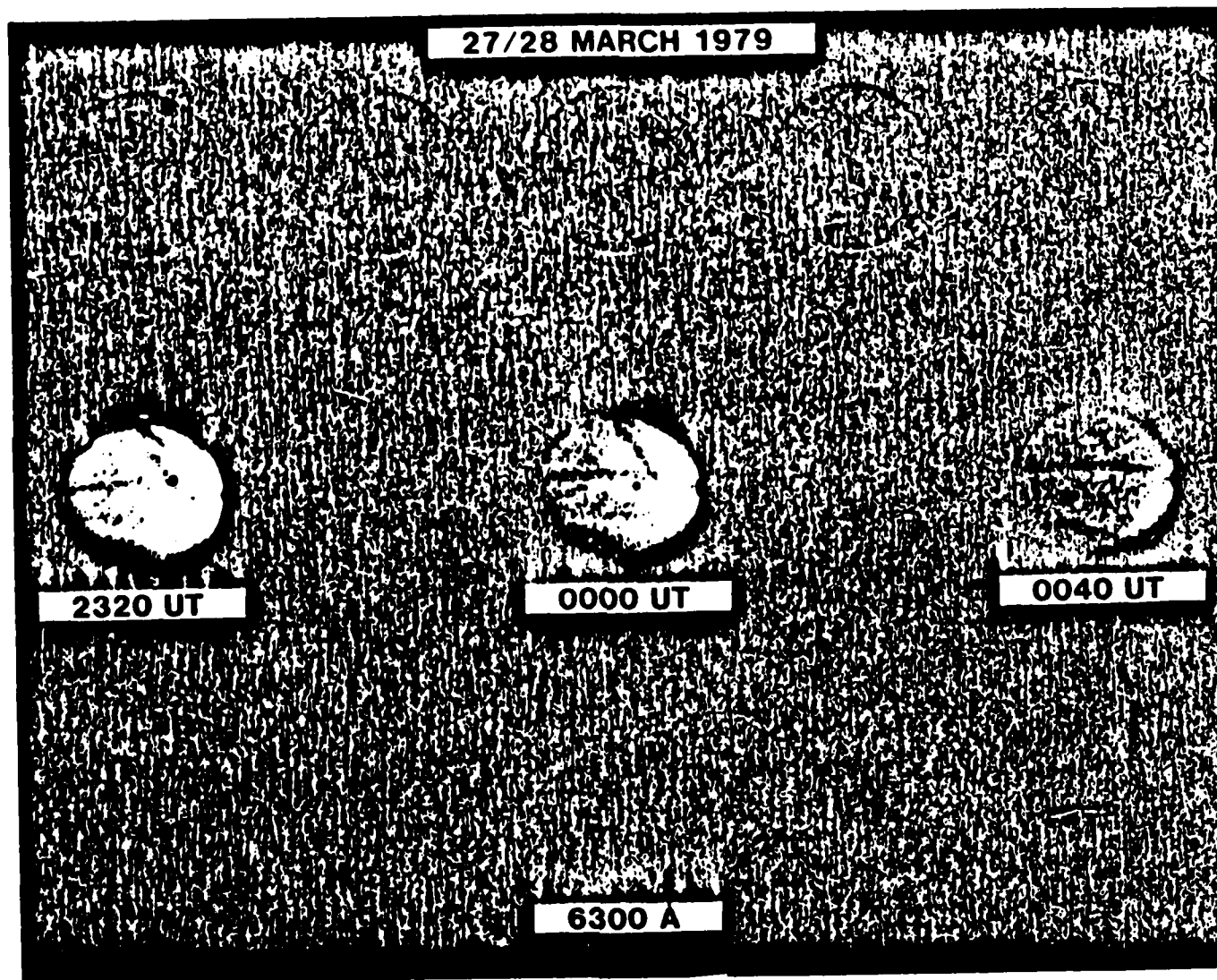


Figure 2 shows the all sky 6300 Å airglow images for three times during the flight. The dots indicate the propagation path intersection at the assumed airglow emission height of 250 km, where the all-sky lens images a circle of 600 km radius in the ionosphere. The airglow depletions visible in Figure 2, although structured, are relatively weak compared to others measured near Ascension Island in 1978 [Weber et al., 1980]. They do, however, verify continuity in the structure we are investigating on consecutive airplane passes.

Figure 2. 6300 Å Airglow Images of the Bubble, with  
the Ionospheric Penetration Point Indicated



### 3. TEC STRUCTURE AND INTENSITY SCINTILLATION

Figure 3a shows the signal intensity and large-scale dispersive phase variation, flying eastward for leg 1, the first scan through the bubble. The onset of intensity scintillation, which is caused by irregularities of ~200 m cross-field dimension, is very rapid on the western edge of the disturbance and is associated with a gradient in total electron content (TEC) which entails a decrease in column density of about  $1 \times 10^{17}$  electrons/m<sup>2</sup>.

The Rayleigh-Taylor instability generation of plasma bubbles in the nighttime equatorial ionosphere is by now, a much-studied and reasonably well-understood process. In some cases, the bubble growth is moderate or stalls at an early stage, leaving a large, westward tilted density depletion in the bottomside F-region [Tsunoda, 1981]. Although the large-scale growth stage of the bubble itself has ended, its edges are still prone to gradient drift instability structuring. At these local times, the zonal neutral wind is large ( 150 m/s) and eastward. In such conditions the generalized Rayleigh-Taylor process is unstable to a westward directed plasma gradient [Kelley et al., 1981]. It is therefore the westward edge of an upwelling which is most likely to develop intermediate scale structure. This behavior is consistent with Figure 4 which is a simple model based upon our  $\Delta$ TEC and scintillation data for flight leg 1. The vertical extent of the bubble can only be guessed. There is no question, however, that it is the west wall which is structured in regions where the plasma drift vector and the density gradients are parallel.

Figure 3. Intensity and Phase Records for Scans  
Through the Bubble, Flight Legs 1 through 5.

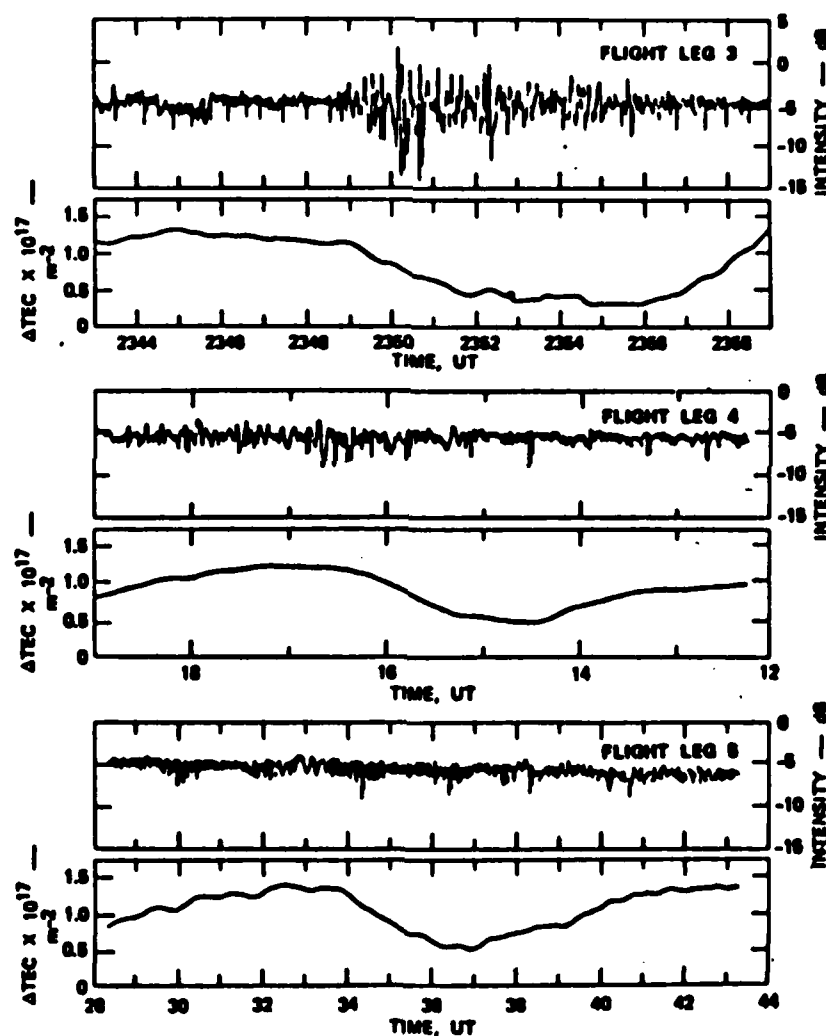
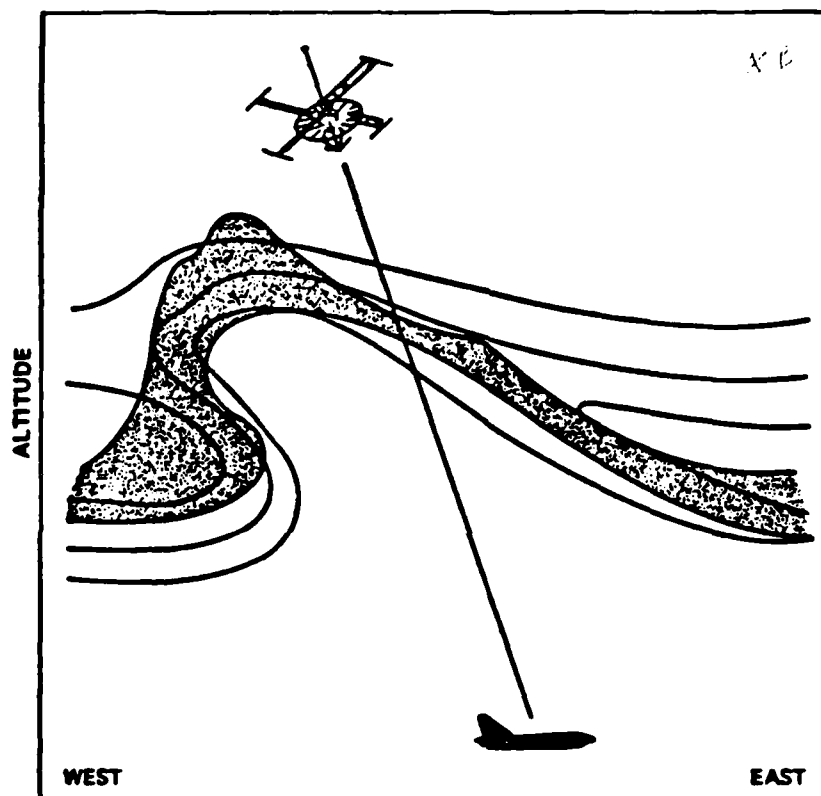




Figure 4. One Possible Configuration of Electron Density (contours) and Irregularity Distribution (shaded) Which Duplicates the Observed Signal Structure.



In Figures 3b through 3e, the intensity scintillation and  $\Delta\text{TEC}$  for subsequent cuts through the drifting bubble are shown. For westward legs, the time scales have been reversed and expanded to match those eastward, in both direction and distance. The relative eastward/westward time scales were ascertained by first locating, in space (Figure 1), the westward intensity scintillation or depletion boundaries for consecutive legs. This yields a cross-field, macroscale drift of  $\sim 90$  m/s throughout the observation period at a penetration altitude of 350 km.

By comparing flight legs in Figure 3 it can be seen that the intensity scintillation declines rapidly to a level indistinguishable from the noise level by the fourth leg, but the  $\Delta\text{TEC}$  pattern remains nearly constant in form. (On the second leg, the phase data is distorted prior to 2325 UT by rapid aircraft deviation from straight and level flight.)

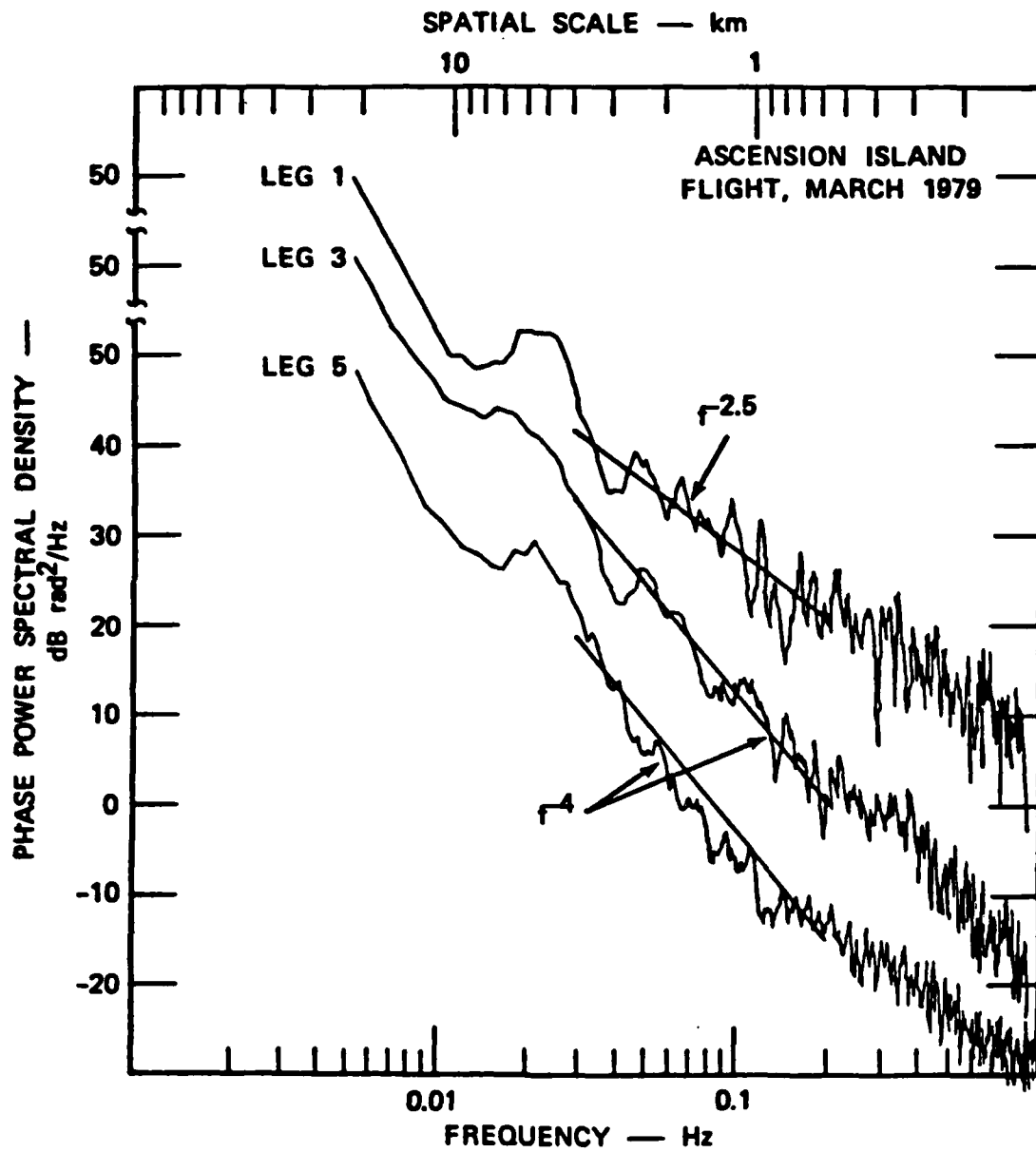
#### 4. PHASE SPECTRA AND IRREGULARITY DECAY

The intensity records in Figure 3 effectively illustrate the east-west asymmetry in, and temporal decay of  $> 400$  m spatial scale irregularities. The phase data and, in particular, the temporal changes in energy and the shape of the phase spectra from leg to leg, can be used to quantitatively determine the decay rate and provide information about possible decay mechanisms.

In Figure 5, the phase spectra of the overall bubble are shown for the three eastbound flight legs (1, 3, and 5). These have been offset from one another by 10 dB for clarity. By including the entire bubble in each spectrum, we can observe energy in spatial wavelengths from the  $\sim 80$  km outer scale down through about 400 m. For the eastbound flight, the bubble drifts with the aircraft, producing an effective scan rate of  $\sim 110$  m/s. This establishes the correspondence between the temporal and irregularity cross field spatial scales shown.

The spectrum for leg 1 is of a familiar experimental form (although no theory has yet successfully predicted this power law index). It is nearly power law with an average spectral index near -2.5; this slope and the spectral density levels agree well with those observed in morphological studies of irregularity spectra at the equator [e.g., Livingston et al., 1981]. Such a phase spectral index corresponds to a one-dimensional rocket or satellite spectrum with index -1.5. We consider it, then, to be the signature of a region sampled during, or shortly after, Rayleigh-Taylor

Figure 5. Phase Power Spectra for the Bubble  
From Flight Legs 1, 3, and 5.



and/or gradient drift structuring, as already suggested. For legs 3 and 5, however, sampled some 40 and 70 minutes after leg 1, the spectra have considerably steepened through energy decay at short spectral scales. For purposes of discussion, we will use the break in the spectra which this decay creates near 4 km, as the dividing line between two different regimes.

At spatial scales larger than about 4 km, the spectra are nearly equal in shape and in energy content for all flight legs. The decay at the peak is only about 5 dB in 70 minutes time. Since the scintillation technique is sensitive to  $(\Delta N)^2$  rather than  $(\Delta N/N)^2$ , some of the observed decay may be due to the decrease in absolute plasma density. A detailed interpretation of the spectral features in this large scale regime, which is dominated by aeronomic processes (Booker, 1979), is beyond the scope of this paper. The broad enhancement in energy centered near 7 km which is made conspicuous by the energy depletion near 15 km, may be a remnant of the larger-scale perturbation (e.g., a gravity wave) which initiated the bubble. We note that this feature is very similar to that seen in the in-situ electron density spectra presented by Kelley et al. [1982].

Of more interest to the present study, and in contrast to the stability of energy at large scales, the energy at short scales decays rapidly during the observation period. For example, at an irregularity scale size near 1 km, the energy decays at an even rate of  $\sim 9$  dB per hour from leg 1 to leg 3 to leg 5. Using the relationship

$$|\Delta N|^2(k, t_0 + \tau) = |\Delta N|^2(k, t_0) \exp - \{2 k^2 D \tau\} \quad (1)$$

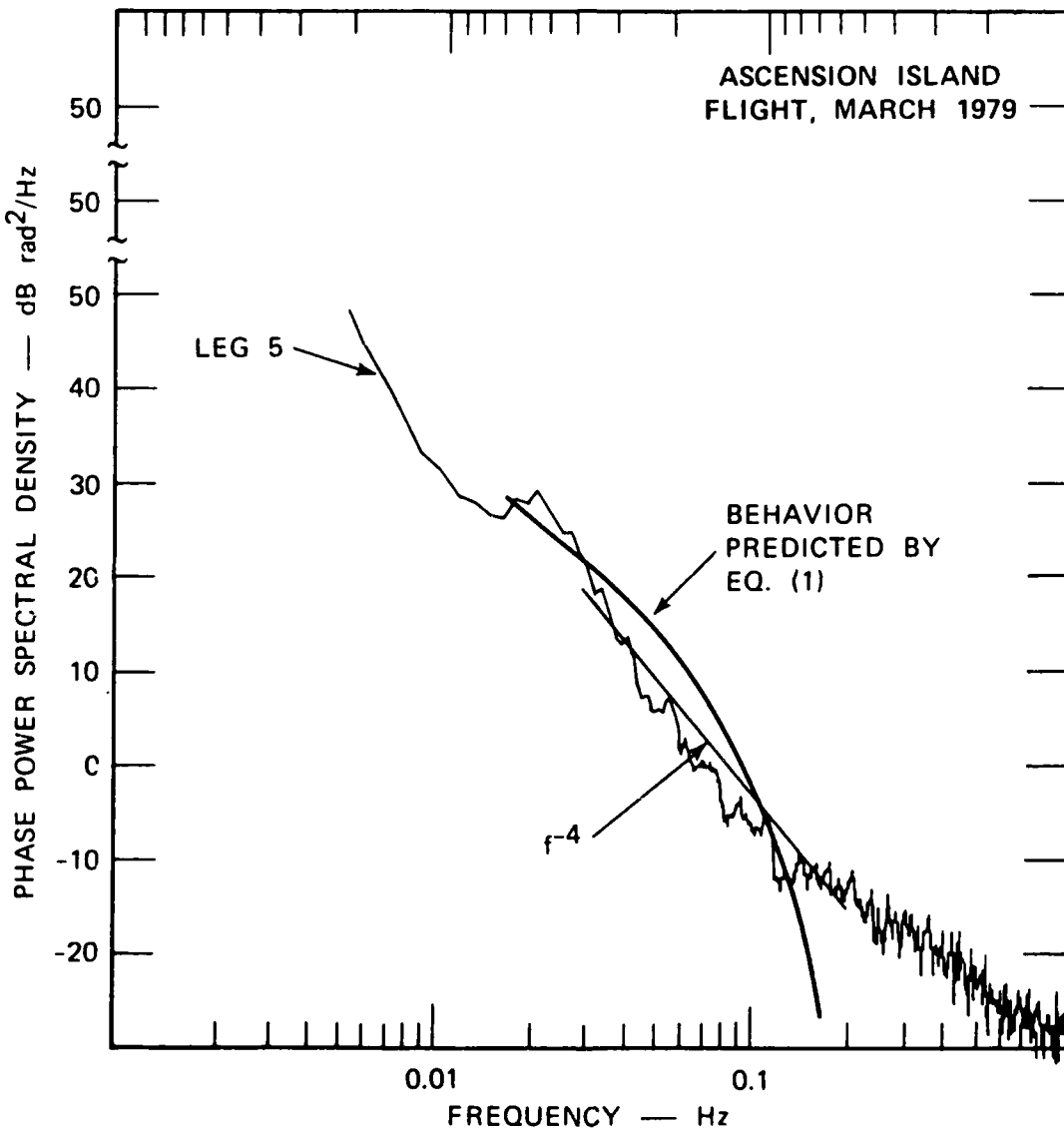
we find a diffusion coefficient for  $k = (2\pi/1000\text{m})$  of  $7 \text{ m}^2/\text{s}$ . On the other hand, the classical ambipolar cross field diffusion coefficient (which is equal to twice the electron perpendicular diffusion coefficient) is given by

$$D_{\perp c} = 2\rho_e^2 v_e \approx 0.96 \text{ m}^2/\text{s} \quad (2)$$

The diffusion coefficient at the one km scale is thus considerably greater than the classical ambipolar rate.

As we shall discuss more fully below, an enhanced diffusion rate is not difficult to explain. What is more interesting is the fact that a single diffusion coefficient (independent of  $k$ ) cannot be used to describe the process. For example, by choosing  $D = 7 \text{ m}^2/\text{s}$ , we can match the decay rate at 1 km, but that is the only scale at which the decay rate is matched by the classical formula given in Equation 1. This result is illustrated in Figure 6 where Equation 1 has been solved at a time,  $t_0$ , corresponding to leg 5 with an input spectrum  $|\Delta N|^2(k, t_0)$  matched to the leg 1 data (the straight line in the figure is the least squares fit to the leg 1 data used as input). The solution matches the observed spectrum at 1 km. However, the experimental decay rate is considerably higher at longer wavelengths and considerably slower at shorter scales.

Diffusion Constant of  $7.2 \text{ m}^2 \text{ s}^{-1}$ .



The initial Spectrum was the straight line fit to leg 1 data

The data in Figure 5 provide an opportunity to determine empirically the scale size dependence of the diffusion rate,  $D_1(k)$ . Over the scale size regime  $400 \text{ m} < \lambda < 4 \text{ km}$ , the spectra in Figure 5 are nearly power law with slopes of -2.5, -4, and -5 respectively. By equating the value of  $|\Delta N|^2$  at 4 km for three such power law spectra and differencing the curves at all other scale sizes, we can solve Equation (1) for  $D_1(k)$ . The result is plotted in Figure 7. The curve represents the average between differencing leg 5 and leg 1 and leg 3 and leg 1. The error bars indicate the differences in the two estimates. This empirical  $D_1(k)$  is, of course, model dependent in the sense that Equation (3) assumes that each Fourier mode decays independently of the adjacent modes. As discussed below, it is unlikely that the physical mechanism or mechanisms which lead to the observed anomalous decay characteristics share the property of mode independence. The  $D_1(k)$  we have found should thus be regarded as both empirical and model dependent.



## 5. DISCUSSION

### A. Enhanced Classical Diffusion

A diffusion coefficient enhanced with respect to the ambipolar rate [Vickrey and Kelley, 1982] can be understood as follows. The ambipolar rate occurs when the more rapid perpendicular ion diffusion leads to a space charge electric field which severely limits the ion flow and slightly enhances the electron velocity. An equilibrium results in which the two fluids diffuse at the same rate. Now if field aligned currents can flow, for example, to a "conducting end plate" such as the E region in the auroral zone [Vickrey and Kelley, 1982], the ambipolar electric field can be "shorted out" and diffusion proceeds at the faster rate determined by

$$D_{\perp c} = \frac{\Sigma_i^F}{\Sigma_i^F + \Sigma_e^F + \Sigma_p^E} (D_{\perp e} - D_{\perp i}) + D_{\perp i} \quad (3)$$

where the  $\Sigma_p$  are the height integrated Pedersen conductivities. The E region is of little importance in the nighttime equatorial zone. However, the conjugate F region has almost by definition, a comparable height integrated conductivity which, when substituted for  $\Sigma_p^E$  above, implies that  $D_{\perp c} \sim .5 D_{\perp i}$ . Taking  $v_{in} = .6 \text{ sec}^{-1}$  and  $\rho_i = 5 \text{ m}$  corresponding to a height of 350 km yields  $D_{\perp c} = 7 \text{ m}^2/\text{s}$ . Thus, the enhanced diffusion rate is not as surprising as the observed wavelength dependence; i.e., the rate of diffusion could be explained classically, but the spectrum of decaying

turbulence is another matter. In the next two sections we investigate two mechanisms which could lead to a scale size dependent diffusion rate.

#### B. The Drift Wave Hypothesis

It has been suggested by Costa and Kelley [1978a,b], Burke et al. [1979], Huba and Ossakow [1981], Kelley [1982], and perhaps others, that drift waves play an important role in F region diffusion. In linear theories these waves are de-stabilized by gradients in the plasma and, in their non-linear state, act to smooth out the gradients which produce them. The result is anomalous diffusion of the driving structure.

Gary [1980] has analytically studied anomalous diffusion due to drift waves. The waves grow at wavelengths such that  $k_{\perp} \rho_1 \gg 1$  which corresponds to wavelengths below about 40 m. Kelley et al. [1982] and Kelley [1982] have compared the amplitude and spectral forms of both density and electric field fluctuations predicted by Gary [1980] and by Bernhardt et al. [1982] in this wavelength regime, and found excellent agreement with data obtained in the topside equatorial spread F environment (i.e., altitudes > 280 km).

Gary's analytical form for the anomalous diffusion coefficient is

$$D_a = \frac{\pi}{9} \left( \frac{KT}{M} \right)^{3/2} \left( \frac{1}{\Omega i} \right)^2 \left( \frac{1}{n} \frac{dn}{dx} \right) \quad (4)$$

which can also be written

$$D_a = 1.29 D_{\perp i} (Kl) \quad (5)$$

where  $l$  is the ion mean free path parallel to the magnetic field ( $v_{tn}^i/v_{in}$ ) and  $K$  is the gradient scale length  $(1/n \, dn/dx)^{-1}$  wave number of the driving scale. For a sinusoidal driver with wavelength of 3 km, corresponding to the break in the spectrum and a mean free path of 450 m,  $D_a = 1.2 D_{\perp i} \approx 17 \, m^2/s$ .

This result is in reasonable agreement with the present data set in the sense that the enhanced decay at long wavelengths may be explained. Since the drift waves themselves occur only at very short wavelengths, however, one must hypothesize a link in  $k$  space for this mechanism to be valid. In fluid turbulence theory such a linkage occurs in the so-called inertial subrange where energy is passed between adjacent wavenumbers and a cascade of energy occurs from large to small scales. The net effect is to maintain the energy level in the intermediate range, with dissipation occurring at short wavelengths.

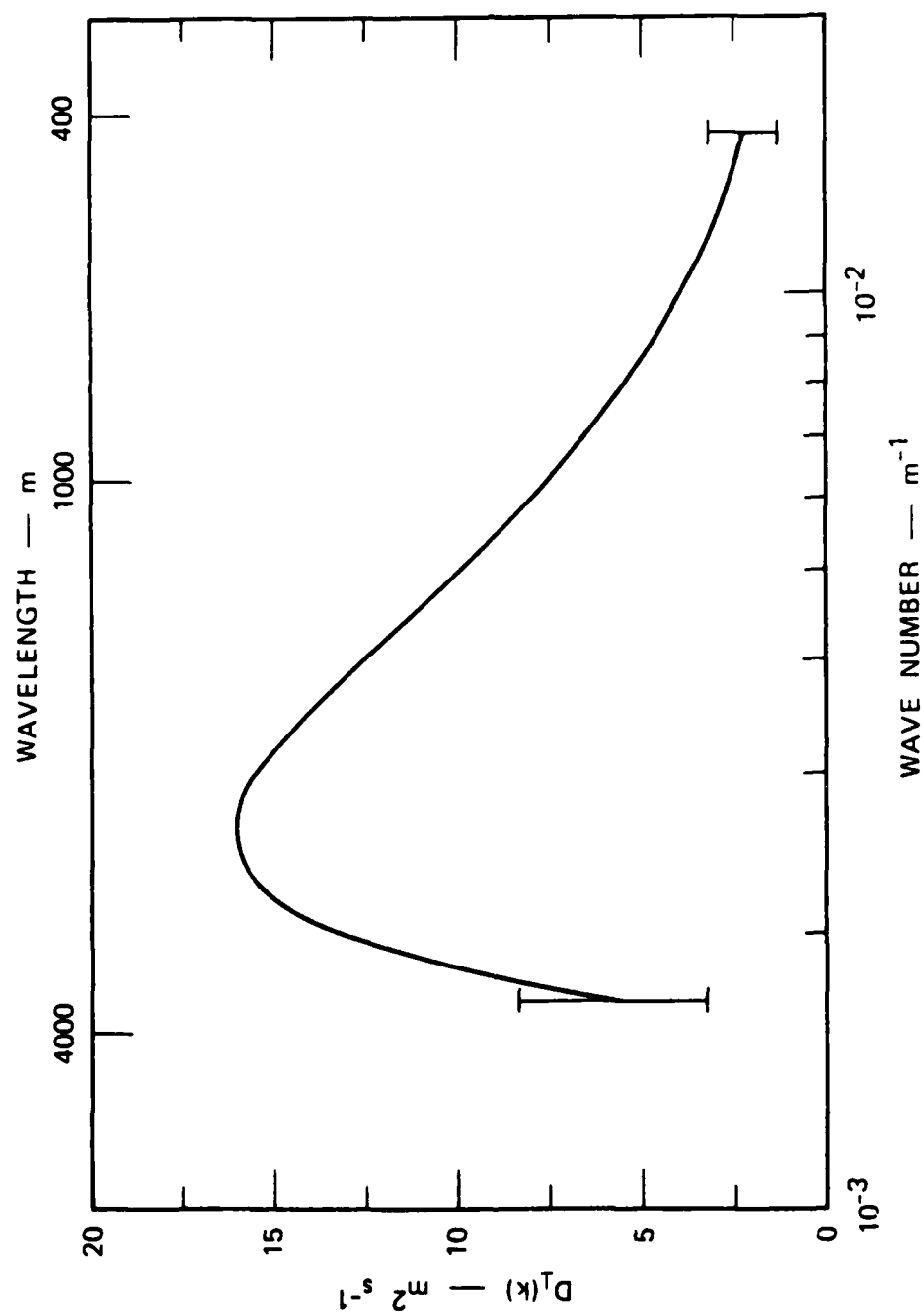
These arguments must remain somewhat speculative since turbulence theory is not as well developed in plasma applications. The data are not inconsistent with these concepts, however, provided an analog of the inertial subrange exists in plasmas.

### C. The Image Formation Process

An alternative mechanism that can lead to a scale size dependent loss of F layer structure has been proposed by Vickrey et al. [1983], who have investigated theoretically the formation of image striations in the E layer. Images result from the finite compressibility of the E region ion gas. Since the electron gas is incompressible in both the E and F regions, however, the image formation process redistributes electrons in altitude (along the magnetic field line) in a scale size selective way such that  $\nabla \cdot J \neq 0$ .

The model calculations of Vickrey et al. [1983], show that the saturated E region image spectrum has a peak near 1 km and scale size in agreement with near-equatorial rocket observations. Since the image irregularities grow at the expense of F layer plasma, Vickrey et al. [1983], argued that the "effective" diffusion rate in the F layer would reflect, at least qualitatively, the scale size dependence of the image formation process. The present observations are supportive of that argument. It should be kept in mind, however, that the observed spectrum is a balance between possibly scale-size dependent drivers and loss mechanisms. Nevertheless, the present observations are supportive of a "non-driven" situation in which the spectral evolution is determined purely by diffusion processes. A quantitative time-dependent cross-field diffusion model including magnetic field-line coupling effects is currently being developed and will be reported elsewhere.

Figure 7. An Empirically Derived Scale Size Dependent  
Diffusion Rate Based on Differencing Linear Fits  
to the Data in Figure 5.



## 5. SUMMARY

We have shown unique airborne observations of the spectral evolution of ionospheric structure in an isolated decaying plasma bubble. The temporal behavior of the decaying plume structure suggests that the loss mechanism of structure is scale size dependent. The effective cross-field diffusion rate deduced from the observations is scale size dependent and in qualitative agreement with the theoretical model described by Vickrey et al. [1983].

# REFERENCES

- Bernhardt, P. A., M. B. Pongratz, S. Peter Gary, and M. F. Thomsen, "Dissipation of Ionospheric Irregularities by Wave-Particle and Collisional Interactions," J. Geophys. Res., 87(A4), 2356-2362, April 1, 1982.
- Booker, H. G., "The Role of Acoustic Gravity Waves in the Generation of Spread F and Ionospheric Scintillations," J. Atmos. Terr. Phys., 41, 501, 1979.
- Burke, W. J., D. E. Donatelli, R. C. Sagalyn, and M. C. Kelley, Low Density Regions Observed at High Altitudes and their Connection with Equatorial Spread F," Planet. Space Sci., 27, 593, 1979.
- Costa, E., and M. C. Kelley, "On the Role of Steepened Structures and Drift Waves in Equatorial Spread F," J. Geophys. Res., 83, 4359, 1978a.
- Costa, E., and M. C. Kelley, "Linear Theory for the Collisionless Drift Wave Instability with Wavelengths near the ion Gyroradius," J. Geophys. Res., 83, 4365, 1978b.
- Gary, S. P., "Waveparticle Transport from Electrostatic Instabilities," Phys. Fluids., 23, 1193, 1980.
- Huba, J. D. and S. L. Ossakow, "Diffusion of Small-Scale Density Irregularities During Equatorial Spread F," J. Geophys. Res., 86., 9107, 1981.
- Kelley, M. C., "Nonlinear Saturation Spectra of Electric Fields and Density Fluctuations in Drift Wave Turbulence," Phys. Fluids., 25(6), 1002, June 1982. (c)
- Kelley, M. C., R. Pfaff, K. D. Baker, J. C. Ulwick, R. Livingston, C. Rino, and R. Tsunoda, "Simultaneous Rocket Probe and Radar Measurements of Equatorial Spread F--Transitional and Short Wavelength Results," J. Geophys. Res., 87, 1575, 1982. (c)
- Kelley, M. C., R. C. Livingston, C. L. Rino, and R. T. Tsunoda, "The Vertical Wave Number Spectrum of Topside Equatorial Spread F: Estimates of Backscatter Levels and Implications for a Unified Theory," J. Geophys. Res., 87(A7), 5217-5221, July 1, 1982.
- Livingston, R. C., "Heater-Generated Intermediate-Scale Irregularities: Spatial Distribution and Spectral Characteristics," Radio Sci., Accepted for Publication, 1983.

- Livingston, R. C., C. L. Rino, J. P. McClure, and W. B. Hanson, "Spectral Characteristics of Medium-Scale Equatorial F-Region Irregularities," J. Geophys. Res., 86, 2421, 1981.
- Ossakow, S. L., "Ionospheric Irregularities," Rev. Geophys. Space Phys., 17, 521, 1979.
- Rino, C. L., "A Power Law Phase Screen Model for Ionospheric Scintillation Studies, 1. Weak Scatter," Radio Sci., 14, 1135, 1979.
- Tsunoda, R. T., "Time Evolution and Dynamics of Equatorial Backscatter Plumes, 1. Growth Phase," J. Geophys. Res., 86, 139, 1981.
- Vickrey, J. F., M. C. Kelley, R. Pfaff and S. R. Goldman, "Low-Altitude Image Striations Associated with Bottomside Equatorial Spread F-- Observations and Theory," Accepted by J. Geophys. Res., 1983.
- Vickrey, J. F. and M. C. Kelley, "The Effects of a Conducting E Layer on Classical F Region Cross-Field Plasma Diffusion," J. Geophys. Res., 87, 4461, 1982.
- Weber, E. J., J. Buchau, and J. G. Moore, "Airborne Studies of Equatorial F Layer Ionospheric Irregularities," J. Geophys. Res., 85, 4631, 1980.



APPENDIX C

ELECTRICAL COUPLING EFFECTS ON THE TEMPORAL  
EVOLUTION OF F-LAYER PLASMA STRUCTURE

by

R. A. Heelis  
Center for Space Sciences, Physics Program  
The University of Texas at Dallas  
Richardson, TX

J. F. Vickrey and N. B. Walker  
Radio Physics Laboratory  
SRI International  
Menlo Park, CA

## ABSTRACT

A time-dependent model of a decaying F-region structure that includes electrical coupling along magnetic field lines to the E-region is examined. The temporal behavior of the ion concentration fluctuations is determined by the electric field in the coupled system as well as by the initial perturbation spectra and the E-region recombination rate. The formation of image structure in the E-region ion concentration affects the lifetime of F-layer structure in a scale size dependent way. Once an image is formed, the image amplitude and the driving F-region structure amplitude decay at the same rate. At large scale sizes,  $\lambda$  ( $\lambda = 2\pi/k$ ), this rate is proportional to  $k^2$  and the ratio of the temperatures in each region. At small scale sizes it depends on the E-region recombination rate and the temperatures of the two regions but is only very weakly dependent on  $k$ . The background E-region concentration determines the wave number beyond which the structure amplitude decay rate is almost independent of its scale size.

### 1. Introduction

Structure in the ion concentration and ambient electric field in the ionospheric F region exists at scale sizes ranging from global scales to centimeters. The sources of this structure vary with location. At the equator, for example, nighttime F-region structure results from instabilities that can dominate the plasma motion. At high latitudes, plasma instabilities are accompanied by structured particle precipitation, strong and highly structured magnetospheric convection electric fields and field-

aligned currents, all of which can produce variations in ion concentration [Fejer and Kelley, 1979]. The ultimate spectrum of fluctuations in ion concentration that is observed experimentally is a balance between the strength and scale-size dependencies of the sources and sinks of structure. In this paper, we concentrate on the scale-size dependence of one structure removal process--classical diffusion. Other processes (i.e., anomalous diffusion, non-linear mode coupling, etc.) may produce additional scale-size dependencies in the loss process that are not considered here. In our treatment, all scale sizes evolve independently.

We show that electrical coupling along magnetic field lines to the E layer can strongly impact the temporal evolution of a decaying F-region irregularity. The effects of E-region conductivity on the cross-field diffusion of plasma gradients in the F region has been studied by Vickrey and Kelley [1982]. They show that for an insulating E region, F-region diffusion may only proceed at the electron rate, but that the diffusion rate increases with increases in E-region conductivity. In the presence of a perfectly conducting E-region, F-region diffusion proceeds at the ion rate. Further work in this area has shown, however, that the presence of F-region irregularities can produce image irregularities in the E region by virtue of the polarization fields generated by the F-region structure. Vickrey et al. [1984], have shown evidence for the existence of such images in the equatorial ionosphere and have shown theoretically that their power spectrum has a peak near 1 kilometer. The situation they modeled was driven, not purely decaying as will be treated here. Nonetheless, since the E-region structure is driven at the expense of F-region structure, they argued that the effective F-region diffusion rate (or loss rate) must also be scale size dependent.

Here we examine quantitatively the effects of E-region image formation on the decay of F-region structure. We show that the loss rate for F-region structure is scale size dependent and investigate the factors that determine the scale size at which maximum loss occurs. The effects of E- and F-region conductivities and E-region recombination are included.

In what follows it is important to draw a distinction between an effective diffusion rate appropriate to a plasma structure and the plasma loss rate from that structure. An effective diffusion rate may be defined by assuming that the temporal evolution of a perturbation density,  $\Delta N$ , at some scale size,  $k$ , can be expressed in the form

$$\Delta N(k, t+\Delta t) = \Delta N(k, t) \exp[-\Delta t D(k, t)] \quad (1)$$

Here  $D(k, t)$  is the diffusion rate that in the classical case, [e.g., Vickrey and Kelley, 1982] is proportional to  $k^2$  and independent of  $t$ . Vickrey and Kelley [1982] have shown that if the effects of a conducting E region are considered but any structure is assumed to have a negligible effect on the local conductivity and its gradient, then the effective plasma diffusion rate is given by

$$D(k, t) = \frac{\Sigma_o^E}{\Sigma_o^E + \Sigma_o^F} d_{\perp} k^2 \quad (2)$$

where  $d_{\perp}$  is the local ion diffusion constant.

An alternative approach to the problem is to examine the plasma loss rate,  $\partial/\partial t [\Delta N(k, t)]$ . Such an approach is more appropriate here because the effective diffusion rate is a function of  $k$  and  $t$  and thus loses its usefulness.

## 2. Theoretical Background

The variation of plasma concentration,  $N$ , and velocity,  $V$ , as a function of time,  $t$ , in the ionosphere is determined by the continuity and momentum equations

$$\partial N / \partial t = P - L - \nabla \cdot (NV) \quad (3)$$

$$dV_i / dt = 1/N \nabla (NbT_i) + e(E + V_i \times B) - m_i \nu_{in} (V_i - U) \quad (4)$$

$$\partial V_e / \partial t = -1/N \nabla (NbT_e) - e(E + V_e \times B) - m_e \nu_{en} (V_e - U) - m_e \nu_{ei} (V_e - V_i) \quad (5)$$

Here  $P$  and  $L$  denote the production and loss rates for the ion species,  $T$  is the temperature, and  $E$  is the electric field.  $b$ ,  $e$ ,  $\nu$  and  $B$  are Boltzman's constant, the electronic charge, the collision frequency for momentum transfer and the earth's magnetic field vector respectively. Subscripts  $i$ ,  $e$  and  $n$  denote the particles, ion electron or neutral, to which the parameter refers. In Equation (4) we have neglected the effects of electron-ion collision on the ions and if we further assume that the neutral gas velocity  $U$  is identically zero, then manipulation of Equation (4) yields an expression for the ion Pedersen drift velocity.

$$V_{iP} = \frac{e v_i}{m(\Omega_i^2 + \nu_i^2)} E - \frac{b T \nu_i}{N m(\Omega_i^2 + \nu_i^2)} \nabla_P N \quad (6)$$

Here  $\nu_i$  refers only to ion neutral collisions, the subscript  $P$  denotes the component in the direction of the electric field (i.e., the Pedersen direction) and  $\Omega_i$  is the ion gyro-frequency.

Similar manipulation of Equation (5) yields an expression for the electron Pedersen drift.

$$V_{ep} = \frac{-e v_e}{m_e (\Omega_e^2 + \nu_e^2)} E - \frac{b T v_e}{N m_e (\Omega_e^2 + \nu_e^2)} \nabla_P N + R V_{ip} \quad (7)$$

Here  $\nu_e$  denotes the sum of the electron-neutral and electron-ion momentum transfer collision frequencies. The ion Pedersen drift is included because we cannot ignore electron ion collisions on the electrons and the multiplicative factor,  $R$ , is given by

$$R = \frac{\Omega_e^2 \nu_{ie} / \nu_{in} + \nu_{ei} \nu_e}{\Omega_e^2 + \nu_e^2} \quad (8)$$

Equations (6) and (7) are used to derive the Pedersen current.

$$J_p = [(1-R)\sigma_{ip} + \sigma_{ep}]E - e[(1-R)d_{i\perp} - d_{e\perp}] \nabla_P N \quad (9)$$

where

$$\sigma_{\ell p} = \frac{e^2 \nu_{\ell} N}{m_{\ell} (\Omega_{\ell}^2 + \nu_{\ell}^2)}$$

$$d_{\ell\perp} = \frac{b T_{\ell} \nu_{\ell}}{m_{\ell} (\Omega_{\ell}^2 + \nu_{\ell}^2)}$$

and the subscript  $\ell$  denotes either ions or electrons. Keeping in mind the validity of our assumptions and using appropriate values for the parameters, Equation (9) can be used at all altitudes.

In our study of the effects of E-region conductivity and images on F-region structure we adopt the simple geometry used by Vickrey and Kelley [1980] shown schematically in Figure 1. The E and F regions are considered

as slabs connected by vertical, infinitely conducting magnetic field lines. In both the E and the F regions, the Hall current is assumed to be divergence free.

If additionally we assume that no current flows out of the top of the F region or out of the bottom of the E region, then current continuity at the E-F region boundary demands that

$$\nabla_P J_P^E = - \nabla_P J_P^F \quad (10)$$

where J is the height-integrated current in the region, the subscript P again refers to the Pedersen direction and the superscripts E and F refer to the E and F regions respectively.

Equation (10) represents the fundamental electrical coupling relation by which E- and F-region structures and their associated electric fields affect each other. In order to examine the effects of such structure, we will always follow the bulk flow of the plasma in response to an imposed electric field. Because we treat only the linear problem there is no interaction between different scale sizes. Thus, we may consider the total ion-concentration structure and the electric-field structure it creates at each k as a simple wave form, such that

$$N(k) = N_0(1 + \Delta N/N_0(k)) \quad (11)$$

where

$$\Delta N(k) = \Delta N_0(k) \sin(kx + \theta_1) \quad (12)$$

and

$$E(k) = E_0(k) \sin(kx + \theta_2) \quad (13)$$



Here  $N_0$  is the background undisturbed ion concentration, the Pedersen direction is denoted by the coordinate  $x$ , and the scale size  $\lambda$  of the perturbation is given by  $\lambda = 2\pi/k$ . Then, using Equation (9) and assuming  $\Delta N_0(k)/N_0$  is independent of altitude in both the E and F regions, we can show for each region that

$$J_P(k) = \Sigma_0 \left[ 1 + \frac{\Delta N_0}{N_0}(k) \right] E_0(k) - e D_0 \nabla_P \left[ \frac{\Delta N_0}{N_0}(k) \right] \quad (14)$$

where

$$\Sigma_0 = \int_{\text{bottom}}^{\text{top}} [(1-R)\sigma_{1p} + \sigma_{ep}] dz$$

$$D_0 = \int_{\text{bottom}}^{\text{top}} [(1-R)d_{11} - d_{e1}] dz$$

The integrals extend over the altitude extent of each slab. Equations (10) and (14) yield an expression for the electric field throughout the system that can be linearized to the form

$$[\Sigma_0^F + \Sigma_0^E] E_0(k) = -ek [D_0^F \frac{\Delta N_0^F}{N_0^F}(k) + D_0^E \frac{\Delta N_0^E}{N_0^E}(k)] \quad (15)$$

Having established the electrical coupling properties of the region we now return to the local continuity Equation (3). In the F region we neglect the chemical loss process since it affects  $N_O$  and  $\Delta N_O$  equally and therefore will not affect  $\Delta N_O/N_O$ . Then, assuming all gradients are in the Pedersen direction, Equations (3) and (6) give

$$\frac{\partial}{\partial t} \overline{\Delta N_O^F(k)} = -k \frac{\Sigma_i^F}{e} E_O(k) - k^2 D_1^F \frac{\Delta N_O^F}{N_O^F}(k) \quad (16)$$

In the E region we assume that the background ion concentration  $N_O$  is maintained in equilibrium against chemical recombination with rate  $\alpha$ . Then retaining first order terms in  $\Delta N^E(k)$  we have

$$\frac{\partial}{\partial t} \overline{\Delta N_O^E(k)} = -\frac{\overline{\Delta N_O^E(k)^2}}{2\alpha(N_O^E)^2} \frac{\Delta N_O^E}{N_O^E}(k) - k \frac{\Sigma_i^E}{e} E_O(k) - k^2 D_1^E \frac{\Delta N_O^E}{N_O^E}(k) \quad (17)$$

In both equations bar quantities represent height integrals over the appropriate region, and the subscript i denotes the height integrated parameter applicable only to the ions. Substituting for the electric field  $E_O(k)$  in Equations (16) and (17) from Equation (15) yields equations that can be solved for  $\Delta N_O^F(k)$  and  $\Delta N_O^E(k)$  as a function of time. Such a procedure allows us to investigate the evolution of E- and F-region irregularity spectra from a given initial state assuming that there is no interaction between different scale sizes.

### 3. Results and Discussion

We have investigated the effects of E-region image formation on the decay of F-region structure by solving the continuity equations in the E and F layer. In these equations, the loss processes for the irregularities

are local cross field ion diffusion and additionally in the E layer, chemical recombination. The ambipolar diffusion electric field that opposes ion diffusion, however, has now changed from the local value,  $bT(\nabla N/N)/q$ , to include the electrical coupling between the E and F regions. Before illustrating the effects of this coupling in detail, it is worth pointing out some of its basic properties.

If the E-region conductivity is infinite, then the ambipolar electric field produced by an F-region structure is shorted out completely and the decay of F-layer structure depends only on the local ion diffusion constant  $d_{i\perp}^F$ . The existence of E-region structure does not affect this situation. At the other extreme, if we assume that the E-region conductivity is zero, then E-region structure cannot exist and we can show that the coefficient of  $\Delta N_0^F$  in Equation (16) depends only on the local electron diffusion coefficient  $d_{e\perp}^F$ .

Figure 2 illustrates the temporal evolution of F-region structure in the presence of a conducting E region in which no images are formed. Here we have arbitrarily selected an initial F-region spectrum that has the form [Vickrey et al., 1984]

$$\left| \frac{\Delta N_0^F}{N_0^F} \right|^2(k) = \frac{1}{1 + (k/k_c)^2} \quad (m) \quad (18)$$

where  $k_c$  was chosen to be  $3 \times 10^{-3} \text{ m}^{-1}$ . Panels A and B show the decay of this initial spectrum when the peak E-region ion concentration is  $10^5 \text{ cm}^{-3}$  and  $10^4 \text{ cm}^{-3}$  respectively. The curve labelled F shows the spectrum after a three hour decay period and intermediate spectra are shown every 5 min. The curve labelled I shows the state of the structure after 5 min. It

should be pointed out that the evolution of the spectral shape is a function of the initial shape chosen, however, by dealing with a spectrum we can contrast the behavior at different scale sizes. The initial spectral shape chosen is based on observed irregularity spectra, but in the physical situation we are modelling all scale sizes evolve independently.

In both cases illustrated in Figure 2, the irregularities decay in the manner expected from our previous discussion. That is,  $\Delta N^F/N_O^F$  decreases exponentially but the diffusion coefficient in the exponent is reduced from its local value by the ratio  $\Sigma_O^E/(\Sigma_O^F + \Sigma_O^E)$ . In case A this ratio is very close to unity since the E region is an extremely good conductor. The F-region decay therefore occurs at close to its maximum rate. In case B, however, the diffusion coefficient is reduced by approximately 50 percent and the associated reduction in the decay rate can be seen by comparing the initial temporal evolution and the final spectrum in the two cases. Figure 3 shows the rate of change of height-integrated density perturbation [i.e.,  $\partial/\partial t(\Delta N_O^F)$ ] for case B as a function of time and wave number,  $k$ . Several features of structure loss with a diffusion coefficient that is independent of time are evident. Most easily seen is the existence of a peak in the loss rate as a function of  $k$  and the movement of this peak to smaller values of  $k$  as time increases. It can be shown in fact that the maximum loss rate occurs at

$$k = (\tau D)^{1/2}$$

where  $D$  is the diffusion constant and  $\tau$  is the time over which the structure has decayed.

Vickrey et al. [1984] have pointed out that in order to significantly affect the behavior shown in Figures 2 and 3, an E-region image structure must develop substantially against chemical recombination. In a highly conducting E-region, with its associated high ion concentration, image amplitude is expected to be small. Figure 4 shows this to be the case. It illustrates the temporal evolution of F-region structure and its associated E-region image (in the same format and) under the same initial conditions as Figure 2A. Comparison of the F-region spectra in Figures 4 and 2A show that the E-region image, despite its small amplitude, significantly affects the F-region decay. This example also illustrates some fundamental features of the image structure and its temporal evolution that may be understood as follows.

The image formation process has been described in some detail by Vickrey et al. [1984]. The pressure gradient associated with F-region plasma structure causes plasma diffusion in a direction opposite to the gradient in electron number density. The resulting polarization electric field maps along the magnetic field to the E layer where the ion gas is relatively compressible. If at some altitude in the E layer, the ions are compressed together by this electric field at a rate  $\gamma_{\text{comp}}$  that is more rapid than they either diffuse away or recombine (at the rates  $\gamma_{\text{diff}}$  and  $\gamma_{\text{chem}}$  respectively) then an "image" structure will form. These rates can be identified with the second, third and first terms respectively in Equation (17).

The evolution of the E-region image structure shown in Figure 4 can be understood by considering the modelled situation. We begin with some perturbation density in the F region. This perturbation produces an image

structure in the E region and they both evolve; the E region growing and the F region decaying until

$$\frac{\partial}{\partial t} (\overline{\Delta N_c^E}) = 0$$

This condition is satisfied when

$$\frac{\Delta N_o^E / N_o^E(k)}{\Delta N_o^F / N_o^F(k)} = \frac{k^2 \Sigma_1^E D_o^F}{2\alpha (N_o^E)^2 (\Sigma_o^F + \Sigma_o^E) + k^2 \Sigma_o^E D_1^E} \quad (19)$$

From that point on, both spectra decay. We note that after five minutes both E- and F-region spectra are seen to decay in Figure 4, implying that the E-region growth is very rapid and the structure reaches its maximum amplitude in less than 5 min. Subsequently both the E- and F-region structure will decay and by applying Equation (19) in Equations (16) and (17), we can show that

$$\frac{\partial}{\partial t} \left[ \log \frac{\Delta N_o^F}{N_o^F} (k) \right] = \frac{\partial}{\partial t} \left[ \log \frac{\Delta N_o^E}{N_o^E} (k) \right] = \frac{-2k^2 D_1^F \Sigma_o^E \alpha (N_o^E)^2}{N_o^F [2\alpha (N_o^E)^2 (\Sigma_o^F + \Sigma_o^E) + k^2 \Sigma_o^E D_1^E]} \quad (20)$$

Examination of Equation (20) shows that for large scale sizes (small k) the irregularity amplitude will decay so that

$$\frac{\partial}{\partial t} \left[ \log \frac{\Delta N_o^F}{N_o^F} (k) \right] = - \frac{k^2 D_1^F \Sigma_o^E}{N_o^F (\Sigma_o^E + \Sigma_o^F)} \quad (21)$$

At small scale sizes (large k) the irregularity spectral shapes will be preserved as they decay since

$$\frac{\partial}{\partial t} \left[ \log \frac{\Delta N_O^F}{N_O^F} (k) \right] = - \frac{2\alpha (N_O^E)^2}{N_O^F} \frac{D_1^F \Sigma_O^E}{\Sigma_O^F D_1^E} \quad (22)$$

As has been pointed out by Vickrey and Kelley [1982], the amplitude of an image structure is strongly dependent on the E-region recombination rate or identically the E-region background ion concentration. This can be seen from Equation (19) and by contrasting Figures 5 and 4. In these figures, which correspond to maximum E-region concentrations of  $10^4 \text{ cm}^{-3}$  and  $10^5 \text{ cm}^{-3}$  respectively, the peak amplitudes of the image irregularities differ by about 20 dB. The temporal behavior of the image spectrum in Figure 5 appears markedly different from that of Figure 4, but the differences simply reflect the characteristics of Equations (21) and (22). As the effective recombination rate  $\alpha (N_O^E)^2$  decreases, the k value beyond which the spectral shape is preserved moves to smaller k (longer wavelengths) leading to a preserved spectral shape over much of the scale-size range contained in the figure. These effects can be emphasized by allowing the E-region recombination rate to become zero. In this case the E-region irregularity will continue to grow until

$$\frac{\Delta N_O^E / N_O^E (k)}{\Delta N_O^F / N_O^F (k)} = \frac{T^F}{T^E} \quad (23)$$

where we have assumed that the ion and electron temperatures are equal at all heights. This condition was also derived by Vickrey and Kelley [1982] by determining the E region gradient necessary to produce an electric field,  $E_O$ , that is equal to the ambipolar diffusion electric field that F region ions would experience if the E layer were nonconducting. Once condition (23) is achieved, the E and F-region spectra decay only at the

slow electron diffusion rate. This behavior is seen in Figure 6. It should be noted that at large scale sizes (small  $k$ ) the time required to reach the equilibrium condition (23) is much longer than the 3 hour period we have studied, and so the E-region spectrum is continually growing in this figure. Finally, we note that the E-region image spectrum that we are examining depends strongly on the F-region driving spectrum and its evolution. Nevertheless it can be shown that a maximum in the E-region spectrum must occur for all reasonable (i.e., monotonically decreasing) F-region spectral shapes, and that it can only occur at a place where the F-region spectral slope is less than  $k^{-2}$ . This would typically occur at scale sizes between 1 km and 5 km.

The effects of image formation on the rate at which an F-region perturbation density is lost can be seen in Figure 7. Contours of constant perturbation loss rate are shown as a function of  $k$  and  $t$  for the same ionospheric conditions that apply to Figure 5. This figure should be compared with Figure 3, which is appropriate for the same conditions but assumes the image structure does not form. As is evident from the image spectrum, the maximum F-region perturbation loss occurs where the maximum E-region growth appears and for the conditions chosen here that scale size remains relatively constant with time. A comparison of the absolute loss rates in Figures 3 and 7 can be deceiving, since in addition to the coupling effects themselves, the loss rate is also dependent on the magnitude of the perturbation density. In fact, an examination of Figures 2A and 4 shows that the image formation process tends to preserve structure in the F region at all scale sizes, although the scale size at which preservation becomes significant depends upon the background E-region number density.



Figure 8 shows contours of the ratio of F-region spectral amplitudes that result from our calculations when decay is allowed to proceed with and without the formation of E-region images. Little change in the temporal evolution is seen for large scale sizes, and indeed the loss rate in Equation (21) is in fact identical to that obtained for the case of no image formation. At smaller scale sizes the decaying spectral amplitude may be many tens of dB higher than one would expect if the image formation process is neglected.

#### 4. Conclusions

We have presented a model of the temporal evolution of a decaying spectrum of F-region irregularities that includes electrical coupling along magnetic field lines to a compressible E-region plasma. The existence of F-region structure induces irregularities in an initially uniform E layer in a scale size selective way. Because E-region images form at the expense of F layer plasma, the  $k$  dependence of the F-region structure loss rate is strongly influenced by coupling to the E layer. The density gradients associated with image structure impact the driving electrostatic field and parallel current that couple the two layers. The net result is that images prolong the lifetime of F layer structure in a scale size dependent way.

We have shown that the amplitude of the E-region image irregularities are related to the driving F-region irregularity in a way that allows the image spectral amplitude to be a constant multiple of the F-region spectral amplitude for all wave numbers beyond a particular value. This condition

may be routinely achieved where the E-region density is low (i.e., in the winter polar cap, in equatorial spread-F or in barium clouds). In this condition, the E and F layer spectra decay with a common spectral shape at a rate determined by E-region chemistry.

#### ACKNOWLEDGMENTS

This work is supported by Air Force Geophysics Laboratory contract F19628-83-K-0022 and NASA Grant NGR 44-004-120 to the University of Texas at Dallas and by the Air Force Office of Scientific Research and the Defense Nuclear Agency under contracts F49620-83-K-0025 and DNA001-83-C-0034.

#### REFERENCES

- Fejer, B. G., and M. C. Kelley, "Ionospheric Irregularities," Revs. Geophys. and Space Phys., 18(2), 401-454, 1980.
- Vickrey, J. F., M. C. Kelley, R. Pfaff and S. R. Goldman, "Low-Altitude Image Striations Associated with Bottomside Equatorial Spread F-- Observations and Theory," in press, J. Geophys. Res., 1984.
- Vickrey, J. F., and M. C. Kelley, "The Effects of a Conducting E Layer on Classical F Region Cross-Field Plasma Diffusion," J. Geophys. Res., 87(A6), 4461-4468, 1982.

AD-A142 648

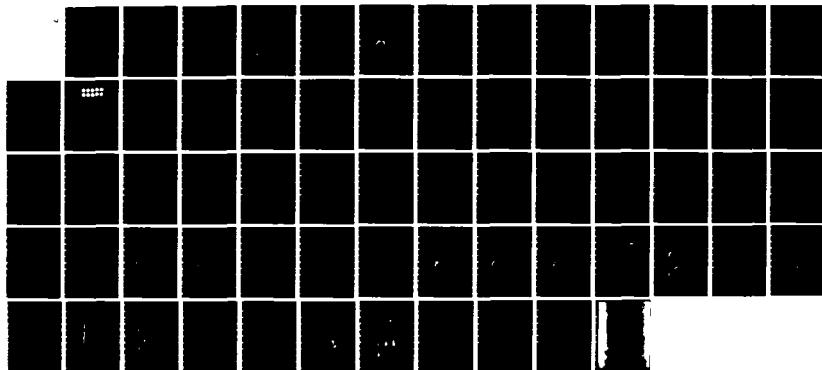
HIGH-LATITUDE IONOSPHERIC IRREGULARITIES(U) SRI  
INTERNATIONAL MENLO PARK CA J F VICKREY ET AL.  
10 MAY 84 AFOSR-TR-84-0510 F49620-83-K-0025

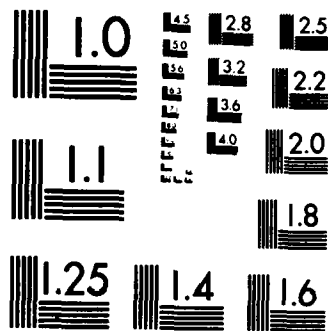
2/2

UNCLASSIFIED

F/G 4/1

NL





MICROCOPY RESOLUTION TEST CHART  
NATIONAL BUREAU OF STANDARDS-1963-A

### Figure Captions

- Fig. 1. Schematic illustration of simple cylindrically symmetric geometry assumed in the model
- Fig. 2. Temporal evolution of F-region structure from an initial arbitrary spectrum of irregularity amplitudes. Different evolutions depend only on the effective E-region conductivity
- Fig. 3. Loss rate of the F-region column content associated with the structure in figure 2b.
- Fig. 4. Temporal evolution of F-region and E-region structure from an initial arbitrary spectrum of irregularities in the F-region. F-region structure is produced by the image formation process in a background concentration  $10^5 \text{ cm}^{-3}$  and conditions are identical to those for figure 2a.
- Fig. 5. Temporal evolution of F-region and E-region structure from an arbitrary spectrum of F-region irregularities. E-region structure is produced by the image formation process in a background concentration of  $10^4 \text{ cm}^{-3}$ . Conditions are identical to these in figure 2b.
- Fig. 6. Same as figure 5 except that the E-region recombination rate is reduced to zero.
- Fig. 7. Loss rate of the F-region column content associated with the structure in figure 5. Note a peak in the loss rate at a scale size that remains relatively constant in time.
- Fig. 8. Temporal evolution of the ratio of F-region structure amplitude when the image formation process is neglected to that when it is included. Structure is preserved at all scale sizes although little effect is seen at very large scale sizes. Conditions are appropriate to figures 2b and 5.

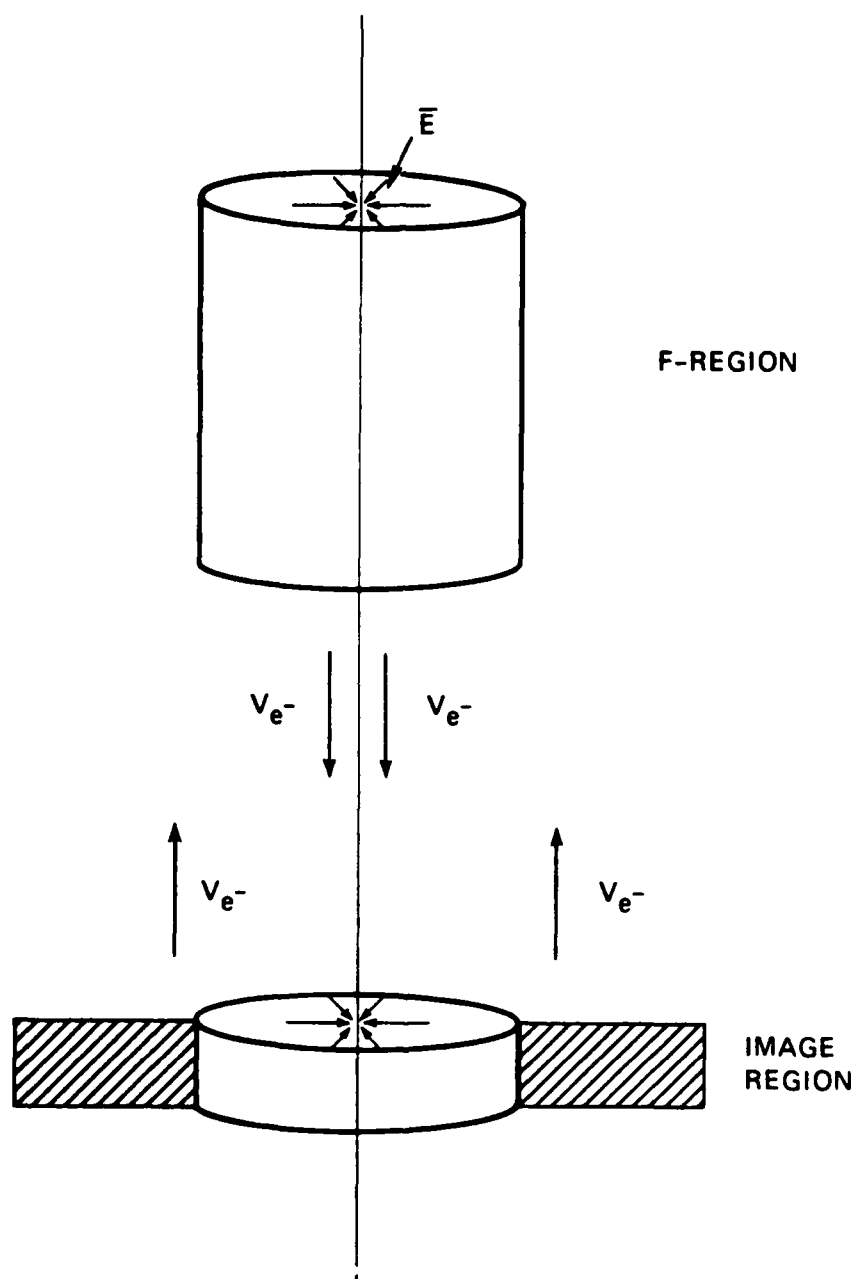


Figure 1. Schematic Illustration of Simple Cylindrically Symmetric Geometry Assumed in the Model.

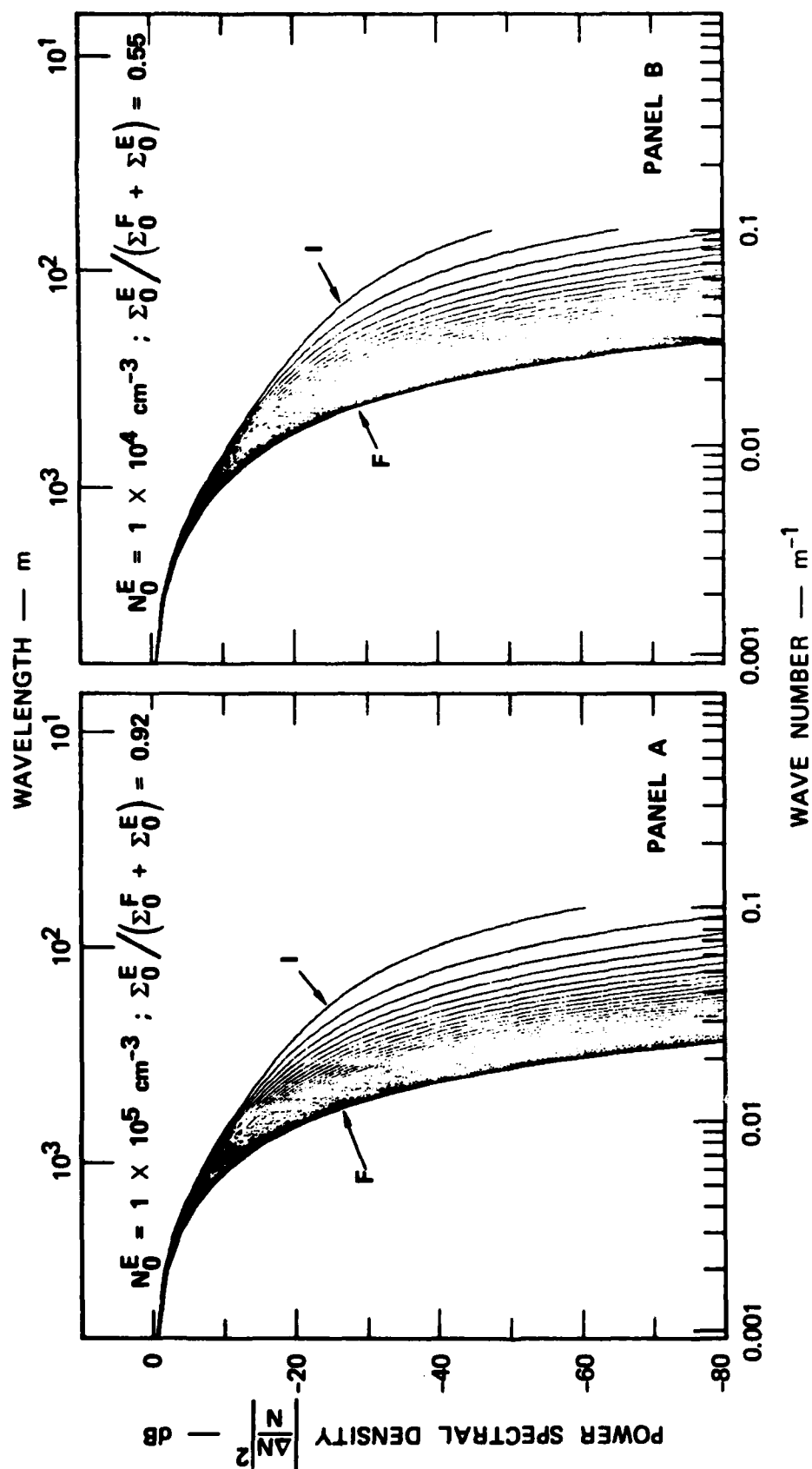


Figure 2. Temporal Evolution of F-region Structure from an Initial Arbitrary Spectrum of Irregularity Amplitudes. Different evolutions depend only on the effective E-region conductivity.

# F-REGION STRUCTURE LOSS RATE — $\text{m}^{-2} \text{s}^{-1} \times 10^{10}$

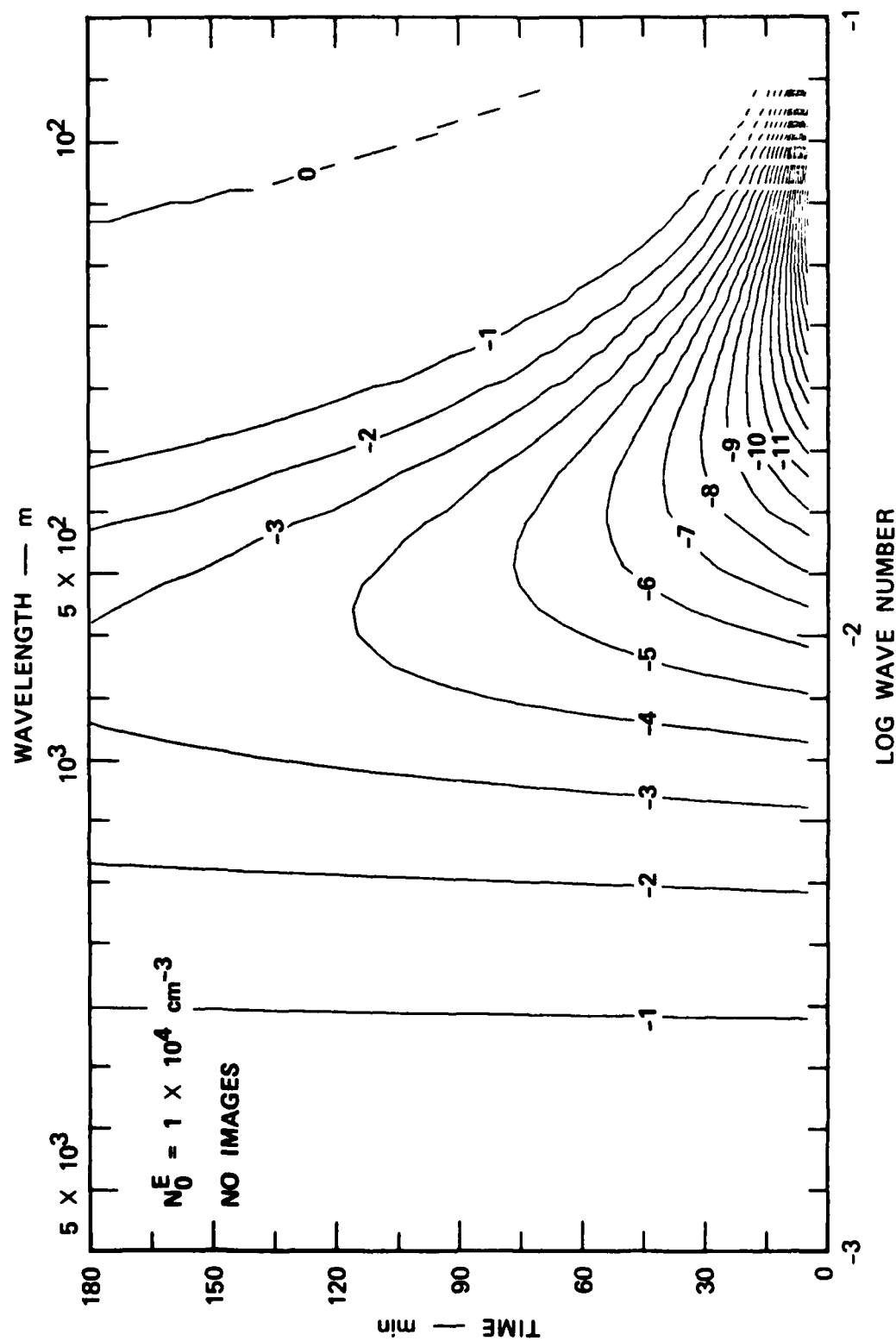


Figure 3. Loss Rate of the F-Region Column Content Associated with the Structure in Figure 2B.



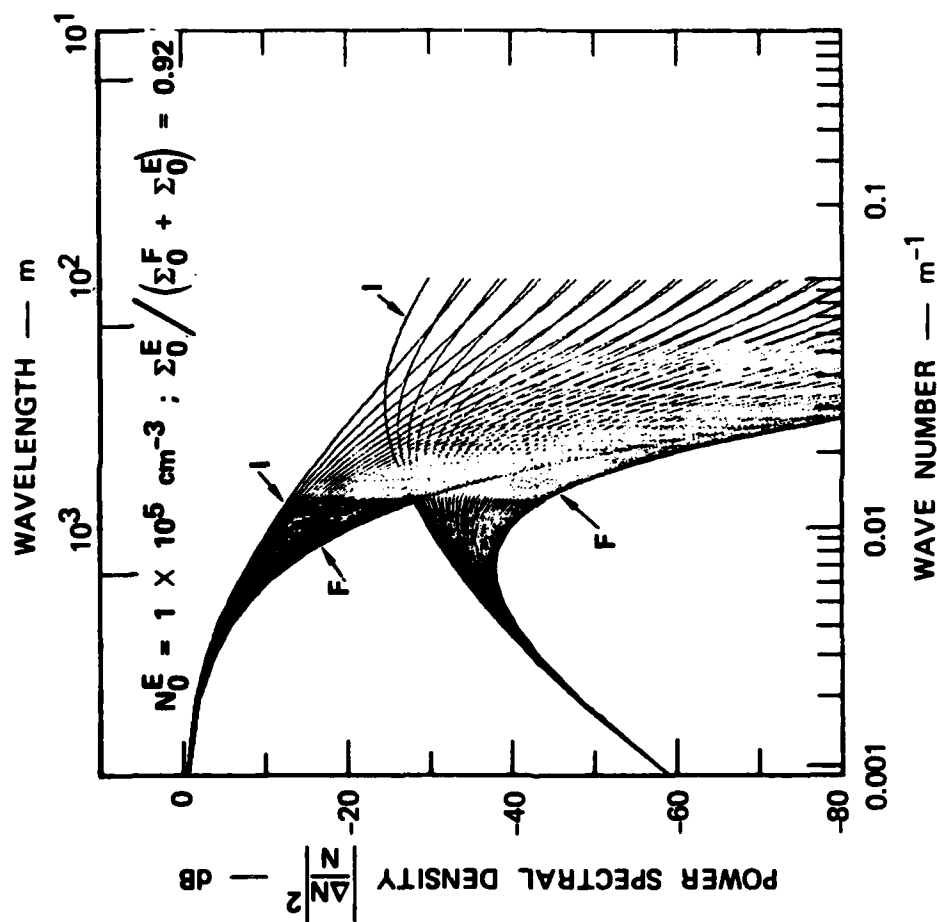


Figure 4. Temporal Evolution of F-Region and E-Region Structure from an Initial Arbitrary Spectrum of Irregularities in the F-Region. F region structure is produced by the image formation process in a background concentration  $10^5 \text{ cm}^{-3}$  and conditions are identical to those for Figure 2A.

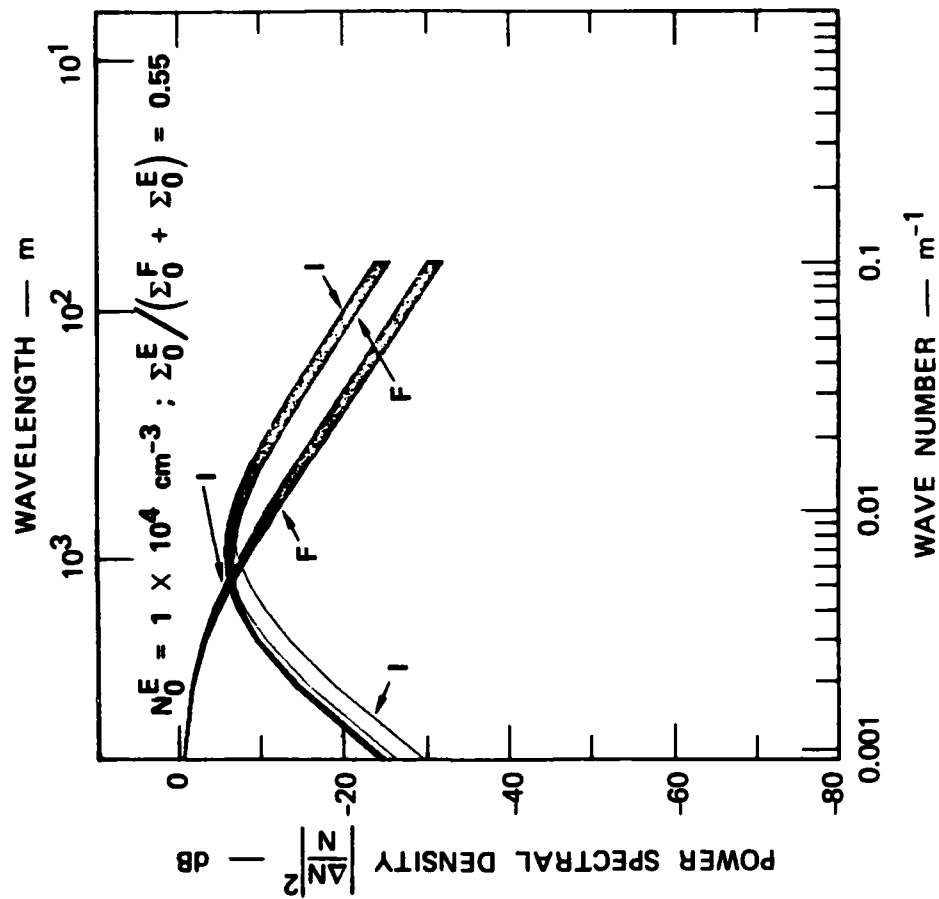


Figure 5. Temporal Evolution of F-Region and E-Region Structure from an Arbitrary Spectrum of F-Region Irregularities. E-region structure is produced by the image formation process in a background concentration of  $10^4 \text{ cm}^{-3}$ . Conditions are identical to these in Figure 2B.

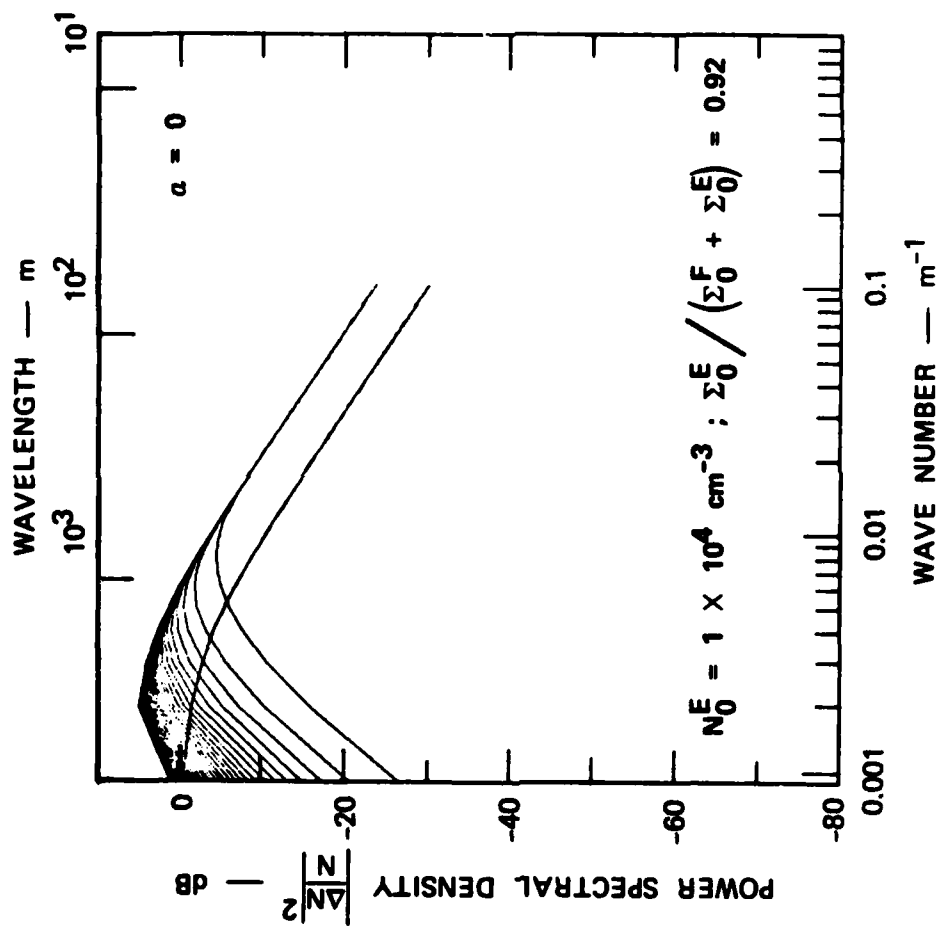


Figure 6. Temporal Evolution of F-Region and E-Region Structure from an Arbitrary Spectrum of F-Region Irregularities. E-region recombination rate is reduced to zero.

# F-REGION STRUCTURE LOSS RATE — $m^{-2} s^{-1} \times 10^{10}$

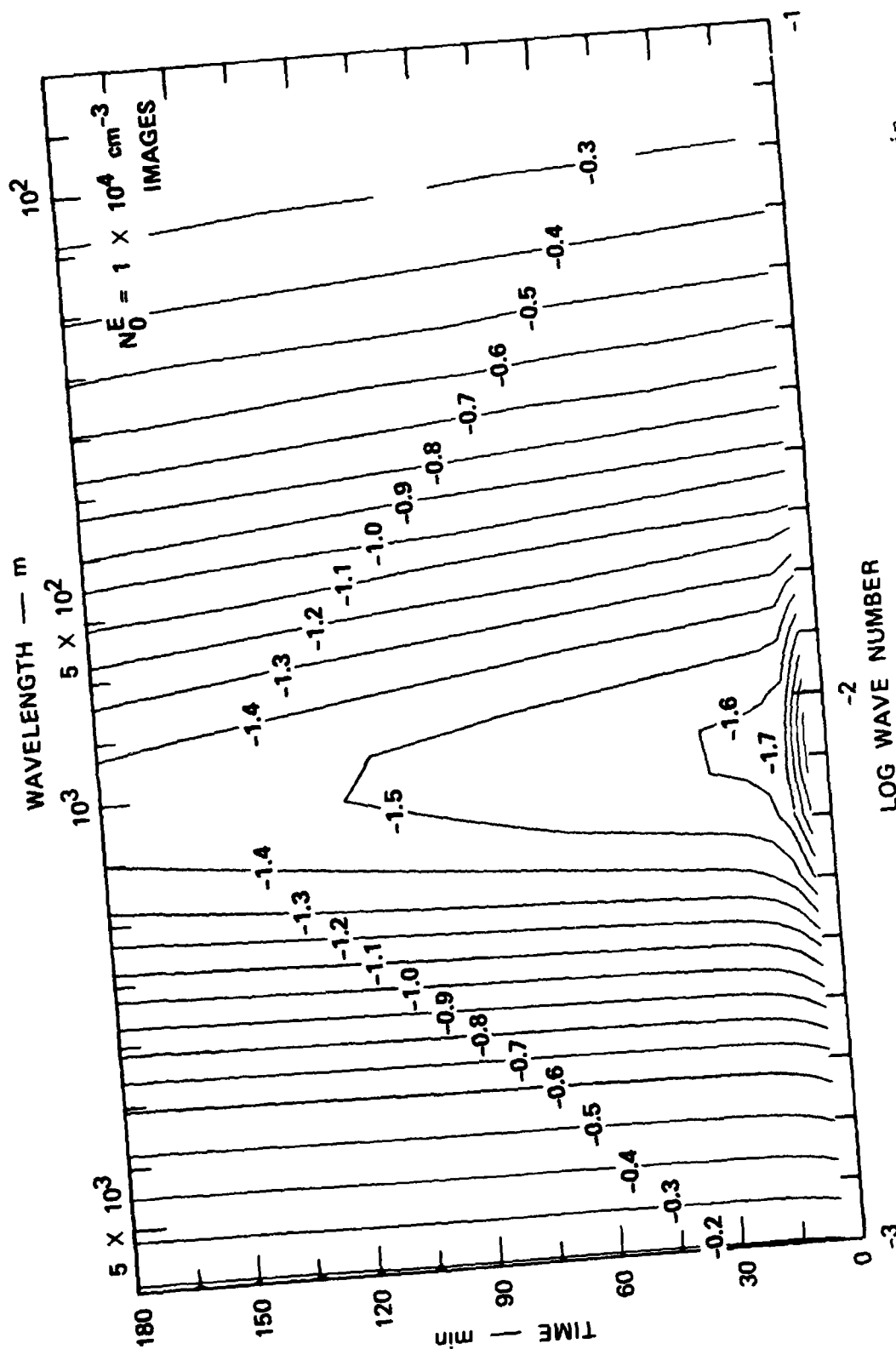


Figure 7. Loss Rate of the F-Region Column Content Associated with the Structure in Figure 5. Note a peak in the loss rate at a scale size that remains relatively constant in time.

$$\frac{|\Delta N|^2 |IMAGE|}{|\Delta N|^2 |NO IMAGE|} \text{ --- dB}$$

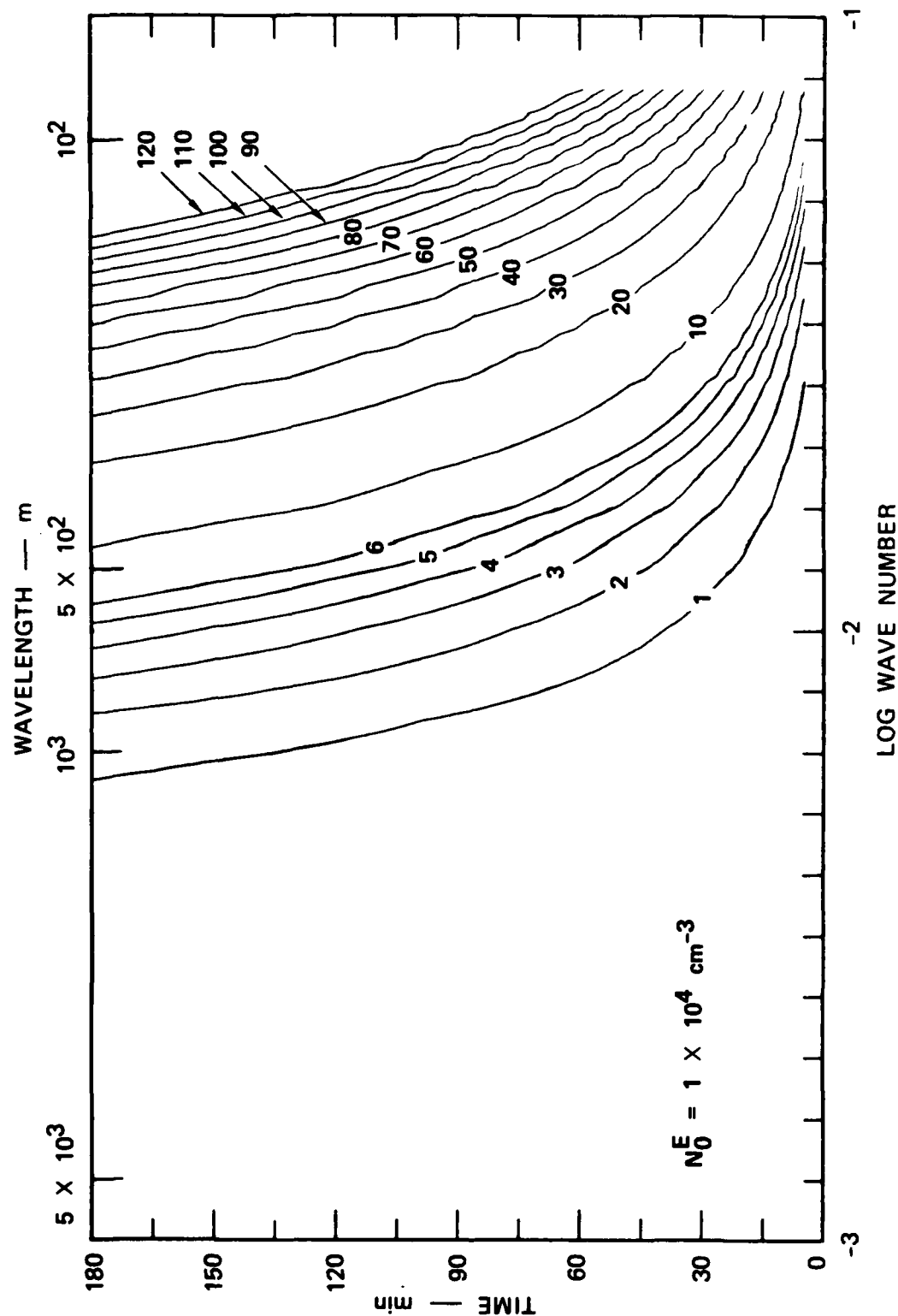
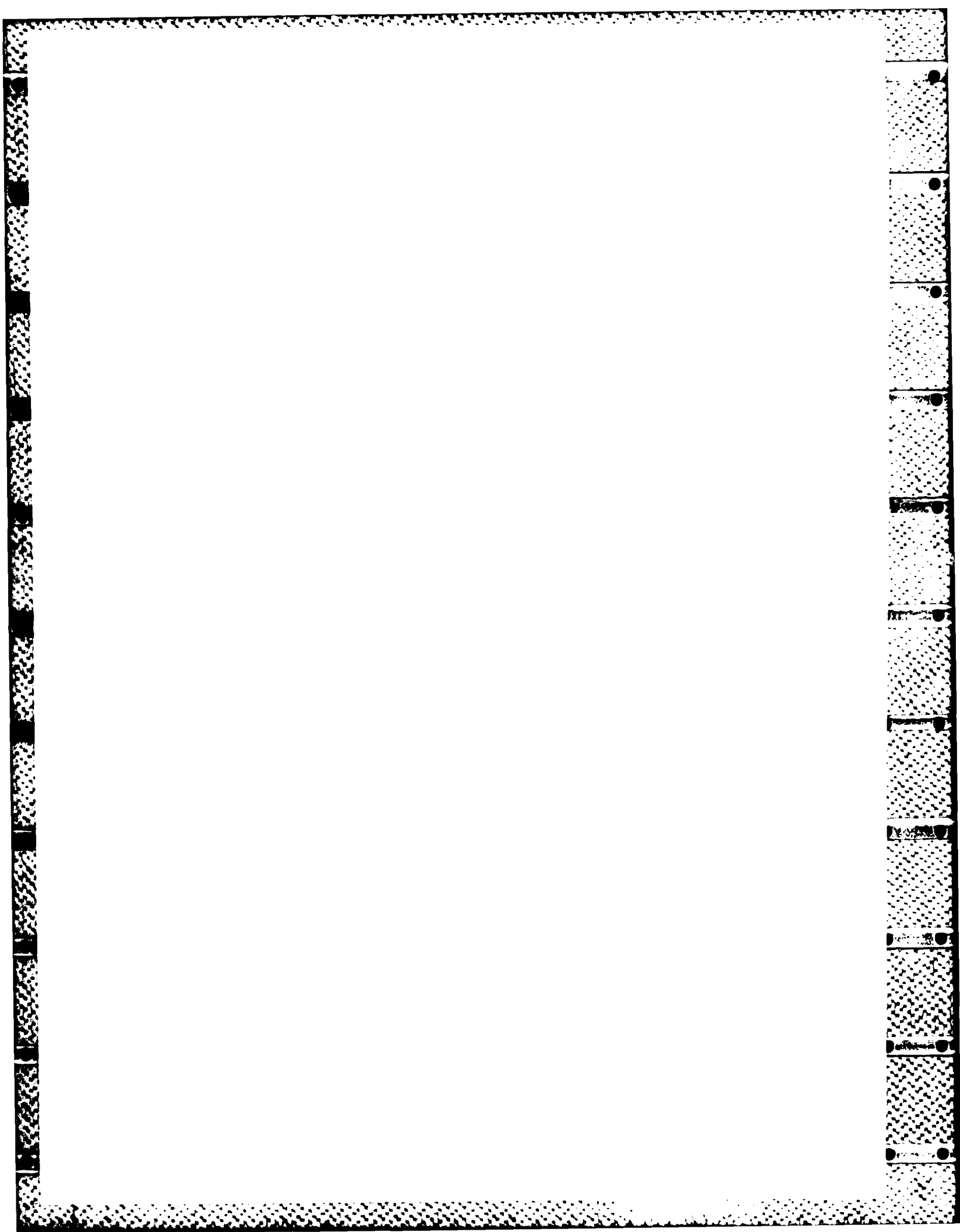


Figure 8. Temporal Evolution of the Ratio of F-Region Structure Amplitude when the Image Formation Process is Neglected to that when it is Included. Structure is preserved at all scale sizes although little effect is seen at very large scale sizes. Conditions are appropriate to Figures 2B and 5.



APPENDIX D

## Aurora and Electrojet Configuration in the Early Morning Sector

Y. KAMIDE,<sup>1,2</sup> R. M. ROBINSON,<sup>3</sup> S.-I. AKASOFU,<sup>4</sup> AND T. A. POTEMRA<sup>5</sup>

Nearly simultaneous data from the Chatanika radar, the TRIAD satellite, and the IMS Alaska meridian chain of magnetic and auroral observatories are utilized to examine the spatial relationship among auroras, field-aligned currents, ionospheric electric fields, and conductivities in the westward electrojet in early morning hours. The westward electrojet is found to be dominated by one of two different quantities, depending on latitudinal locations in this local time sector. The poleward half of the electrojet is governed by a relatively intense southward electric field. On the other hand the Hall conductivity is the dominant factor in controlling the electrojet current in the equatorward half. The electrojet center appears to be located within the region of the upward field-aligned current. Major auroral activity is present only in the equatorward half of the electrojet in which the upward field-aligned current prevails, although it appears that the latitudinal variations of the conductivity and current intensity are not well related within that region.

## 1. INTRODUCTION

Significant progress in our understanding of the large-scale distribution of field-aligned currents and their location relative to the auroral electrojets was made during the last decade. This was primarily due to the development of vector magnetometers onboard polar-orbiting satellites and ground-based radars at auroral latitudes. As pointed out by Kamide [1981] and Baumjohann [1983], however, most of the previous studies have been made only in the evening to premidnight sectors, in spite of the fact that current and field patterns depend statistically on local time [e.g., Kamide and Vickrey, 1983]. Only few papers [Kamide et al., 1976; de la Beaujardiere et al., 1977; Sulzbacher et al., 1980; Zanetti et al., 1983] have dealt with the relationship between the electrojet and field-aligned current configurations in the morning sector, although these studies were somewhat limited in that multiple ionospheric parameters at more than one site along a meridian were not available.

By using rocket and satellite data, two most recent studies [Senior et al., 1982; Ziesolleck et al., 1983] have addressed the question of how the connection of the auroral electrojets and field-aligned currents relates to different auroral features in early morning hours. In particular, Senior et al. have presented simultaneous observations of ionization, conductivities, electric fields, and currents made by the Chatanika incoherent scatter radar. They have combined the Chatanika radar and TRIAD satellite data and found that the latitudinal extent of the westward electrojet covers both the downward (region 1) and upward (region 2) field-aligned current regions. However, in determining the latitudinal breadth of the electrojet, their conclusion was based only on the  $H$  component of ground-based magnetometers.

The purpose of this brief report is to examine in detail three-component magnetic perturbations from the IMS Alaska chain of magnetometers and the auroral distribution from two all-sky cameras near the radar site. This data set allows us to obtain a new insight in mapping the aurora-current configurations in early morning hours.

## 2. DATA SET

Senior et al. [1982] have listed six cases in which TRIAD traversed over Alaska, measuring magnetic effects of field-aligned currents, when the Chatanika radar was in operation. For two intervals (January 10 and 22, 1981) out of the six cases examined by Senior et al., all-sky photographs and IMS magnetometer records were available, and substorms were in progress.

The operating mode of the Chatanika radar employed for measurements discussed in this paper consists of elevation scans in magnetic meridian. Details on the experimental technique were described in Vondrak and Baron [1976]. Our basic data set from the radar measurements includes latitudinal profiles of the electric field vectors in two dimensions and the height-integrated Pedersen ( $\Sigma_P$ ) and Hall ( $\Sigma_H$ ) conductivities as well as the horizontal ionospheric current vector. Error bars in deducing these properties from the radar data are discussed in detail by Robinson et al. [1982] and Kamide and Vickrey [1983].

A complete description of the triaxial magnetometer onboard the TRIAD satellite, which is in a nearly circular orbit at about 800 km, is given in Armstrong and Zmuda [1973]. The original  $A$ ,  $B$ , and  $Z$  components referred to satellite attitude and are converted in this paper into the geomagnetic east  $B_x$ , north  $B_y$ , and vertical  $B_z$  components.

The Alaska meridian chain of magnetometers and all-sky cameras have been operated from the beginning of the IMS. To compare properly the chain magnetometer records with satellite and radar data, the perturbations in the  $H$ ,  $D$ , and  $Z$  components were plotted as a function of invariant latitude. Such profiles were then interpreted on the basis of the standard technique [cf. Kisabeth and Rostoker, 1977] in deducing the center and the latitudinal width of the auroral electrojet. It is possible then to locate the auroral electrojet to an accuracy of 0.5–1° in latitude.

## 3. RESULTS

On January 10, 1981, the TRIAD satellite traversed southward along a geographic longitude ~142°W. At closest approach it was about 300 km east of the Chatanika radar. In Figure 1 we show  $H$  component magnetograms from the Alaska meridian chain of stations. As indicated by the vertical line, simultaneous observations by radar and satellite occurred during the maximum epoch of a weak substorm. It took 13 min (1256–1310 UT) for the radar to cover the  $E$  region in invariant latitude range from 62° to 69°. The field-aligned current distribution within this latitudinal range was scanned

<sup>1</sup> NOAA Space Environment Laboratory.<sup>2</sup> Now at Kyoto Sangyo University.<sup>3</sup> Radio Physics Laboratory, SRI International.<sup>4</sup> Geophysical Institute, University of Alaska.<sup>5</sup> Applied Physics Laboratory, Johns Hopkins University.

Copyright 1984 by the American Geophysical Union.

Paper number 3A1520.  
0148-0227/84/003A-1520\$02.00



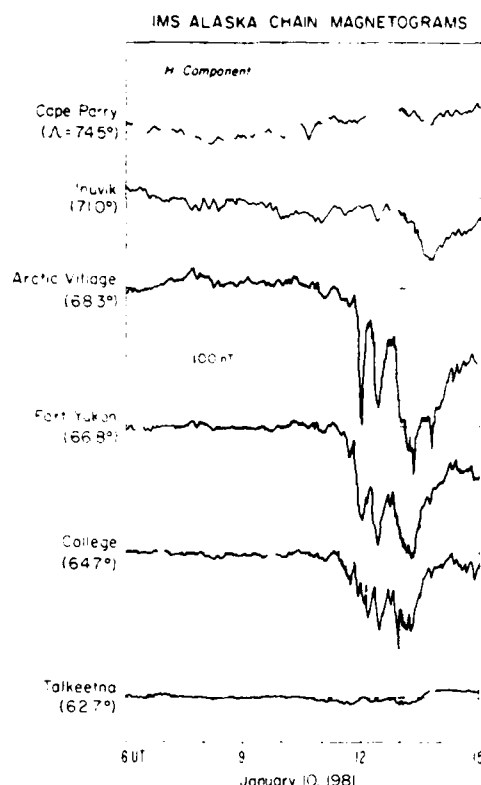


Fig. 1.  $H$  component records from the IMS Alaska meridian chain of six magnetometers for January 10, 1981. Invariant latitude is shown for each station. The vertical line indicates a time interval for which detailed latitudinal profiles of ionospheric parameters and field-aligned currents are given in Figure 2.

by TRIAD at an earlier time (1255–1257 UT) of the entire radar scan. As is evident from Figure 1 the substorm activity reached almost the maximum stage below the latitude of Fort Yukon when the radar-satellite measurements were made, whereas the electrojet intensity was still growing at Inuvik and Arctic Village. In particular, the magnitude of the  $H$  component disturbance increased  $\sim 100$  nT at Arctic Village in the 15-min period (1255–1310 UT).

Figure 2 compares the three latitudinal profiles: Chatanika radar data, ground-based magnetic perturbations, and TRIAD magnetic data. Note that measurement of the electric field can be made when the radar is pointing in the vicinity of the magnetic zenith. The ground magnetic profiles are shown at two UT's by using two different lines. The electrojet extent was then determined by the latitudinal distribution of  $\Delta H$  and  $\Delta Z$ ;  $\Delta D$  was almost zero at all stations within the field of view of the radar. In spite of the rapid changes in the  $H$  component at some stations, the northern and southern boundaries and center of the electrojet did not undergo a significant change during the 15-min interval. Note that since the  $H$  component profiles do not have a sharp peak in this particular case, the inference of the electrojet center relied heavily on the  $\Delta Z$  profile. This inferred electrojet extent (indicated by a horizontal bar) is generally consistent with the  $j_z$  profile deduced from the Chatanika radar data, which, however, includes many spatial fluctuations. The TRIAD information is shown only in terms of the geomagnetic east-west component, since perturbations in other components are negligibly small.

With these provisions in mind, several points of interest are noticeable from Figure 2. First, the radar data indicate that the "westward" electrojet was flowing southwestward, a typical feature in the early morning sector. Furthermore, as pointed out by *Senor et al.* [1982] and *Kamide and Vickrey* [1983], the peak of the Hall conductivity and the peak of the southward electric field do not occur at the same latitude. There are two physically different regions across the westward electrojet in this local time sector: the conductivity-dominant and the electric-field-dominant regions. The equatorward half of the radar field of view features a high Hall conductivity ( $\Sigma_H \sim 30$  mho) and a relatively small electric field ( $E_z \sim 10$  mV/m), while the poleward half is characterized by a large electric field (30 mV/m) and a relatively low Hall conductivity. Second, the region of intense auroral precipitation creating the high  $\Sigma_H/\Sigma_P$  ratio (peaked at  $\sim 66^\circ$ ) does not necessarily coincide with the region of the strongest electrojet, which was located at  $\sim 67^\circ$  to  $67.5^\circ$ . This is somewhat different from what one might have expected. Note that although  $\Delta H$  and  $\Delta Z$  appear to be consistent with each other, the determination of the electrojet center is not without problems. As noticed, for example, by *Hughes and Rostoker* [1979] and *Akasofu et al.* [1980], the  $\Delta Z$  profiles show a marked asymmetry across the crossover with the  $+\Delta Z$  extremum being larger than  $-\Delta Z$  extremum. From an extensive calculation of model three-dimensional current systems, *Hughes and Rostoker* interpreted that this asymmetry in  $\Delta Z$  in the morning sector is due to the effects of the southward closing current system in the westward electrojet region, but there is the possibility that a uniform  $+\Delta Z$  (of unknown origin) is superimposed on the electrojet  $\Delta Z$  contribution. In the latter case the electrojet center may not be located at the  $Z = 0$  crossover but at the  $\Delta Z =$

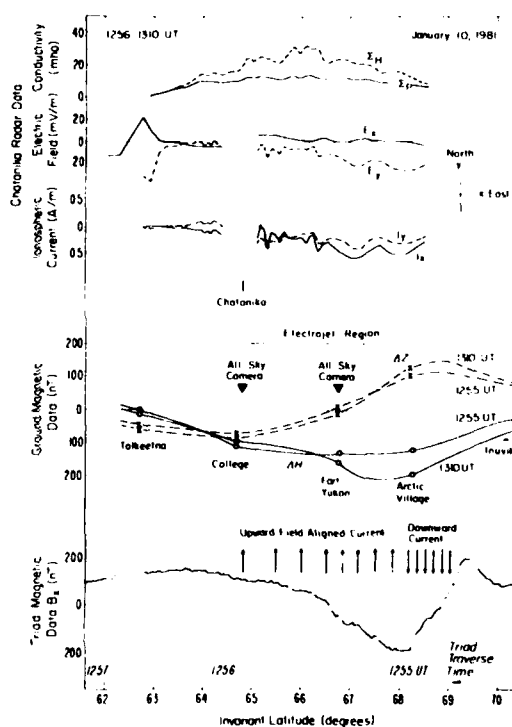


Fig. 2. Latitudinal comparison of Chatanika radar, ground magnetic perturbation, and TRIAD magnetic data for January 10, 1981.

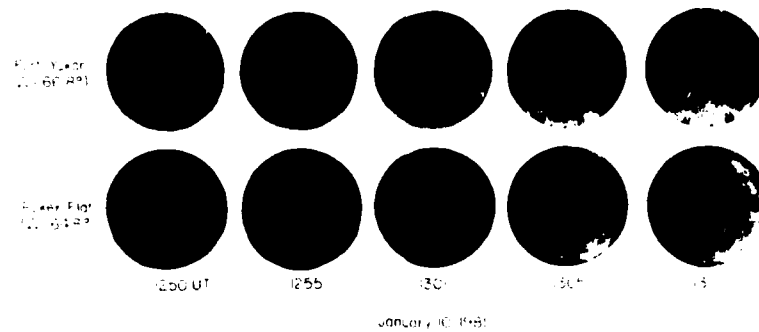


Fig. 3. All-sky camera photograph data from Fort Yukon and Poker Flat for January 10, 1981. Geomagnetic north and east are directed to the right side and downward, respectively, on the photographs.

( $\Delta Z_{\max} - \Delta Z_{\min}$ ) 2 latitude. However, in our particular case, shown in Figure 2, the new center would be located only 0.3 north of the  $\Delta Z = 0$  point. Third, in the TRIAD magnetic perturbation one can notice a distinct change in the slope of  $B_x$  near  $68^\circ$ , indicating that the field-aligned currents change the direction from downward (to the north) to upward (to the south). From the  $B_x$  slope a rough estimate of the current density can be made, yielding  $2.2 \mu\text{A m}^{-2}$  for the downward current and  $0.7 \mu\text{A m}^{-2}$  for the upward current. The "total" currents integrated along the latitude for the upward and downward currents, separately, are found to be almost equal, both giving  $0.28 \text{ A m}$ . This agrees with the statistical result of Iijima and Potemra [1978; see their Figure 14].

A very interesting point is that the region 1 region 2 interface is located well within the poleward half of the electrojet. That is to say, the electrojet center is embedded in the region

of the upward field-aligned current. This is somewhat different from the finding of Senior *et al.* [1982], who suggested that the electrojet center is close to the boundary of the upward and downward field-aligned currents. Note that Senior *et al.* determined the latitude of the center of the auroral electrojet to be  $68^\circ$ , since they used only the  $H$  component records. Another point of interest is that detailed latitudinal variations of the Hall conductivity and the upward field-aligned currents are not well correlated in the equatorward half of the westward electrojet. The most intense upward current between  $66.5^\circ$  and  $68.0^\circ$  is seen in the latitudinal area where  $\Sigma_H$  is decreasing toward higher latitudes, although there is still uncertainty about temporal changes in the latitudinal structure during the interval of the radar scan. This result may suggest that the characteristic energy of precipitating electrons creating a high conductive channel differs from that of current-carrying electrons.

It is of interest to see the distribution of visible auroras corresponding to such a rather complicated current configuration. All-sky camera records from Fort Yukon and Poker Flat for a 20-min period (every 5 min) are shown in Figure 3. The records are not in their best quality because of diffuse overcast conditions at both places, but it is still possible to locate the auroral luminosity along the radar scan. An identical auroral display can be seen in the southern-half sky (to the left in the all-sky camera data) of Fort Yukon and in the northern sky (to the right) from Poker Flat. The equatorward termination of the bright aurora appears to occur overhead at Poker Flat, while the poleward edge of the luminosity moved poleward from  $66.5^\circ$  at 1255 UT to  $67.0^\circ$  at 1310 UT, assuming the auroral altitude to be 110 km. This latitudinal regime coincides with the region of a high Hall conductivity ( $>15\text{--}20 \text{ mhos}$ );  $\Sigma_p$  is almost uniform in a broader regime, from  $\sim 64^\circ$  to  $68^\circ$ . Senior *et al.* [1982] have shown electron density contour plots in an "altitude-latitude" scheme deduced from the radar observations; see their Figure 8. It appears that the latitudinal regime of the electron density enhancements of  $>3 \times 10^5 \text{ el cm}^{-3}$  coincides with that of the bright auroras. In other words, a significant ionization and the corresponding visible auroras are located only in the equatorward half of the westward electrojet.

Figure 4 shows another example of the simultaneous comparison for the January 22, 1981, case in which similar characteristics are well repeated, although the intensity of the westward electrojet is rather weak in this particular case. The TRIAD and Chatanika radar measurements were made during the recovery stage of a weak substorm. The ground magnetometer data indicate no major change occurring in the

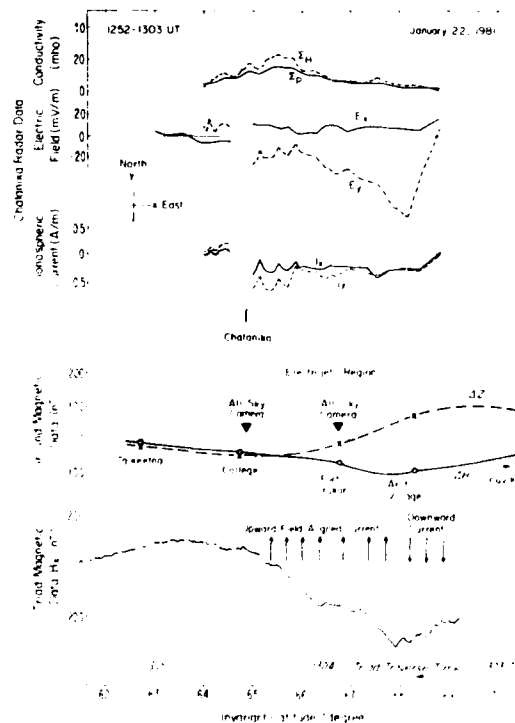


Fig. 4. Same as Figure 2, except for date January 22, 1981.

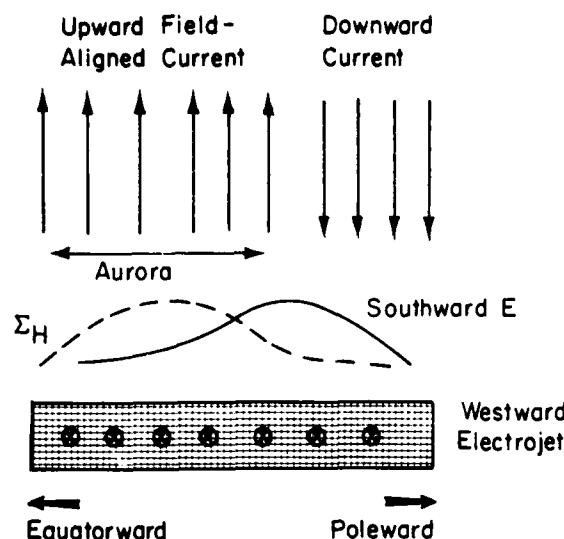


Fig. 5. Schematic illustration of the westward electrojet in the early morning sector. The poleward half of the electrojet is dominated by the southward electric field, whereas its equatorward half is dominated by the Hall conductivity. The field-aligned current reversal occurs at the peak of the electric field.

13-min interval (1252–1305 UT), so that the electrojet extent can be determined relatively accurately. The conductivity is dominant in the equatorward half of the electrojet, while the poleward half is characterized by a large southward electric field reaching 80 mV m. In spite of such a dramatic change in latitudinal profiles of the electric field and conductivity, the westward electrojet current is almost uniform from 64.5 to 68.7. This result is consistent with what one can infer from the latitudinal profile of ground magnetic perturbations. It is clearly seen that the electrojet center (67 to about 67.5) is located well within the upward field-aligned current region. This is, again, in disagreement with the results obtained by Senior *et al.* [1982] who identified the center, by using  $\Delta H$  alone, to be at  $>68.5$  in the region of the downward field-aligned current. However,  $\Delta Z$  was, in fact, very large at Arctic Village, signaling that the electrojet center should be well equatorward of this station (68.3). An inspection of all-sky camera data indicates that the poleward boundary of auroral luminosity remained at about 35 km south of Fort Yukon for the interval of the radar/satellite simultaneous measurement, in agreement with the location of a sharp gradient in  $\Sigma_H$  and  $E_z$ .

We have found similar characteristics in other data sets from TRIAD and Chatanika radar for January 23, 1981, and August 24, 1978, for which only IMS magnetometer data were available; unfortunately, all-sky camera data were not available for the two dates.

#### 4. DISCUSSION

By combining the measurements of ionospheric parameters made by the Chatanika radar and the IMS Alaska meridian magnetometer chain together with TRIAD magnetic data and all-sky photographs, the relative location of the early morning electrojet with respect to field-aligned currents and auroral luminosity has been determined. It has been found that the poleward portion of the westward electrojet in early morning hours has a strong southward electric field, while its equator-

ward portion has a relatively high Hall conductivity. This is in general agreement with the results of Kamide and Vickrey [1983] and Ziesolleck *et al.* [1983], who used radar and rocket observations, respectively. Our present analysis has provided further results for the distribution of visible auroras, which have been found to exist only in the equatorward half of the westward electrojet. The appearance of the auroras only in the equatorward half is consistent with the results of Sulzba-cher *et al.* [1980], who estimated the latitudinal profile of the ratio  $\Sigma_H/\Sigma_p$ , an indication of energetic particle precipitation, from magnetic data of the polar-orbiting satellite TRIAD and the Scandinavia magnetometer array; see their Figure 6. Senior *et al.* [1982] have shown that significant enhancements in the electron density profile occur only within the region of the upward field-aligned current.

In this connection it is of great interest to address the question as to whether or not the commonly adopted auroral oval includes the poleward half of the westward electrojet, where we do not necessarily invoke intense auroral forms. Note that the definition of the auroral oval was originally made in terms of probability of seeing auroral activity [see, for example, Feldstein and Starkov, 1967]. An important point here is that in the poleward half, an intense downward field-aligned current flows. This is the region where Klumpar *et al.* [1976] observed up-going, low-energy electrons escaping from the ionosphere, carrying a sizeable density of the downward field-aligned current. Although it has been a common practice to assume that the auroral oval and the auroral electrojets are colocated (this is why the terminology the "auroral" electrojets has been used), our study demonstrates clearly that this is not the case in the early morning sector. To summarize our observations, we show in Figure 5 a plausible configuration of the westward electrojet in the early morning sector.

Senior *et al.* [1982] have indicated that the region 1 downward and region 2 upward field-aligned currents divide the early-morning westward electrojet into two latitudinal regions. The equatorward half, where the upward field current is flowing, is shown to be dominated by a high conductivity, and the poleward half is associated with the downward current. While the westward electrojet can be divided into two such latitudinal regions, the present study suggests that the two regions do not coincide with the upward and downward field-aligned current regions, respectively. There is an intermediate region in which the conductivity is not completely dominant, but the upward field-aligned current is intense. Indeed, this is the region where the westward electrojet is centered. Our rather complicated profile is consistent, at least qualitatively, with the most recent results of Zanetti *et al.* [1983], who have used three-component magnetometer data from MAGSAT. The altitude of this polar-orbiting satellite is relatively low, so that the magnetometer data include the effects caused by both field-aligned currents and ionospheric currents. It has been indicated by Zanetti *et al.* that the region 1 region 2 interface does not necessarily coincide with the peak location of the westward electrojet in the morning sector. In other words, the region of the electrojet maxima do not occur in the region where either the Hall conductivity or the southward electric field maximizes. The maximum region of the electrojet is actually located somewhere in between. The maximum electric field appears to coincide with the reversal of the upward-downward field-aligned currents. Indeed, Senior *et al.* have noted that the southward electric field is quite large at (and poleward of) this interface. It should be noted further that,

although the schematic diagram in Figure 5 shows only large-scale latitudinal profile of ionospheric parameters, often there exist small-scale ( $\leq 100$  km) current systems associated with auroral arcs having a large  $\Sigma_H/\Sigma_P$  ratio. Sulzbacher *et al.* [1980] have shown that such small-scale systems have essentially the same current configuration as the large-scale system and are located in the region of upward field-aligned currents.

In the cases examined in this paper, the Pedersen conductivity was more or less uniform across the electrojet breadth, meaning that the electric field profile in Figure 5 represents the Pedersen current profile as well. Thus it is most likely, as indicated by Senior *et al.* [1982], that significant portions of the downward and upward field-aligned currents are closed by the southward Pedersen current. Note, however, that this current closure in the early morning sector is different to some extent from the closure in the late-morning sector, where the intensities of the region 1 and region 2 currents, integrated over the entire latitude of the westward electrojet, are not of the same order of magnitude any longer [Kamide *et al.*, 1976]. In late morning hours, portions of the intense downward field-aligned current feed the westward electrojet, and other portions tend to flow southward as the Pedersen current. It is an important task to extend this particular latitudinal "slice" with those in other local time sectors.

**Acknowledgment.** The work at NOAA was supported by the National Research Council under the Resident Research Associate Program. The work at SRI International was supported by the Air Force Office of Scientific Research under contract F49620-80-C-0014. Radar operations were supported by the Defense Nuclear Agency under contract DNA001-77-C-0042. The work at University of Alaska was supported in part by a grant from the National Science Foundation, ATM81-15321. The TRIAD work was supported at Applied Physics Laboratory of The Johns Hopkins University by the National Science Foundation and by the Office of Naval Research.

The Editor thanks W. Baumjohann and C. Senior for their assistance in evaluating this paper.

#### REFERENCES

- Akasofu, S.-I., J. Kisabeth, G. J. Romick, H. W. Kroehl, and B.-H. Ahn, Day-to-day and average magnetic variations along the IMS Alaska meridian chain of observations and modeling of a three-dimensional current system, *J. Geophys. Res.*, **85**, 2065, 1980.
- Armstrong, J. C., and A. J. Zmuda, Three-axis magnetic measurements of field-aligned currents in the auroral region, *J. Geophys. Res.*, **78**, 6802, 1973.
- Baumjohann, W., Ionospheric and field-aligned current systems in the auroral zone: A concise review, *Adv. Space Res.*, **2**, 55, 1983.
- de la Beaujardiere, O., R. R. Vondrak, and M. Baron, Radar observations of electric fields and currents associated with auroral arcs, *J. Geophys. Res.*, **82**, 5051, 1977.
- Feldstein, Y. L., and G. V. Strakov, Dynamics of auroral belt and polar geomagnetic disturbances, *Planet. Space Sci.*, **13**, 209, 1967.
- Hughes, T. J., and G. Rostoker, A comprehensive model current system for high-latitude magnetic activity. I. The steady state system, *Geophys. J. R. Astron. Soc.*, **58**, 528, 1979.
- Iijima, T., and T. A. Potemra, Large-scale characteristics of field-aligned currents associated with substorms, *J. Geophys. Res.*, **83**, 599, 1978.
- Kamide, Y., On the empirical relationship between field-aligned currents and auroras, in *Physics of Auroral Arc Formation*, edited by S.-I. Akasofu and I. R. Kan, pp. 192-198, AGU, Washington, D.C., 1981.
- Kamide, Y., and J. E. Vickrey, Relative contribution of ionospheric conductivity and electric field to the auroral electrojets, *J. Geophys. Res.*, **88**, 7989, 1983.
- Kamide, Y., S.-I. Akasofu, and G. Rostoker, Field-aligned currents and the auroral electrojet in the morning sector, *J. Geophys. Res.*, **81**, 6141, 1976.
- Kisabeth, J. L., and G. Rostoker, Modelling of three-dimensional current systems associated with magnetospheric substorms, *Geophys. J. R. Astron. Soc.*, **49**, 655, 1977.
- Klumpar, D. M., J. R. Burrows, and M. D. Wilson, Simultaneous observations of field-aligned currents and particle fluxes in the post-midnight sector, *Geophys. Res. Lett.*, **3**, 395, 1976.
- Robinson, R. M., R. R. Vondrak, and T. A. Potemra, Electrodynamic properties of the evening sector ionosphere within the region 2 field-aligned current sheet, *J. Geophys. Res.*, **87**, 731, 1982.
- Senior, C., R. M. Robinson, and T. A. Potemra, Relationship between field-aligned currents, diffuse auroral precipitation and the westward electrojet in the early morning sector, *J. Geophys. Res.*, **87**, 10,469, 1982.
- Sulzbacher, H., W. Baumjohann, and T. A. Potemra, Coordinated magnetic observations of morning sector auroral zone currents with TRIAD and the Scandinavian magnetometer array, A case study, *J. Geophys. Res.*, **85**, 7, 1980.
- Vondrak, R. R., and M. J. Baron, Radar measurements of the latitudinal variation of auroral ionization, *Radio Sci.*, **11**, 939, 1976.
- Zanetti, L. J., W. Baumjohann, and T. A. Potemra, Ionospheric and Birkeland current distributions inferred from MAGSAT magnetometer data, *J. Geophys. Res.*, **87**, 4875, 1983.
- Ziesolleck, S., W. Baumjohann, K. Bruning, C. W. Carlson, and R. I. Bush, Comparison of height-integrated current densities derived from ground-based magnetometer and rocket-borne observations during the porcupine F3 and F4 flights, *J. Geophys. Res.*, **88**, 8063, 1983.
- S.-I. Akasofu, Geophysical Institute, University of Alaska, Fairbanks, AK 99701.
- Y. Kamide, Kyoto Sangyo University, Kyoto 603, Japan.
- T. A. Potemra, Applied Physics Laboratory, The Johns Hopkins University, Laurel, MD 20707.
- R. M. Robinson, Radio Physics Laboratory, SRI International, Menlo Park, CA 94025.

(Received March 21, 1983;  
revised September 14, 1983;  
accepted September 15, 1983.)

APPENDIX E

AURORAL ZONE CONDUCTIVITIES WITHIN  
THE FIELD-ALIGNED CURRENT SHEETS

by

R. M. Robinson

Radio Physics Laboratory

SRI International

Menlo Park, CA 94025

R. R. Vondrak

Lockheed Palo Alto Research Laboratory

Palo Alto, CA 94304

and

T. A. Potemra

Applied Physics Laboratory

Johns Hopkins University

Laurel, MD 20707

## ABSTRACT

We have used field-aligned current data obtained by the Triad satellite during 21 passes over Alaska to order conductivity measurements made simultaneously by the Chatanika radar. Three distinct field-aligned current sheets were sampled during these experiments: the Region 2 current sheet in the morning and evening sectors and the Region 1 current sheet in the evening sector. We display the height-integrated conductivities (conductances) in various formats to show the characteristics of precipitation in each of the field-aligned current regions. The conductances in the Region 2 evening sector current sheet increase uniformly with latitude and the total increase in conductance across the sheet is fairly constant. The latitudinal profiles of conductance across the Region 1 evening sector current sheet show that auroral arcs tend to occur in the poleward portion of the sheet. In the morning sector Region 2 current sheet the Hall conductance is larger and changes much more rapidly with latitude than the Pedersen conductance. The Hall and Pedersen conductance can be interpreted in terms of the number density and temperature of a Maxwellian distribution of electrons that would produce the same conductance values. We call this electron population the equivalent Maxwellian source. Although the temperatures and densities thus deduced may not be equal to those of the electrons in the plasma sheet, these quantities can still be used to characterize, in a relative sense, the source regions in the magnetosphere to which the field-aligned currents connect. The same concept is used to study the extent to which the precipitating electrons can carry the field-aligned current measured in the various regions. A comparison of conductance with the field-aligned current measured at the same latitude reveals that the two quantities are not correlated. We conclude that only the direction of the field-aligned currents influences the conductance in that upward

currents favor the formation of parallel potential drops and auroral arcs. The electron density and temperature of the source appears to be more important in determining the conductances than the magnitude of the field-aligned currents.

## I INTRODUCTION

Auroral zone conductivities were measured during the ten years of operation of the Chatanika radar in Alaska. In contrast to conductivity measurements inferred from satellite data radar measurements yield the conductivity directly from the ionization profile. Statistical models of auroral zone conductivities have been constructed from satellite data [Wallis and Budzinski, 1981; Spiro et al., 1982] and the results are consistent with conductivities measured by the Chatanika radar and published in various papers [e.g., Brekke et al., 1974; Vickrey et al., 1981]. A similar statistical approach using the Chatanika radar data is difficult because the Chatanika data are limited in latitudinal coverage.

In this paper we take a somewhat different approach. We present conductivity measurements made while the radar was scanning in elevation in the magnetic meridian during coordinated experiments with the Triad satellite. The advantages of using this data set is that the field-aligned current information provided by Triad can be used to order the conductivity measurements. Iijima and Potemra (1976) used Triad data to show that the large scale field-aligned currents can be divided into two regions. Region 1 connects to the poleward portion of the auroral zone and is upward in the afternoon and evening sectors and downward from midnight through the morning hours. The Region 2 current sheets connect to the equatorward portion of the auroral zone and are oppositely directed. There is evidence to suggest that each of these



large-scale field-aligned current sheets connects to different regions in the plasma sheet [Winningham et al., 1975; Sugiura, 1975]. Because the conductivities are produced primarily by precipitating electrons, the height-integrated conductivities in each of the field-aligned current sheets should reflect the differences in the particle populations of the magnetosphere to which the currents connect. However, the ionospheric conductances are also affected by the field-aligned current existing on the same flux tube because current-driven instabilities occurring in regions of upward current lead to the formation of parallel potential drops that accelerate electrons into the atmosphere.

Coordinated experiments between the Triad satellite and the Chatanika radar were scheduled routinely from September 1979 to March 1982 when the radar was dismantled for relocation to Greenland. Case studies of electric fields and conductivities and their relation to field-aligned currents measured by Triad have been discussed by Robinson et al. (1982) and Senior et al. (1982). In this paper we examine conductivities using the entire Chatanika/Triad data base.

## II EXPERIMENTAL TECHNIQUE

During the Triad/Chatanika experiments the radar scanned in elevation in the magnetic meridian. Each scan took 12 to 15 minutes to complete and spanned about  $140^\circ$  in elevation angle. Electron density and line-of-sight velocity data obtained during a scan were used to determine conductivity and electric field as a function of both latitude and altitude. The magnetometers on the Triad satellite can measure magnetic perturbations with a temporal resolution of .5 s or about 4 km in the ionosphere. Because the Triad satellite pass did not always occur near the Chatanika meridian the satellite and radar data were expressed as a function of invariant latitude for comparison. In

this study we have used only data from satellite passes that contain some evidence that auroral forms were extended in the east-west direction. Decisions to include a particular pass in the study were made on the basis of (1) all sky camera photographs when available, (2) the north-south magnetic perturbation in the Triad data, and (3) the similarity between the appearance of the ionosphere as determined from radar elevation scans before and after the time of the pass. Triad passes during which the satellite crossed the longitude of Chatanika more than 400 km from the radar's meridian were not used in the study.

Temporal ambiguities were removed from the data set by only using the radar scan that was simultaneous with the Triad pass. Scans before and after the satellite pass were examined to ensure the steadiness of the ionosphere during the experiment. Passes that occurred during substorm conditions were not used in the study.

Field-aligned currents for each pass were determined from Triad magnetic field measurements expressed in geomagnetic coordinates. Processing and filtering of the Triad data are described by Saflekos et al. (1978). In most cases, the field-aligned current sheets in Regions 1 and 2 were well defined in the Triad data. In several instances, however, the Triad data could not be interpreted in terms of the statistical pattern mapped out by Iijima and Potemra (1976), although no indication of disturbed conditions was apparent in the radar data. Data from these passes were not used in the study.

The field-aligned current derived from the Triad data for each pass was used to determine the equatorward and poleward boundary of each current sheet. These parameters were used to express the conductivities as a function of fractional distance across the current sheet. Baseline problems often made it difficult to identify the boundaries of the field-aligned currents in the

Triad data. This is especially true at the equatorward edge of the Region 2 current sheet. However, in most cases this boundary could be localized to a latitudinal region that was small compared to the total width of the sheet.

Height-integrated conductivities were computed by combining radar measurements of electron density with neutral atmosphere parameters given by the 1000° thermopause model of Banks and Kockarts (1973). The ion neutral collision frequency used was  $3.75 \times 10^{-10} [N] \text{ s}^{-1}$  where  $[N]$  is the neutral number density in  $\text{cm}^{-3}$ . Because the limits of the radar scan were 15° and 25° elevation to the north and south, respectively, only about a 500 km wide section of the E region ionosphere was sampled during a scan. In this paper, all conductivities were integrated over altitude from 80 km to 160 km. In accordance with Spiro et al. (1982), we use the term conductance to mean height-integrated conductivities.

Table 1 gives the date and local time of the passes used in this study. Most of the passes occurred in winter months. Even for those passes near equinox, the solar contribution to E region conductance was negligible. The solar zenith angle at the times of the passes was never less than 90°. Thus, precipitating particles primarily produced the E region density measured by the radar.

Three distinct field-aligned current regions are represented in the data set: Region 2 evening sector, Region 1 evening sector, and Region 2 morning sector. No radar data were obtained within the Region 1 current sheet in the morning sector. The conductances in each of these three regions will be examined in three ways. We begin by showing the latitudinal variation of the conductances. We then discuss the precipitating electron characteristics in each of the regions by introducing the concept of an equivalent Maxwellian source. The equivalent Maxwellian source is the electron population at high altitudes

above the ionosphere that would produce the same combination of height-integrated Hall and Pedersen conductivities. Using the same concept, we discuss the extent to which the precipitating electrons can carry the field-aligned current measured by Triad in the three regions.

#### Equivalent Maxwellian Source

In this section we compute the ionospheric conductances produced by precipitation from a Maxwellian population of electrons at high altitudes along a magnetic flux tube. A Maxwellian velocity distribution is given by

$$F(v) = n \left( \frac{m}{2\pi kT} \right)^{3/2} e^{-mv^2/2kT} \quad (1)$$

where  $n$  is the density,  $T$  is the temperature,  $k$  is Boltzmann's constant,  $v$  is the electron velocity and  $m$  is the electron mass. The differential energy spectrum of the electrons is given by

$$F(E) = \frac{2E}{m} n \left( \frac{m}{2\pi kT} \right)^{3/2} e^{-E/kT} \quad (2)$$

where  $E$  is the electron energy. If the pitch angle distribution at high altitudes above the ionosphere is isotropic, (i.e., strong pitch angle diffusion) the energy spectrum of electrons precipitating into the ionosphere will be given by Eq. (2). The height-integrated conductivity produced by precipitating electrons with this energy spectrum can be found by first using an energy deposition code [e.g., Rees, (1963)] to compute the resulting ionization in the altitude range where the perpendicular conductivities are significant (70 km to 200 km). Height-integrated conductivities are then calculated by the classical formulae. In reality, the lower energy portion of the electron

spectrum deviates from a Maxwellian due to the production of secondary electrons. However, precipitating electrons with energies less than 1 Kev will deposit little energy below about 160 km. Thus, the conductances are determined primarily by the part of the spectrum that is nearly Maxwellian in shape.

Using the technique described above, we computed the Hall and Pedersen conductances resulting from precipitating electrons with Maxwellian source distributions given by Eq. (1) with densities of .1, .2, 1, and 2  $\text{cm}^{-3}$ . The results are shown in Figure 1. Note that the ratio of Hall to Pedersen conductance depends only on  $kT$  while either the Hall or Pedersen conductance alone depends on both source density and temperature. A given combination of Hall and Pedersen conductance corresponds to a unique set of values for  $n$  and  $kT$ . The values of  $n$  and  $kT$  thus derived characterize the electrons that produce the conductivity.

The net current carried by electrons with an energy distribution given by Eq. (2) is given by

$$j_z \left( \text{A/m}^2 \right) = 8.5 \times 10^{-7} n(kT)^{1/2} \quad (3)$$

where  $n$  is in  $\text{cm}^{-3}$  and  $kT$  is in Kev. Figure 2 shows the conductances that are produced when electrons from a Maxwellian source carry currents along the field line of 0.5, 1.0, 2.0, and 4.0  $\mu\text{A/m}^2$ .

The results in Figures 1 and 2 are true only for a Maxwellian source and in the case of strong pitch angle diffusion. Several investigators have attempted to make coordinated measurements of electron fluxes at conjugate points in the ionosphere and in the equatorial plane of the magnetosphere [Meng et al., 1979; Hones et al., 1971]. These results are not conclusive and the extent of isotropy in plasma sheet velocity distributions is not known.

This suggests that although the source density and temperature of the electron source giving rise to the observed conductances may not be determined in an absolute sense, the relative changes that we observe are significant. We subsequently refer to the electron population defined by the auroral conductances as the equivalent Maxwellian source. The density and temperature of the equivalent Maxwellian source are often good parameters to use in describing conductances observed in auroral forms. Similarly the conductances observed in the ionosphere provide a direct indication of the characteristics of the source electrons.

### III RESULTS

#### Latitudinal Variations of Conductances

In Figures 3, 4, and 5, we display the latitudinal variations of the conductances in each of the three field-aligned current regions. The abscissa in these figures is the fractional distance across the current sheet. Figure 3 shows the results for the Region 2 evening sector current sheet for 13 Triad satellite passes. Note that the conductances increase linearly across the current sheet and that the total change in conductance across the current sheet is very similar for all the passes regardless of the actual width of the current sheet. This is especially true for the Pedersen conductance. The Hall conductance is enhanced in some cases in the poleward portion of the current sheet. The ratio of Hall conductance to Pedersen conductance in this field-aligned current region is typically between 1.0 and 1.4.

Figures 4(a) and 4(b) show the latitudinal variation in Pedersen and Hall conductances, respectively, across the Region 1 current sheet for seven evening sector Triad passes. Auroral arcs are apparent in all of these traces as latitudinally confined conductivity enhancements with relatively sharp gradi-

ents at the edges. In six out of seven cases these enhancements were confined to the poleward half of the current sheets. The one exception corresponds to the most intense and widest of all the arcs observed. The width of the arc for this case was about 100 km or half the width of the current sheet. With the exception of this pass, the data shown in Figure 4 indicate that the conductance in the equatorward half of Region 1 is very similar to that of the poleward edge of Region 2. In fact, the conductance decreases slightly with latitude in this portion of the Region 1 current sheet. Although this data set is limited, we note that an arc-like electron density enhancement was present in the data whenever there was a well-defined Region 1 current sheet in the field of view of the radar.

Figures 5(a) and 5(b) show the latitudinal variation in Pedersen and Hall conductance, respectively, across the Region 2 current sheet for five morning sector passes. The Pedersen conductance is typically between 8 and 16 mhos and does not vary a great deal with latitude. The Hall conductance, on the other hand, exhibits large random variations with latitude. The ratio of Hall to Pedersen conductance in the morning sector varies between 1.0 and 2.4 and is larger than that in the evening sector.

#### Precipitating Particle Characteristics

Figures 6, 7, and 8 are scatterplots of the Hall and Pedersen ratio as a function of the Hall conductance for each of the three field-aligned current regions. The curves from Figure 1 have been superimposed for reference. These results show that the differences in conductances in the three field-aligned currents regions can be interpreted in terms of variations of the density and temperature of the source regions. In the Region 2 evening sector current sheet, the densities implied by the conductances are  $.04$  to  $1 \text{ cm}^{-3}$  and

the characteristic energies are less than about 2 Kev. In much of the Region 1 evening sector current sheet, the conductances are similar to these values. However, auroral arcs occur within this upward current sheet and the arcs seem to originate from electrons of about the same temperature but with higher densities. As discussed below, the densities associated with arcs must be interpreted somewhat differently owing to the presence of parallel potential drops between the ionosphere and the source. In the morning sector current sheet, the source densities are between  $0.5$  and  $2.0 \text{ cm}^{-3}$  and the temperatures are between 1 and 4 Kev.

To aid in the interpretation of the data plotted in Figures 6, 7, and 8, we show in Figure 9 two electron density contour plots constructed from radar elevation scans made during Triad satellite passes. The contours in the figure are drawn in a magnetic coordinate system so that field lines are vertical. The arrows in the figures indicate the direction of the field-aligned currents as determined from the simultaneous Triad magnetometer data. For the scan in Figure 9(a) both the Region 1 and Region 2 evening sector current sheets were within the radar field of view. In Figure 9(b), we show the location of the Region 2 morning sector current sheet. Figures 10(a) and 10(b) are scatterplots of conductances measured during the scans shown in Figure 9(a) and 9(b), respectively. In Figures 10(a) and 10(b), we have used x's to indicate conductances measured in upward current regions and dots to indicate conductances measured in downward current regions. As in Figures 6 and 8, the conductances measured in each of the three regions are distributed in different portions of the  $\Sigma_H/\Sigma_p$  versus  $\Sigma_H$  plane.

These differences are further emphasized by the differential energy spectra shown in Figure 11. The dashed lines show electron energy spectra reconstructed using the UNTANGLE code [Vondrak and Baron, 1977] from the ionization



profiles labeled A, B, and C in Figure 9. Profile A is indicative of the ionization produced by precipitation from the inner edge of the plasma sheet. Profile B is typical of central plasma sheet precipitation which is thought to be responsible for the diffuse aurora. The solid curves represent the equivalent Maxwellian source spectra. The temperature and density of the Maxwellian is given in the figure. Although the temperatures of the Maxwellians in Figures 11(a) and 11(b) do not differ substantially, the densities differ by a factor of six. Thus, the gradient in conductivity across the Region 2 current sheet is produced primarily by a corresponding change in plasma sheet density. We may also conclude from Figures 11(a) and 11(b) that for energies below about 10 Kev the equivalent Maxwellian source spectrum is a good approximation to the real spectrum.

#### Parallel Current

Figures 12 and 13 are plots of conductance as a function of field-aligned current density. Figure 12 includes data from all flux tubes within the Region 2 field-aligned current sheet. In the evening sector, Region 2 is downward (negative), while in the morning sector Region 2 is upward (positive). Therefore, in Figure 12 most of the data to the right of the zero line was obtained from morning sector Triad passes. Figures 12(a) and 12(b) show that the conductances in Region 2 are slightly higher in the morning sector than in the evening sector. This tendency is more pronounced for the Hall conductance. Thus, this evening-morning asymmetry is most obvious in the Hall to Pedersen ratio plotted in Figure 12(c).

Figure 13 displays the results for the evening sector Region 1 current sheet. Recall that no data were obtained for Region 1 in the morning sector. However, there are two data points where downward current was observed within

the Region 1 evening sector current sheet. It is clear from Figure 13 that there is a wide range of conductance associated with any given field-aligned current value. For example, the Pedersen conductance associated with a Region 1 current of  $2.5 \mu\text{A}/\text{m}^2$  can be as little as 5 mhos or as large as 40 mhos. The maximum values for the conductances are substantially higher than in the Region 2 current sheet. However, the Hall to Pedersen ratio is not significantly different from that measured in the morning sector Region 2 current sheet.

#### IV DISCUSSION

We have displayed conductances in the auroral zone in several different formats. Using simultaneous measurements of field-aligned currents by the Triad satellite, we ordered the data according to the current region within which the data were obtained. The properties of the conductances in each of the three field-aligned current regions sampled are reviewed and discussed below.

##### Region 2 Evening Sector

Perhaps the most striking aspect of conductances in the Region 2 evening sector current sheet is the linear change with latitude displayed in Figure 3. Several studies have indicated close spatial coincidence between this current sheet and the diffuse aurora [Robinson et al., 1982; Tsunoda et al., 1976]. The latitudinal distribution of precipitation in the diffuse aurora has been studied by Whalen (1974) using ionosphere sounder data. He found that the energy flux and average energy of the diffuse aurora have Gaussian latitudinal profiles. Fonteyn and Blanc (1983) inferred a similar distribution on theoretical grounds. The latitudinal distribution is determined by the combined

effects of magnetospheric convection and pitch angle diffusion. The decrease in precipitating electron flux with decreasing latitude is caused by depletion of the electron population as a result of strong pitch angle diffusion. This decrease in source density is exemplified by the results shown in Figures 11(a) and 11(b). In this example, the source density across the Region 2 current sheet changed by about a factor of six.

The parallel current contribution from precipitating electrons in the Region 2 evening sector current sheet is shown in Figure 12. The current carried by precipitating electrons is directed upward while the total current is downward. Thus, the electrons responsible for the conductance in this current sheet oppose the net field-aligned current.

#### Region 1 Evening Sector

The equatorward portion of the Region 1 evening sector current sheet has conductances similar to those found at the poleward edge of the Region 2 current sheet. Robinson et al. (1982) have shown that the boundary between the Region 2 and Region 1 current sheets in the evening sector usually occurs near a latitudinally localized enhancement in E region density referred to as the interface arc. In terms of the diffuse aurora model of Fonteyn and Blanc (1983) this localized maximum is the result of strong pitch angle diffusion on nondepleted flux tubes. That is, the competing effects of convection and precipitation produce a localized region of enhanced flux. Auroral arcs occur poleward of this interface arc. As shown in Figure 9 arcs appear to originate from Maxwellian sources with higher densities than the diffuse aurora. However, interpretation of the meaning of the equivalent Maxwellian source spectrum is ambiguous within auroral arcs. Evans (1974) has discussed the energy spectra of precipitating electrons that are likely to result from acceleration

of a Maxwellian source through a parallel potential drop  $V_0$ . For energies greater than  $V_0$

$$F(E) = \frac{2E}{m} n \left( \frac{m}{2\pi kT} \right)^{3/2} \exp \left[ -(E - eV_0)/kT \right] \quad (4)$$

where  $e$  is the electron charge. For energies less than  $V_0$  the spectrum is comprised of backscattered and secondary electrons and electrons that have been reflected (perhaps several times) from the bottom of the potential barrier [Pulliam et al., 1981]. Considering this, it is at first somewhat surprising that the conductances in auroral arcs tend to be distributed along a constant density contour. However, as noted above, electrons with energy less than 1 Kev do not contribute to the conductances. When  $V_0$  is less than 1 Kev the spectrum above 1 Kev is Maxwellian with the fluxes at each energy larger than those of the unaccelerated Maxwellian by a factor  $eV_0/kT$ . In this case, the density of the equivalent Maxwellian source is higher than the density of the unaccelerated electrons by the same factor. For all the conductances in an auroral arc to lie along a constant density contour as in Figure 10(a) requires that the factor  $eV_0/kT$  be constant everywhere in the arc. Because arcs have been associated with inverted V events  $V_0$  must vary across the arc. However, Hoffman and Lin (1981) examined the quantities  $kT$  and  $V_0$  for many inverted V events and found that the ratio  $eV_0/kT$  tends to remain constant within each event. That is, the potential drop increases with the source temperature. Thus, the resulting conductances appear to be produced by a source whose density does not vary across the arc.

For  $V_0$  greater than 1 Kev the portion of the primary spectrum below  $eV_0$  is not Maxwellian. However, the difference may not be significant since the filling in of the spectrum by secondaries may produce fluxes very similar to

that expected from a pure Maxwellian [Pulliam et al., 1981]. In particular, if  $V_0$  is not too large (1-5 Kev), only the Pedersen conductance will be affected by the non-Maxwellian part of the spectrum because the Hall mobility peaks at altitudes that are not affected by lower energy electrons. Thus, the precipitation in most auroral arcs can be attributed to a Maxwellian source with a density of  $neV_0/kT$  where  $n$  is the actual source density.

In examining conductivity data from evening sector auroral arcs, we have found a great deal of variability from one arc to the next in the density of the equivalent Maxwellian source. This variability may reflect differences in the quantity  $eV_0/kT$  rather than in the density. If the source density in the arc is assumed to be the same as that outside the arc, the quantity  $eV_0/kT$  can be determined from the density of the equivalent Maxwellian source.

We can use the equivalent Maxwellian source concept to examine the extent to which precipitating electrons can carry the upward current observed in the Region 1 evening sector current sheet. Comparing Figure 13 with Figure 2 shows that the observed conductances are not consistent with the field-aligned current measured along the same field line. Thus, lower energy electrons must also contribute to the current in the Region 1 evening sector current sheet.

#### Region 2 Morning Sector

The latitudinal profile of conductance in the Region 2 morning sector current sheet differs from that in the evening sector diffuse aurora in two respects. First, the peak in the precipitating electron flux occurs near the center of the current sheet rather than between the two sheets. Second, there are large variations in the Hall to Pedersen ratio with the ratio being larger on the average than those in the evening sector. This asymmetry may be due to differences in the source populations, or may be due to the effects of field-

aligned currents on pitch angle diffusion. The wider range in source temperature in the Region 2 morning sector population results in the spreading out along a constant density contour of the points in Figure 8. Thus, the source density in the morning sector is clearly defined and lies between .6 and  $2 \text{ cm}^{-3}$ .

In contrast to the results found for the upward current sheet in the evening sector, the conductances and field-aligned currents observed in the morning sector are more consistent with that expected from a Maxwellian electron source. This can be seen by comparing Figure 12 with Figure 2. For example, a field line carrying a parallel current of  $1.5 \text{ } \mu\text{A/m}^2$  on which a Hall conductance between 5 and 30 mhos is measured, must have a Hall to Pedersen ratio between 1.0 and 2.2 if produced by a Maxwellian source. This is close to the measured values shown in the bottom panel of Figure 12.

#### Magnetic Storm Related Conductivities

The data that comprise Figures 3 to 12 necessarily represent only magnetically quiet to moderate periods, because in more active times the field-aligned current sheets become difficult to identify. However, even in active periods, an equivalent Maxwellian source can be identified. The temperature and density of the source is fairly distinctive and changes dramatically in space and time. An example is shown in Figures 14 and 15. Figure 14 shows two electron density contour plots from elevation scans approximately 2 hours apart. The first occurred during the onset of a 500 nT negative bay at College, while the second occurred later in the recovery period. The scatterplots in Figure 15 show that the conductances in the first scan are consistent with precipitation from a source of density between 1 and  $5 \text{ cm}^{-3}$  and temperature between 1 and 8 Kev. The conductances in the second scan indicate a

source density between .2 and  $1 \text{ cm}^{-3}$  and a temperature between 3 and 6 Kev. Note that because of the wide range in conductances observed in each of these scans the value of the source density is quite obvious.

## V SUMMARY AND CONCLUSIONS

By combining Triad satellite measurements of field-aligned currents with simultaneously obtained Chatanika measurements of height-integrated conductivity, we have been able to characterize conductances in each of three field-aligned current regions.

The latitudinal profiles of conductance are distinct in each of the field-aligned current sheets. In Region 2 of the evening sector, the conductance increases uniformly with latitude with the total change across the current sheet very similar in all cases. In Region 1 of the evening sector, auroral arcs are usually confined to the poleward portion of the current sheet. In Region 2 of the morning sector, the Hall conductance is larger than the Pedersen conductance and changes much more rapidly with latitude. Except for the presence of auroral arcs, the conductances in the evening sector are consistent with those predicted by models of particle precipitation by strong pitch-angle diffusion.

We interpreted the conductances in terms of the number density and temperature of a Maxwellian source of electrons that would produce the same conductance values. The evening sector diffuse aurora seems to originate from a population with temperature less than about 2 Kev and density less than  $1 \text{ cm}^{-3}$ . The morning sector diffuse aurora within the Region 2 current sheet originates from a population with temperatures between 1 and 4 Kev and density between .6 and  $2 \text{ cm}^{-3}$ . The source density and temperature in the

Region 1 current sheet in the evening sector is similar to that of Region 2 in the evening sector except within auroral arcs. Arcs appear to originate from a population within density greater than  $1.0 \text{ cm}^{-3}$ . However, this is probably because the fluxes at each energy are higher by a factor  $eV_0/kT$  owing to acceleration through parallel potential drops.

We also compared the conductances with the field-aligned currents measured at the same latitude by the Triad satellite. There is little correlation between the field-aligned current density and the conductance measured along the same flux tube. Thus, our results do not suggest a relation between field-aligned current density and conductances, either their absolute values or their ratio. Only the direction of the field-aligned currents influences the conductance in that upward currents favor the formation of parallel potential drops and auroral arcs. The electron density and temperature of the source population appears to be more important in determining the ionospheric conductances than the magnitude of the field-aligned currents.

The concept of equivalent Maxwellian source was used to study the extent to which the electrons producing the conductance can carry the observed field-aligned currents. Only in the morning sector Region 2 current sheet can the energetic electrons carry a large fraction of the upward current.

Finally, we note that our data are more heavily weighted toward local times near midnight. The conductances within field-aligned current sheets at dawn and dusk may differ from those shown here. This difference may arise because of a local time variation in the properties of the source plasma or the spatial relationship of the field-aligned currents relative to this source. For example, the Region 2 current sheet in the evening sector may extend well equatorward of the central plasma sheet electron precipitation [Klumpar, 1979]. In addition, precipitating protons within this current sheet



may produce conductances differing from those shown here. Similar effects may be present in the morning sector and in the dayside auroral zone.

#### REFERENCES

- Banks, P. M. and G. Kockarts, Aeronomy, Academic Press, New York, New York, (1973).
- Brekke, A., J. R. Doupnik, and P. M. Banks, "Incoherent Scatter Measurements of E-region Conductivities and Currents in the Auroral Zone," J. Geophys. Res., Vol. 79, 25, 3773, (1974).
- Evans, D. S., "Precipitating Electron Fluxes Formed by a Magnetic Field-Aligned Potential Difference," J. Geophys. Res., 79, 2853, (1974).
- Fontaine, D. and M. Blanc, "A Theoretical Approach to the Morphology and the Dynamics of the Diffuse Auroral Zones," J. Geophys. Res., Vol. 188, 7171, (1983).
- Hoffman, R. A., and C. S. Lin, Study of Inverted-V Auroral Precipitation Events in Physics of Auroral Arc Formation, S. I. Akasofu and J. R. Kan, editors, Geophysical Monograph 25, American Geophysical Union, Washington, DC, (1981).
- Hones, E. W., Jr., J. R. Asbridge, S. J. Bame, and S. Singer, "Energy Spectra and Angular Distributions of Particles in the Plasma Sheet and Their Comparison with Rocket Measurements Over the Auroral Zone," J. Geophys. Res., 76, 63, (1971).
- Iijima, T. and T. A. Potemra, "The Amplitude Distribution of Field-Aligned Currents at Northern High Latitudes Observed by Triad," J. Geophys. Res., 84, 2165, (1976).

- Klumpar, D., "Relationships Between Auroral Particle Distributions Associated with Field-Aligned Currents," J. Geophys. Res., 84, 6524, (1979).
- Meng, C.-I., B. Mauk, and C. E. McIlwain, "Electron Precipitation of Evening Diffuse Aurora and its Conjugate Electron Fluxes Near the Magnetospheric Equator," J. Geophys. Res., 84, 2545, (1979).
- Pulliam, D. M., H. R. Anderson, K. Stamnes, and M. H. Rees, "Auroral Electron Acceleration and Atmospheric Interactions: (1) Rocket-Borne Observations and (2) Scattering Calculations," J. Geophys. Res., 86, 2397, (1981).
- Rees, M. H., "Auroral Ionization and Excitation by Incident Energetic Electrons," Planet Space Sci., 11, 1209, (1963).
- Robinson, R. M., R. R. Vondrak, and T. A. Potemra, "Electrodynamic Properties of the Evening Sector Ionosphere Within the Region 2 Field-Aligned Current Sheet," J. Geophys. Res., 83, 1493, (1978).
- Saflekos, N. A., T. A. Potemra, and T. Iijima, "Small-Scale Transverse Magnetic Disturbances in the Polar Regions Observed by Triad," J. Geophys. Res., 83, 1493, (1978).
- Senior, C., R. M. Robinson, and T. A. Potemra, "Relationship Between Field-Aligned Currents, Diffuse Auroral Precipitation and the Westward Electrojet in the Early Morning Sector," J. Geophys. Res., 87, 10469, (1982).
- Spiro, R. W., P. H. Reiff, and L. J. Maher, Jr., "Precipitating Electron Energy Flux and Auroral Zone Conductances--An Empirical Model," J. Geophys. Res., 87, 8215, (1982).
- Sugiura, M., "Identifications of the Polar Cap Boundary and the Auroral Belt in the High Altitude Magnetospheres: A Model for Field-Aligned Currents," J. Geophys. Res., 80, 2057, (1975).

- Tsunoda, R. T., R. I. Presnell, and T. A. Potemra, "The Spatial Relationship Between the Evening Radar Aurora and Field-Aligned Currents," J. Geophys. Res., 81, 3791, (1976).
- Vickrey, J. F., R. R. Vondrak, and S. J. Matthews, "The Diurnal and Latitudinal Variation of Auroral Zone Ionospheric Conductivity," J. Geophys. Res., 86, 65, (1981).
- Wallis, D. C. and E. E. Budzinski, "Empirical Models of Height Integrated Conductivities," J. Geophys. Res., 86, 125, (1981).
- Whalen, J. A., "A Quantative Description of the Spatial Distribution and Dynamics of the Energy Flux in the Continuous Aurora," J. Geophys. Res., 88, 7155, (1983).
- Winningham, J. D. F. Yasuhara, S.-I. Akasofu, and W. J. Heikkila, "The Latitudinal Morphology of 10 eV to 10 keV Electron Fluxes During Magnetically Quiet and Disturbed Times in the 2100-0300 MLT Sector," J. Geophys. Res., 80, 3148, (1975).

## FIGURE LEGENDS

- 1 Contours of constant source density and characteristic energy in the  $\Sigma_H/\Sigma_P$  versus  $\Sigma_H$  plane. A Maxwellian velocity distribution of electrons at the source is assumed.
- 2 Pedersen and Hall conductances and their ratio as a function of  $j_z$  for electrons with Maxwellian source distributions of density 0.2 and  $2.0 \text{ cm}^{-3}$ .
- 3 Latitudinal variations of Hall and Pedersen conductance measured during 13 Triad satellite passes through the Region 2 evening sector current sheet.
- 4 Latitudinal variations of Hall and Pedersen conductance measured during seven Triad satellite passes through the Region 1 evening sector current sheet.
- 5 Latitudinal variations of Hall and Pedersen conductance measured during five Triad satellite passes through the Region 2 morning sector current sheet.
- 6 Hall to Pedersen conductance ratio as a function of Hall conductance measured within the Region 2 evening sector current sheet.
- 7 Hall to Pedersen conductance ratio as a function of Hall conductance measured within the Region 1 evening sector current sheet.
- 8 Hall to Pedersen conductance ratio as a function of Hall conductance measured within the Region 2 morning sector current sheet.
- 9 Electron density as a function of latitude and altitude measured during two radar elevation scans during Triad satellite passes. The arrows indicate the direction of the field-aligned currents determined from the Triad magnetometer data.

- 10 Hall to Pedersen ratio as a function of Hall conductance measured during the two scans of Figure 9. Data obtained in regions of upward current are shown by X's. Dots designate data obtained in downward current regions.
- 11 Electron spectra inferred from the electron density profiles along Lines A, B, and C in Figure 9. The dashed lines show the inferred spectra while the solid curves are Maxwellian spectra deduced from the Hall and Pedersen conductances.
- 12 Pedersen and Hall conductances and their ratio as a function of the field-aligned current density measured at the same invariant latitude by the Triad satellite during simultaneous passes. Data from the Region 2 morning and evening sector current sheets are shown.
- 13 Same as Figure 12 for the Region 1 current sheet. Only data from the evening sector were available.
- 14 Electron density as a function of latitude and altitude measured at two different times during a substorm on 22 January 1982.
- 15 Hall to Pedersen conductance ratio as a function of Hall conductance measured during the two radar scans shown in Figure 14.

Table 1  
 DATES AND TIMES OF SELECTED TRIAD  
 SATELLITE PASSES OVER CHATANIKA

Date	Magnetic Local Time
27 Oct. 1979	1824
20 Jan. 1980	0203
23 Feb. 1980	2245
24 Feb. 1980	2212
26 Feb. 1980	2250
29 Feb. 1980	2255
17 Apr. 1980	1908
09 May 1980	1725
17 Sept. 1980	2027
20 Sept. 1980	2030
07 Oct. 1980	1942
09 Oct. 1980	2018
10 Oct. 1980	1944
21 Nov. 1980	1709
10 Jan. 1981	0122
22 Jan. 1981	0133
23 Jan. 1981	0100
24 Jan. 1981	0030
26 Feb. 1981	2309
28 Feb. 1981	2204

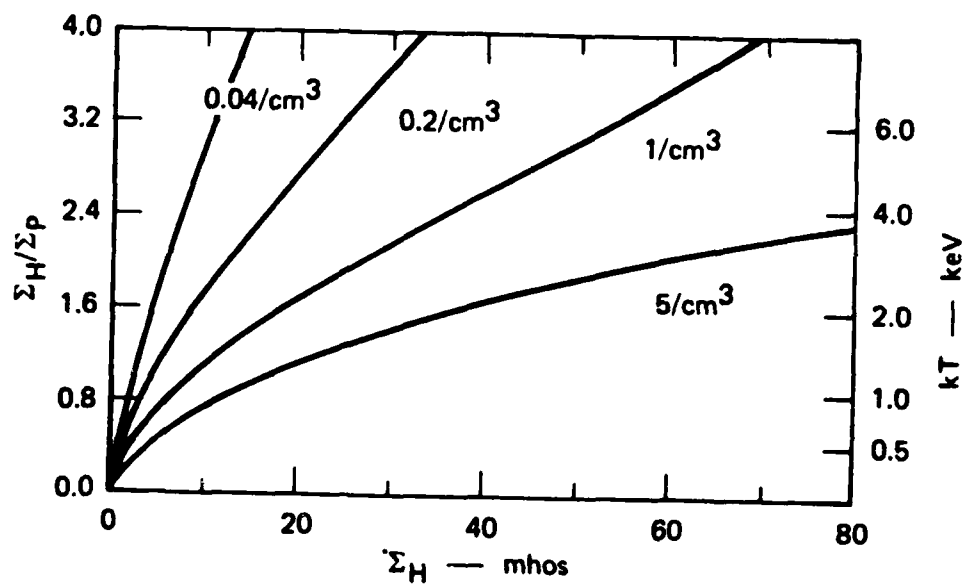


FIGURE 1

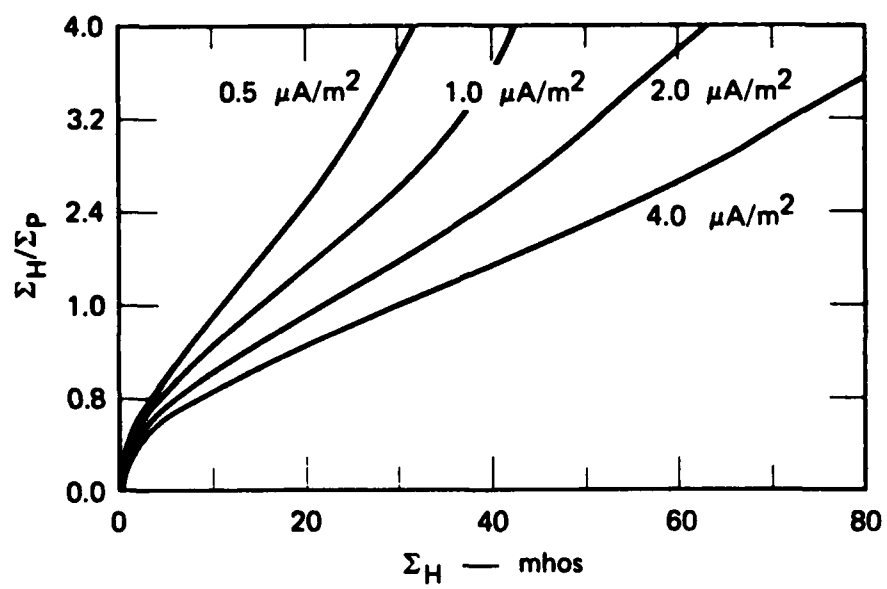


FIGURE 2



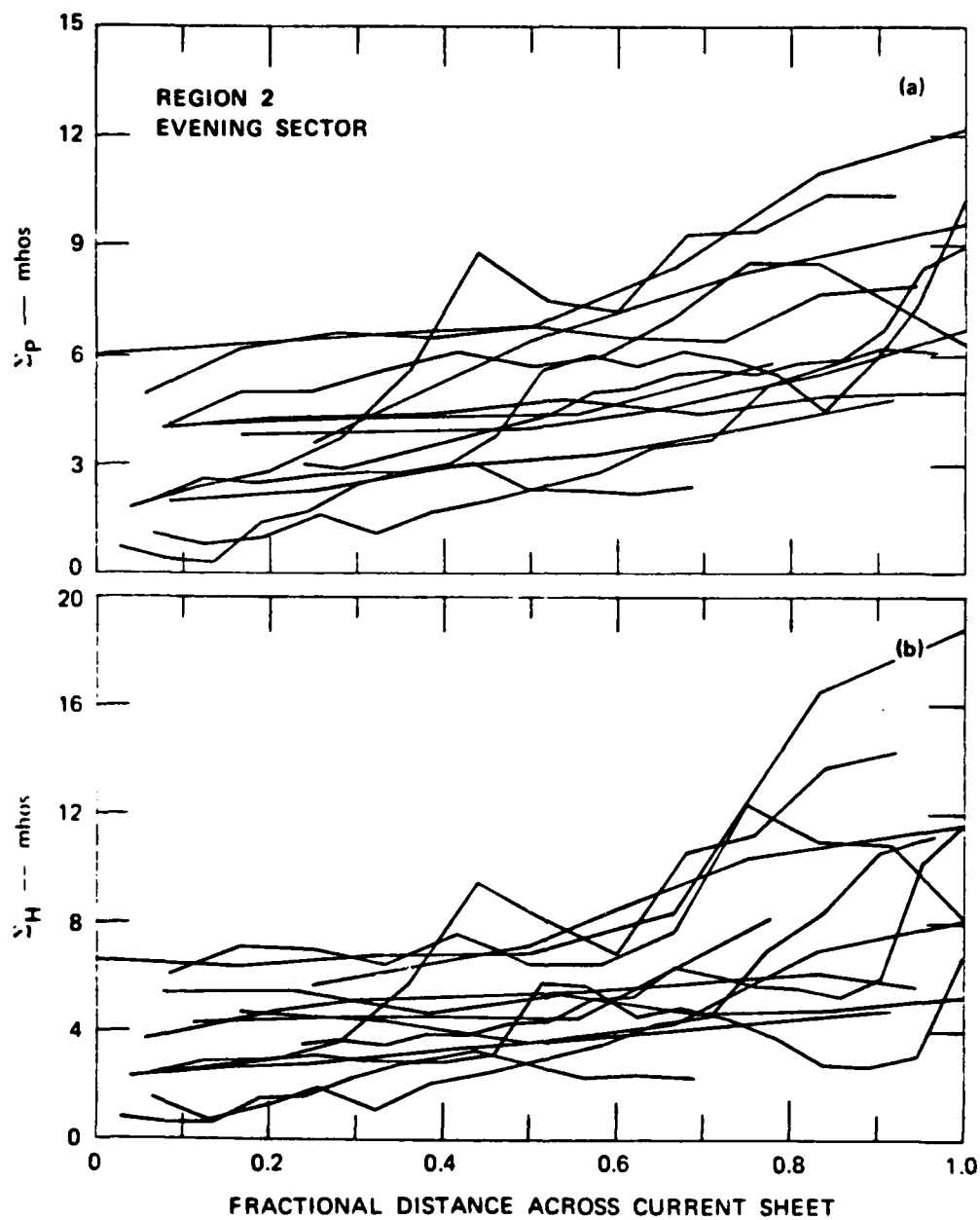


FIGURE 3

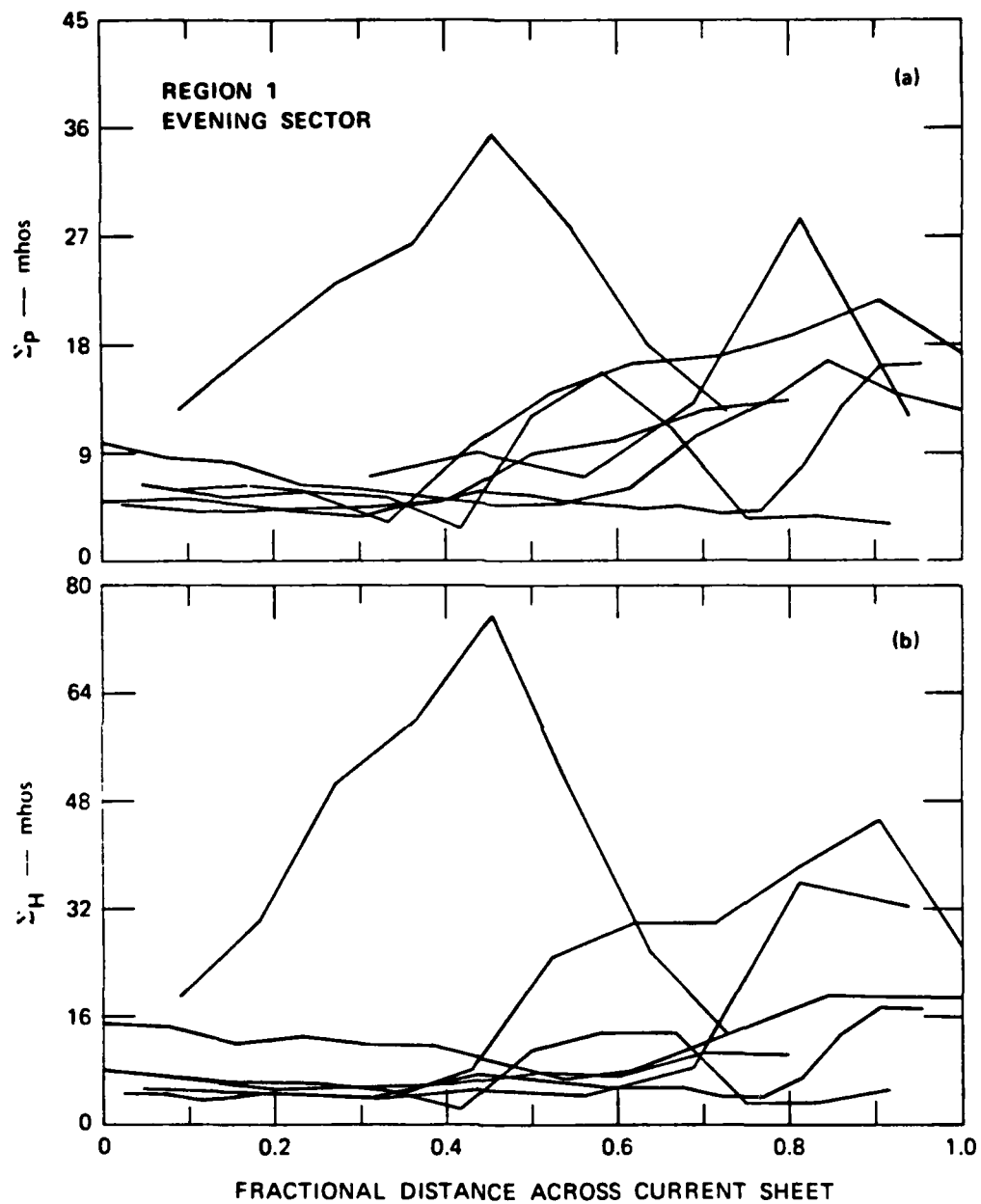


FIGURE 4

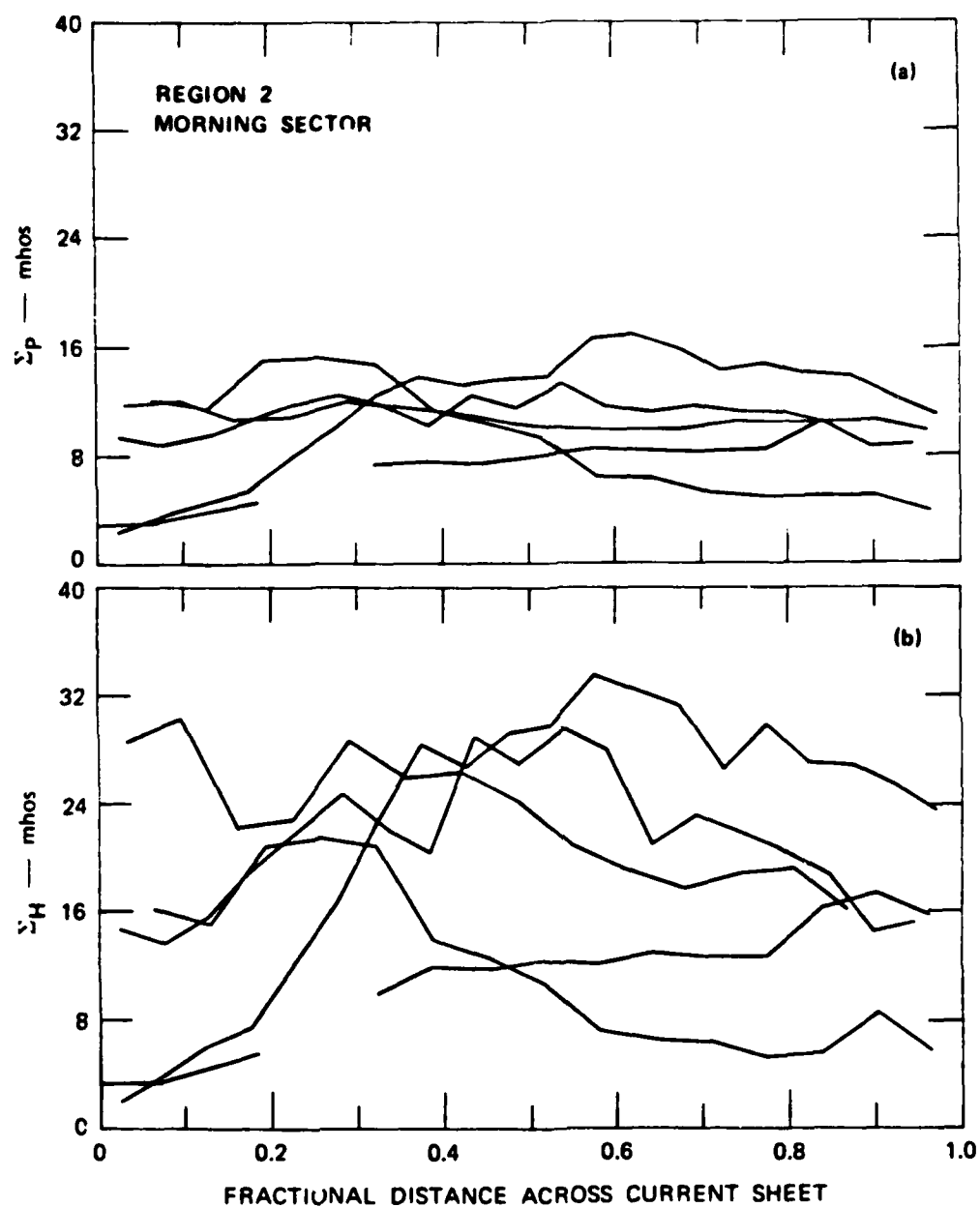


FIGURE 5

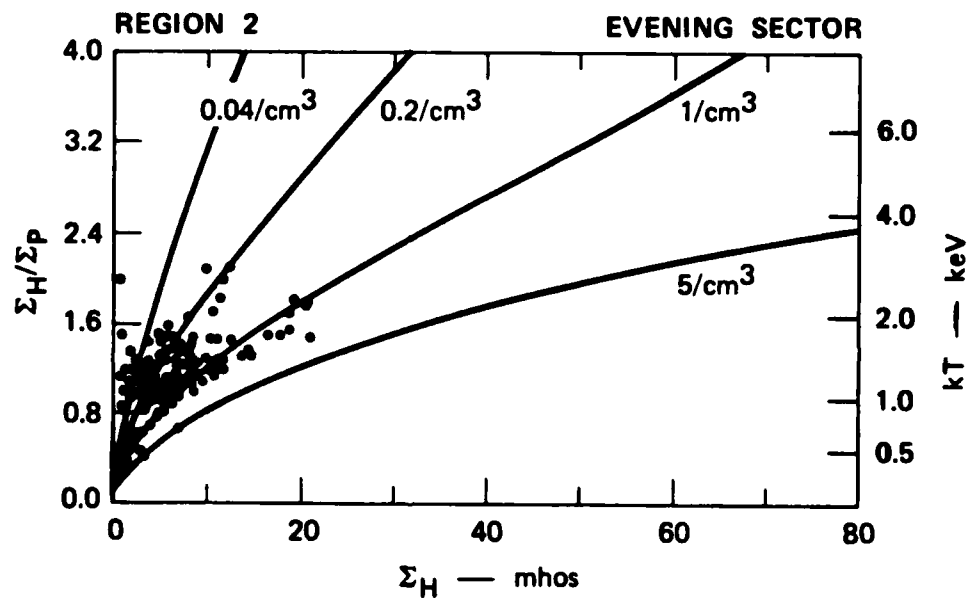


FIGURE 6

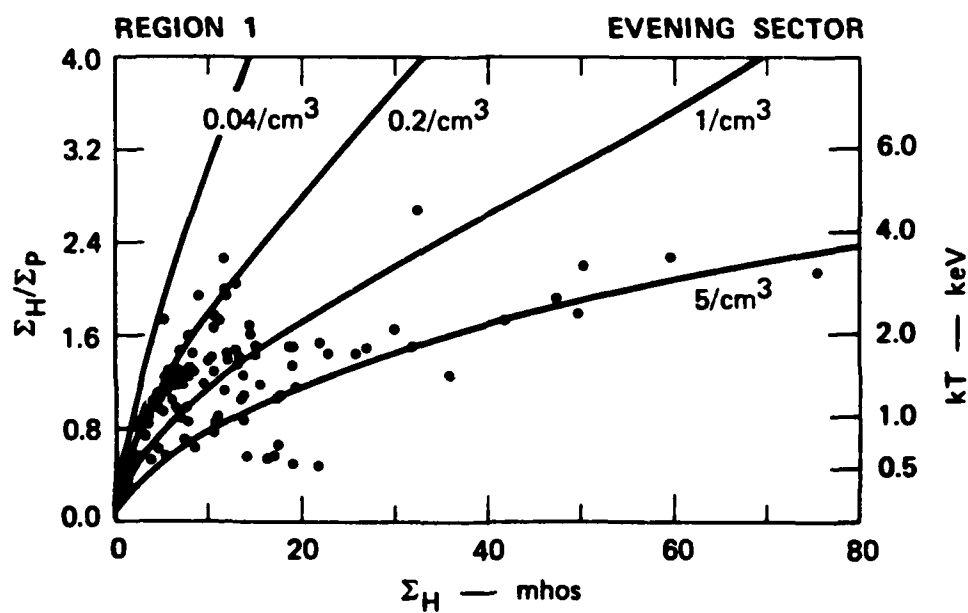


FIGURE 7

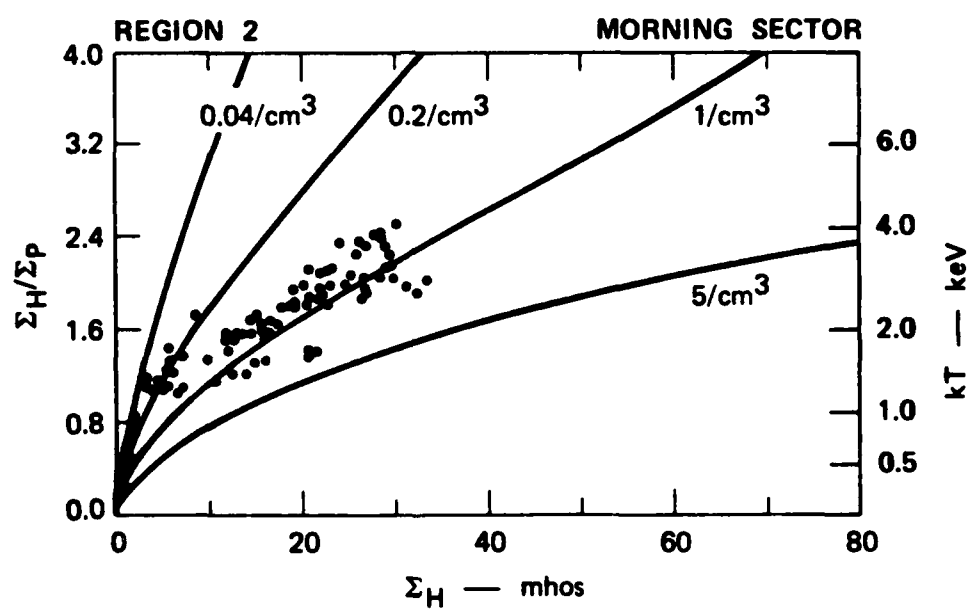


FIGURE 8

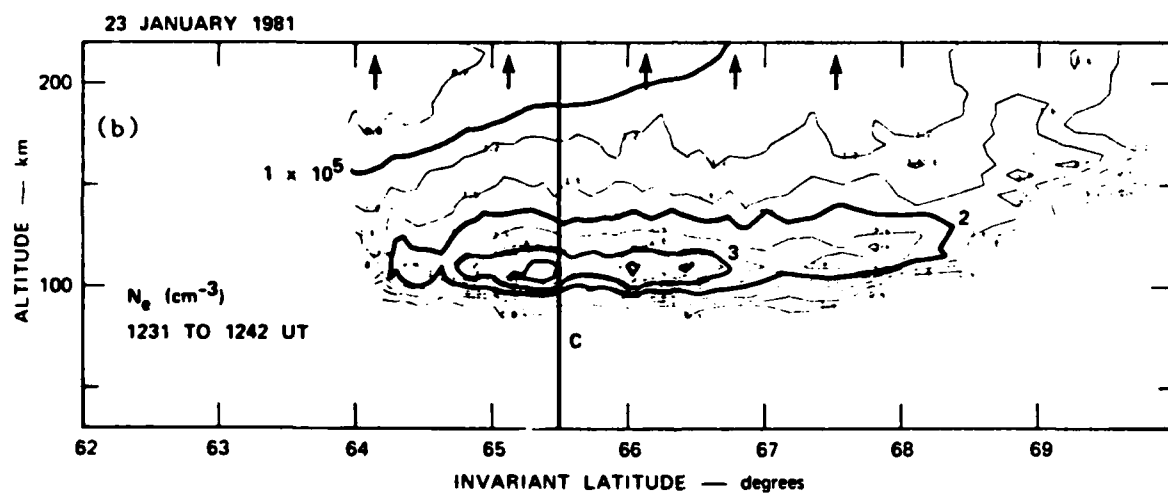
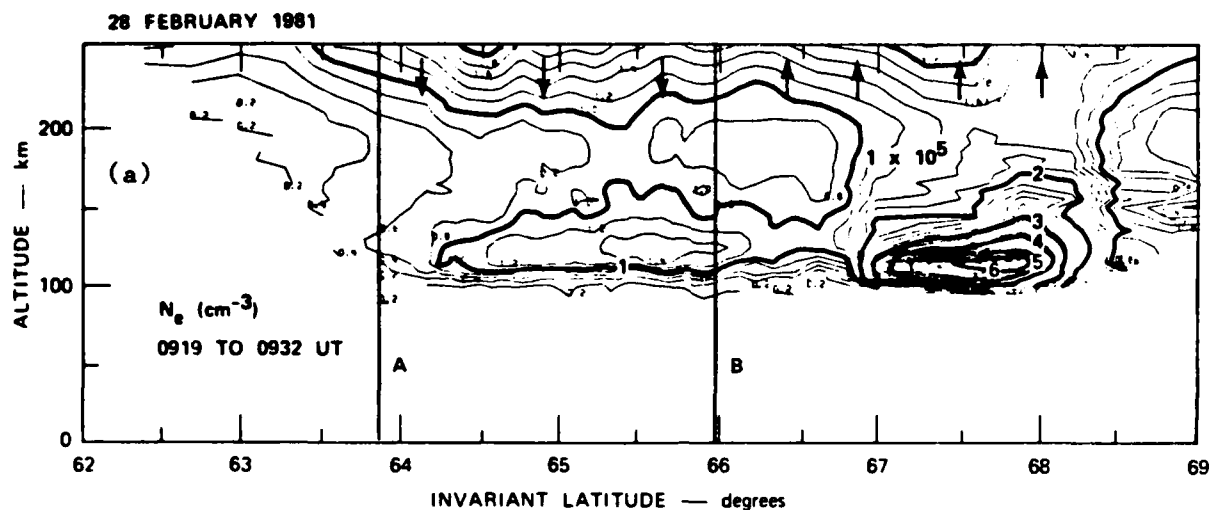


FIGURE 9

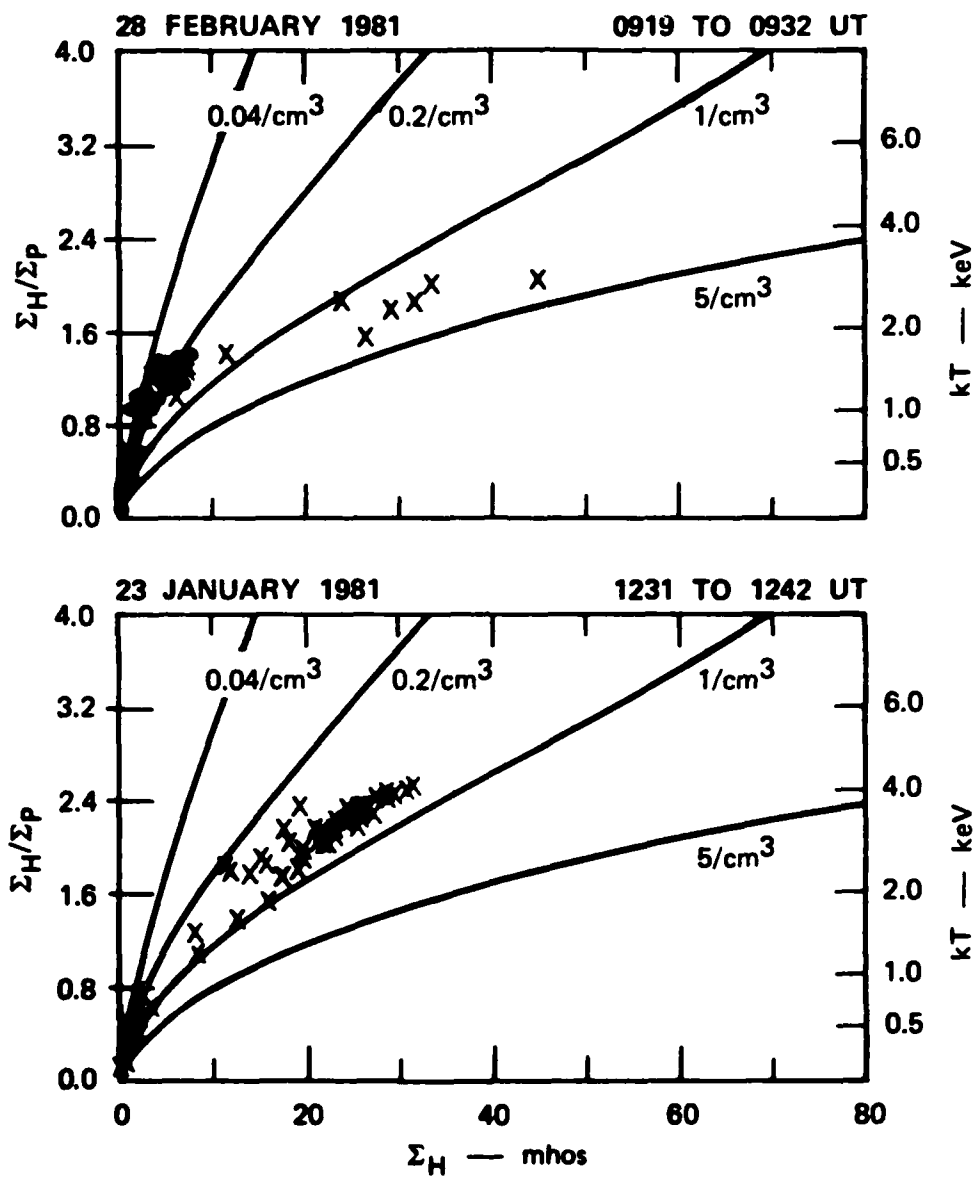


FIGURE 10



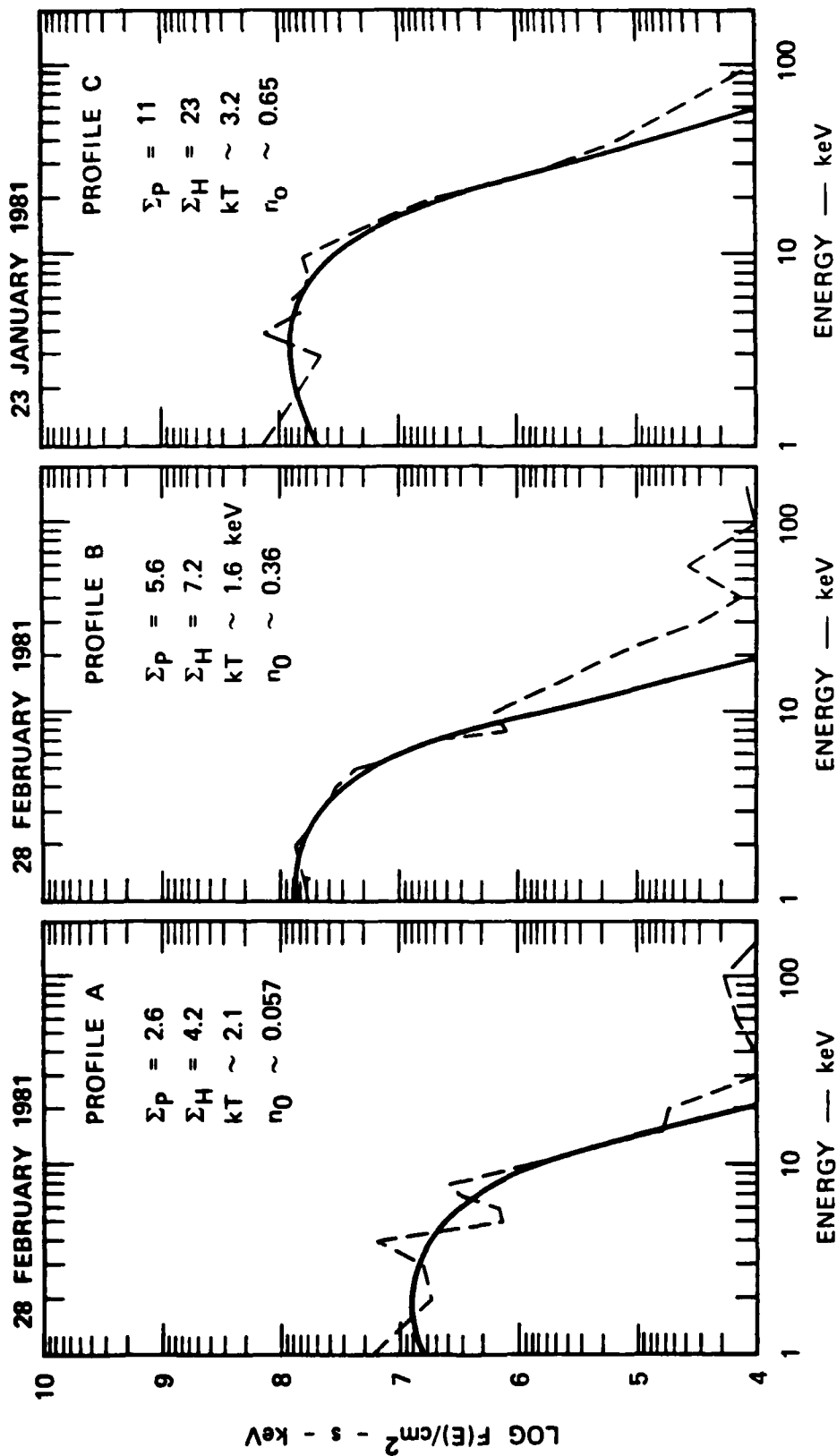


FIGURE 11

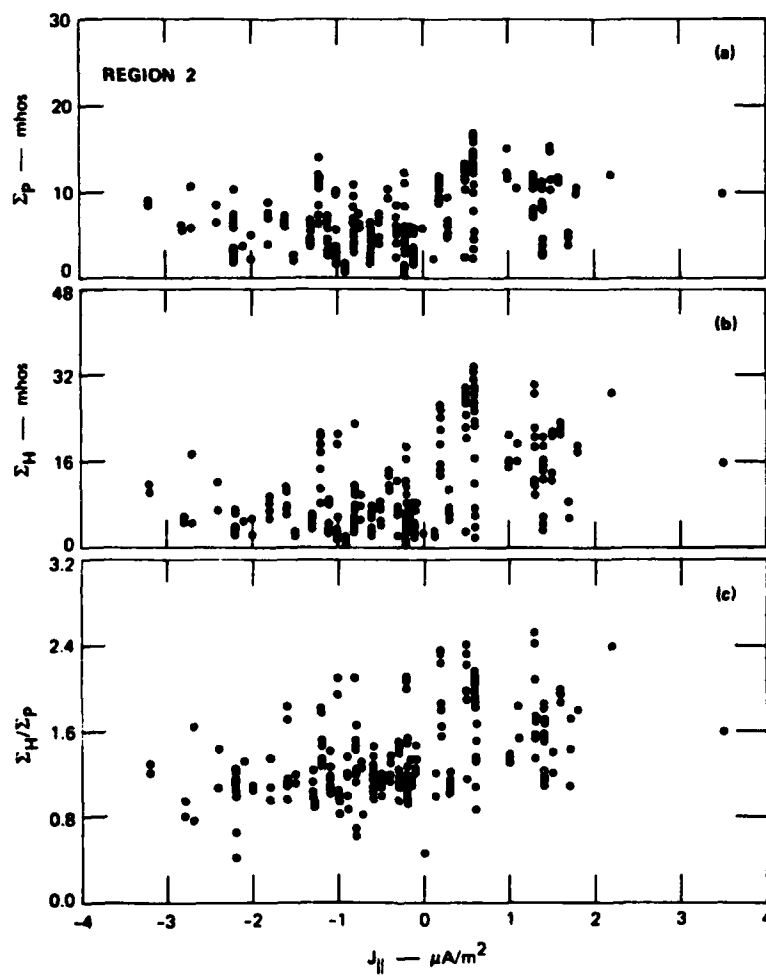


FIGURE 12

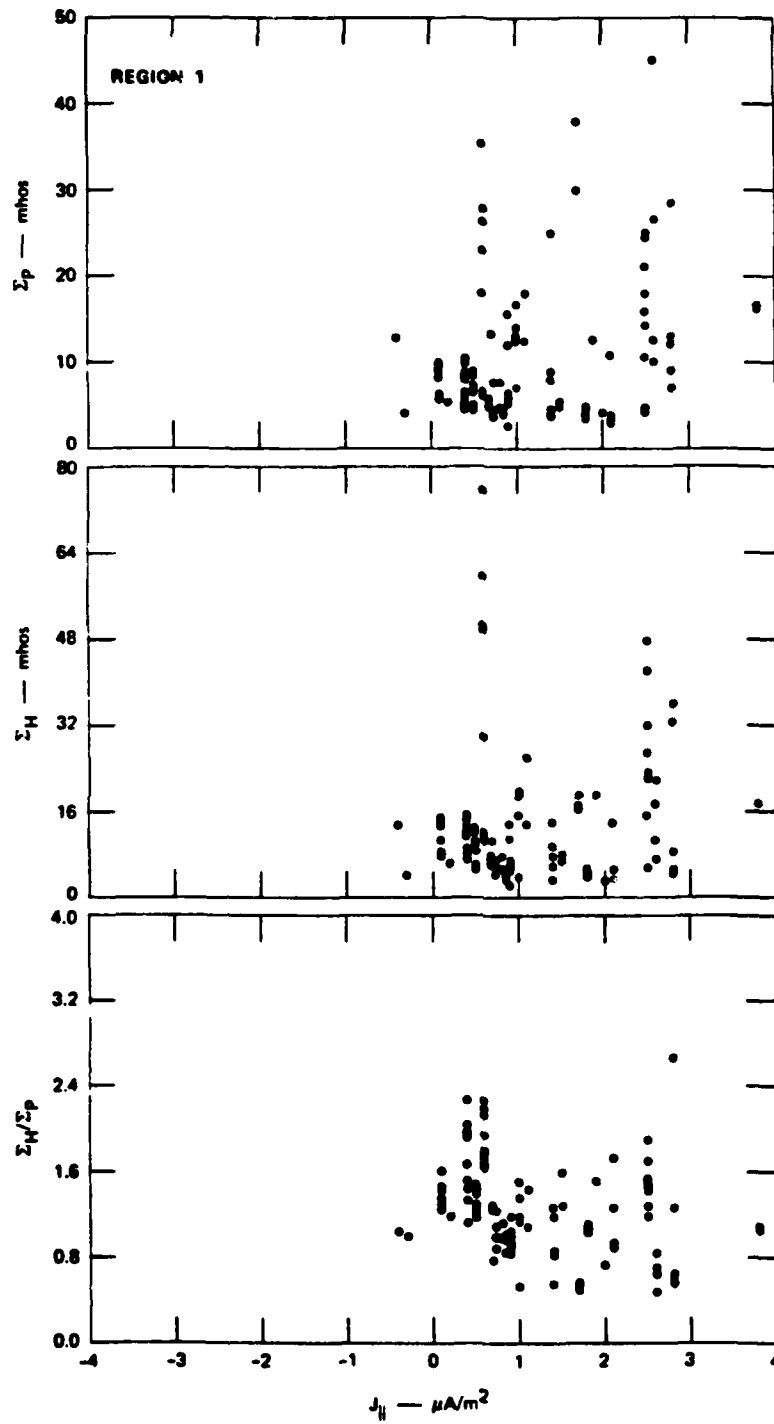


FIGURE 13

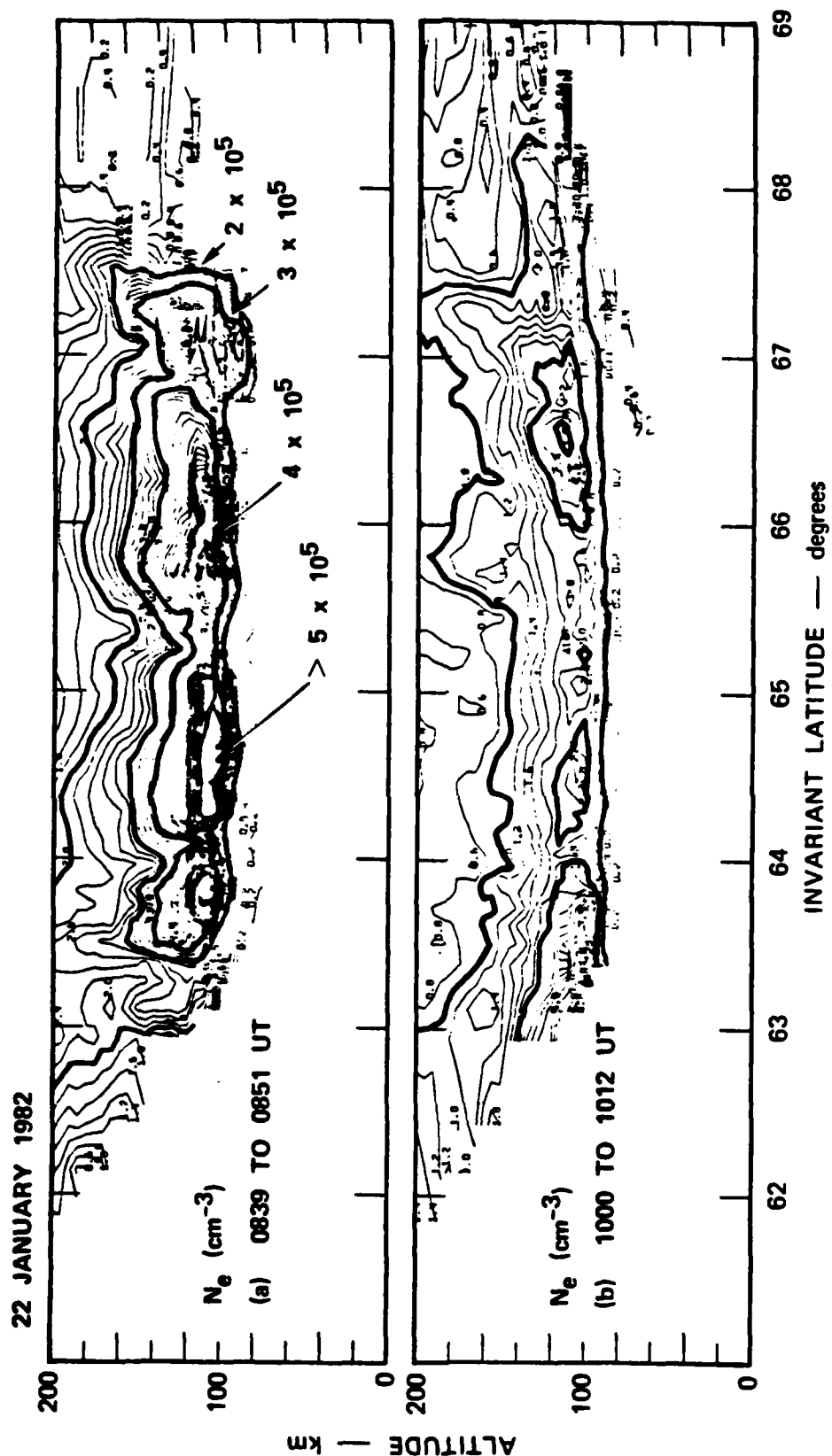


FIGURE 14

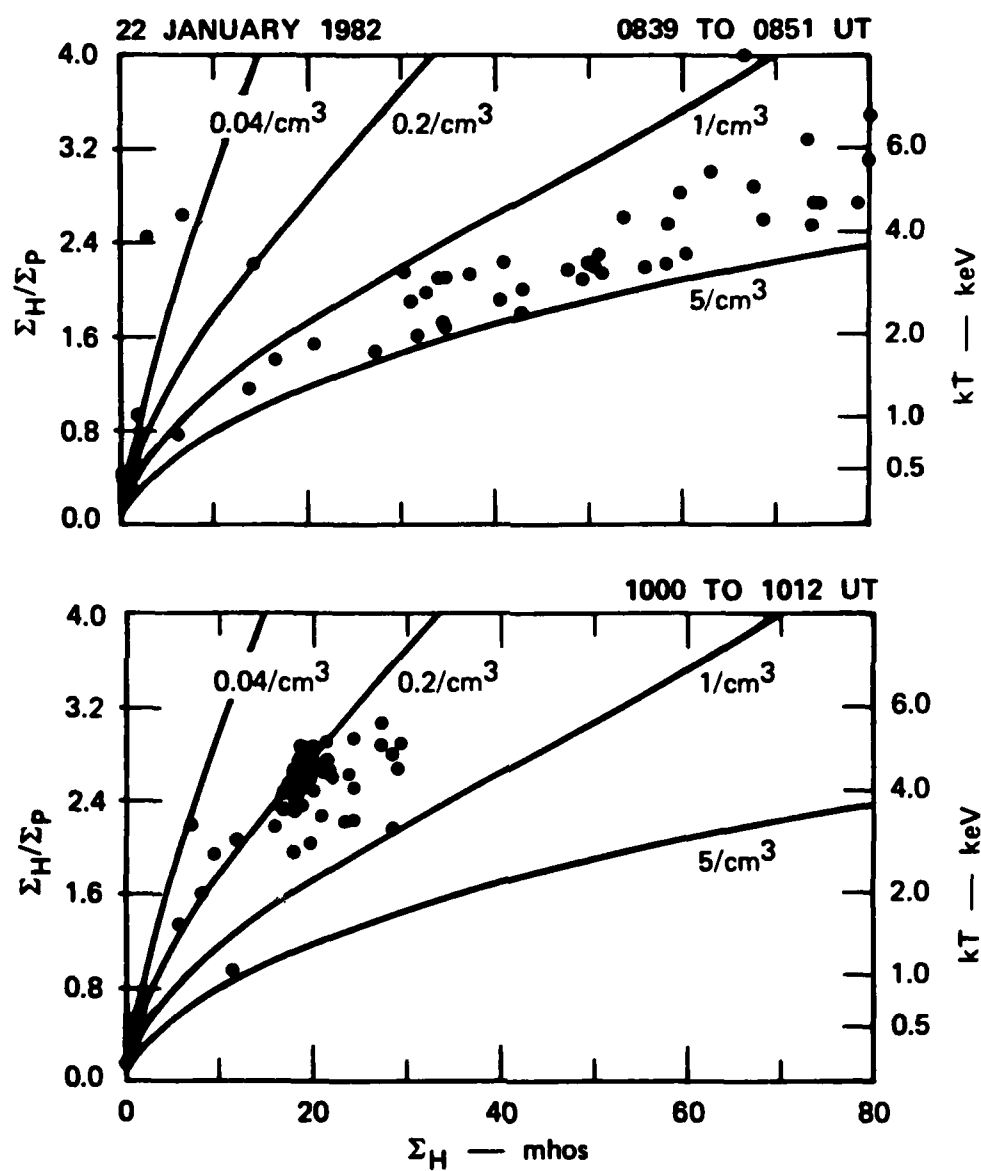


FIGURE 15

APPENDIX F

## Kp Dependence of Auroral Zone Field-Aligned Current Intensity

R. M. ROBINSON

SRI International, Radio Physics Laboratory

More than 200 hours of Chatanika radar elevation scan data have been used to show that the Pedersen current in the ionosphere is limited to a value that is proportional to the planetary magnetic index  $K_p$ . By assuming a simple model for the closure of field-aligned currents in the ionosphere, we argue that this limit is equal to the latitudinally integrated field-aligned current intensity. A least-squares fit to the data gives the limiting current intensity  $J_0$  by the following expression:  $J_0$  (A km) =  $97 + 71 \times K_p$ . As an extension of this result we use a previously derived relation between polar cap potential drop and  $K_p$  to establish a current-voltage relationship for the magnetospheric generator. We also show how these results can be used to put an upper limit on the Joule heating rate for a given polar cap potential drop.

## INTRODUCTION

Iijima and Potemra [1976] used magnetometer data from the Triad satellite to show that the average field-aligned current intensity almost doubled for measurements obtained when the  $AL$  index exceeded 100 nT. The intensity is defined as the field-aligned current density in A/m<sup>2</sup> integrated latitudinally across the region 1 or region 2 Birkeland current sheet. Because Reiff *et al.* [1981] showed that the  $AE$  index is correlated with the polar cap potential drop, the field-aligned current intensity increases with the polar cap potential drop. The polar cap potential drop is a good measure of the magnetospheric electric field that drives convection and, therefore, is analogous to the output voltage of a generator. The resulting field-aligned current represents the current driven by the magnetospheric generator.

In this paper we assume a very simple model for the field-aligned currents and use Chatanika radar measurements of electric field and conductivity to show how the field-aligned current intensity varies with  $K_p$ . As an extension of these results, we use the relation between polar cap potential drop and  $K_p$  found by Reiff *et al.* [1981] to derive a current voltage diagram for the magnetospheric generator.

The model we use is shown in Figure 1. We assume that the field-aligned currents flow in extended sheets that close by Pedersen currents in the ionosphere. Note that the field-aligned current in the sheets,  $J_0$  (in A km), is equal to the height-integrated Pedersen current in the region designated by  $B$ . We show this region extended in latitude when, in fact, the two current sheets are usually adjacent. In either case, measurements of the height-integrated Pedersen current in the ionosphere will produce values up to, but not exceeding,  $J_0$ . Measurements of the total current in the ionosphere are not sufficient to determine this quantity because the Hall component of the current is often much larger than the Pedersen current. Thus, for example, the maximum perturbation measured by ground-based magnetometers cannot be used to determine  $J_0$ . Similarly, field-aligned current measurements made by polar orbiting satellites may not be the same as the current generated in the magnetosphere because some of the field-aligned currents may be produced by gradients in the ionospheric Hall current. This contribution to the field-aligned

currents is nondissipative and does not necessarily connect to the magnetospheric generator.

In contrast to these techniques, measurements made by incoherent scatter radar can be used to measure  $J_0$  because both the Hall and Pedersen components of the total current in the ionosphere can be determined. Here we use measurements made by the Chatanika radar. The data set consists of measurements of conductivity and electric field made during more than 200 hours of elevation scan experiments. In the elevation scan mode, measurements are made over a latitudinal range of about 6°. The resolution of the measurements varies from 5 km to 30 km. The duration of each scan and the time between scans varied for these experiments. In the 200 hours of observations, approximately 800 scans were made. Each scan yielded 40 to 50 measurements of conductivity and electric field so that a total of about 35,000 measurements was available.

de la Beaujardiere *et al.* [1977] and Robinson *et al.* [1981] discuss the method by which vector electric fields are determined from ion drift measurements in the meridian plane. The ion drift  $V$  in the  $F$  region yields the east-west electric field directly according to

$$E_{EW} = -VB \quad (1)$$

The north-south electric field is given by

$$E_{NS} = \frac{V_1 B}{k_1} + \frac{k_2}{k_1} E_{EW} + B U_{EW} - \frac{(1 - k_2) U_{NS} B}{k_1} \quad (2)$$

where  $B$  is the magnetic field strength,  $k_1$  and  $k_2$  are Pedersen and Hall mobility coefficients weighted by the radar range gates and  $U_{EW}$  and  $U_{NS}$  are the two components of the  $E$  region neutral wind, assumed constant with altitude [de la Beaujardiere *et al.*, 1977].  $V_1$  is the  $E$  region ion drift measured by the radar along the same field line as the  $F$  region measurement. Because the  $E$  region neutral wind velocity is not measured, it is assumed to be negligible. The effects of this assumption on the measurements of Pedersen current are discussed below.

The uncertainty in the measurements of electric field depends to a large extent on the electron density in the  $E$  region. In this paper, we only show measurements of electric field with uncertainties less than 15 mV/m. In most cases, however, the uncertainties were between 5 and 10 mV/m. The 15 mV/m tolerance imposed on the measurements eliminated approximately 20% of the data.

Copyright 1984 by the American Geophysical Union.

Paper number 3A1702.  
0148-0227/84/003A-1702\$02.00

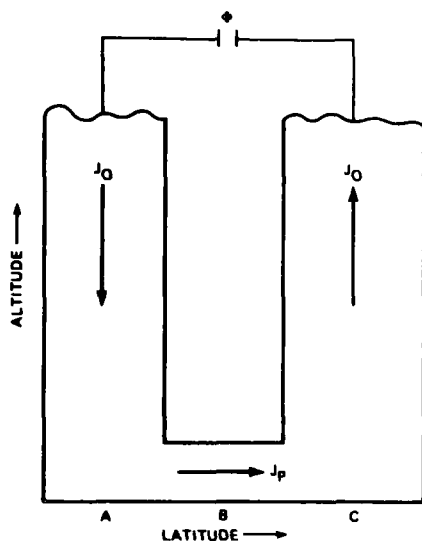


Fig. 1. Simplified model of field-aligned currents and their closure in the ionosphere. The current sheets, shown in cross-section, are assumed to extend along the auroral oval.

The height-integrated Pedersen current in the ionosphere is

$$\mathbf{J}_p = \Sigma_p(\mathbf{E} + \mathbf{U} \times \mathbf{B}) \quad (3)$$

where  $\Sigma_p$  is the Pedersen conductance and  $\mathbf{U}$  is the neutral-wind velocity, assumed constant over the altitude range where  $\Sigma_p$  is significant (100 to 160 km). In our model of field-aligned currents the closing currents are mostly northward. The northward Pedersen current is

$$J_{Ns} = \Sigma_p E_{Ns} - \Sigma_p U_{EW} B \quad (4)$$

Using (2) in (4), we find that the northward Pedersen current does not depend on the east-west component of the neutral wind. The coefficients  $k_1$  and  $k_2$  are such that a northward velocity of 100 m/s produces an error in the electric field measurement of about 15 mV/m insofar as the effect on Pedersen current is concerned. Typical  $E$  region neutral wind velocities are smaller than this [Brekke et al., 1973].

#### RESULTS

Figure 2 is an example of the type of data used in this paper. The horizontal axis is the height-integrated Pedersen conductivity and the vertical axis is the north-south electric field. Because of the orientation of the field-aligned currents sheets we expect that most of the current will be driven by geomagnetically north- or south-directed electric fields. The data in Figure 2 represent measurements made between 0551 and 1400 UT on 22 January 1982. Immediately apparent is that the electric field, either northward or southward, is small when the conductivity is large. This behavior has been noted by many observers and has been attributed to polarization charges that accumulate at the edges of regions of enhanced conductivity. de la Beaujardiere et al. [1977] suggested that in the morning sector, the Hall currents driven by westward electric fields may act to neutralize these polarization charges and at times create large electric field in enhanced conductivity strips. This behavior is not apparent in Figure 2. The anticorrelation between  $E$  and  $\Sigma_p$  occurs both in the evening (northward electric field) and morning (southward electric

field) sectors. In the figures that follow, we will not show the northward and southward components of the electric fields. Instead, we will show only the magnitude of the electric field as a function of Pedersen conductivity.

The envelope of the points in Figure 2 is approximately a hyperbola so that we can write for the height-integrated horizontal Pedersen current

$$\Sigma_p E \leq J' \quad (5)$$

where  $J'$  is about 400 A/km. Recalling the model in Figure 1 we conclude that on this particular day the intensity of the field-aligned current directly driven by the magnetospheric generator never exceeded about 400 A/km.

Similar data from two other elevation scan experiments are shown in Figure 3. The data in Figure 3a were obtained during a three-hour interval during which the planetary magnetic index  $Kp$  was 3. The data in Figure 3b were obtained during a 24-hour experiment. During these 24 hours,  $\Sigma Kp$  was 41. A reference curve given by the equation  $\Sigma_p E = 350$  A/km is drawn in both plots. In these plots, it is clear that the envelope of the data can be fitted to a hyperbola. However, the product  $\Sigma_p E$  has significantly larger values for the more active day. To enclose the data in Figure 3b requires a function given by  $\Sigma_p E \approx 600$  A/km, while to enclose the data in Figure 3a requires the function  $\Sigma_p E \approx 350$  A/km. The data in Figure 2 were obtained when  $Kp$  varied between 3 and 4 and the envelope of the points is about  $\Sigma_p E \approx 400$  A/km. These examples suggest that the limiting Pedersen current depends on world-wide magnetic activity as reflected by the  $Kp$  index.

At first, this may not seem too surprising. However, as pointed out above, indices such as  $Kp$  based on ground mag-

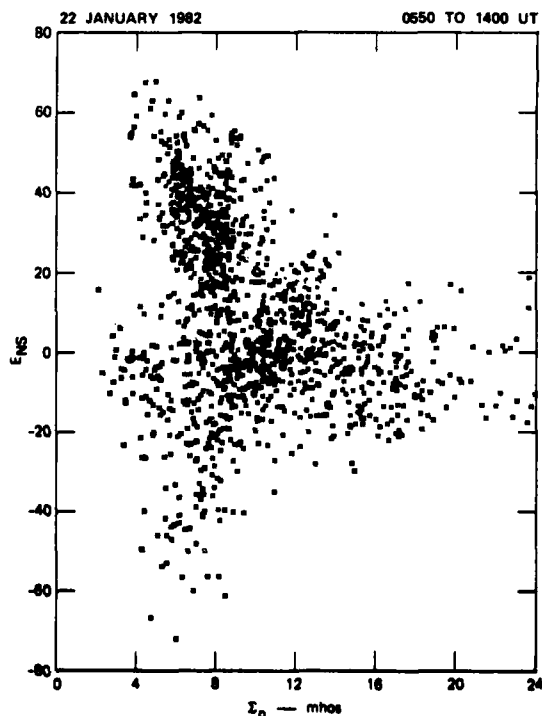


Fig. 2. Plot of Chatanika radar measurements of electric field as a function of height-integrated Pedersen conductivity on February 22, 1982.



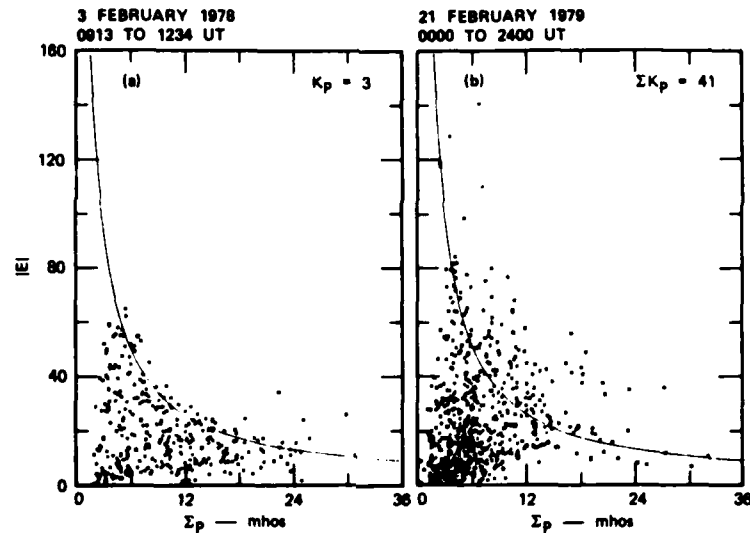


Fig. 3. Electric field as a function of Pedersen conductivity during elevation scan experiments on (a) February 3, 1978 and (b) February 21, 1979.

netometer data are influenced overwhelmingly by the Hall current. For characterizing the magnetospheric generator, the Pedersen current is more important. In addition, we are relating a local measurement of the Pedersen current to a global magnetic index. Thus a priori the trend shown in Figures 2 and 3 would not be expected.

To illustrate this trend further, we use the 200 hours of elevation scan measurements to determine the magnitude of the limiting current as a function of  $K_p$ . In Figure 4, we plot

$\Sigma_p$  as a function of  $E$  with the data sorted according to  $K_p$ . The number of data points in each  $K_p$  category is given at the top of the figure. In each case, it is apparent that the electric field is limited to a value that depends on the conductivity, the envelopes being approximately hyperbolas. The hyperbolas shown in Figure 4 were chosen to contain 95% of the data.

We illustrate the distribution of data in Figure 4 more quantitatively in Figure 5, which shows the fraction of data with values less than any given value of  $\Sigma_p E$ . For the present

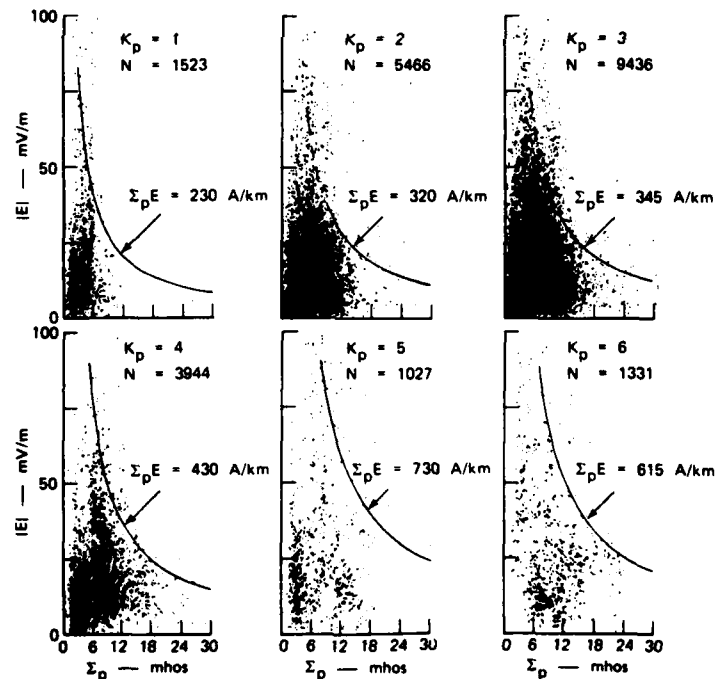


Fig. 4. Electric field magnitude versus height-integrated Pedersen conductivity sorted by  $K_p$ . The number of data points in each plot is given by  $N$ . The hyperbolas were drawn to contain 95% of the data.

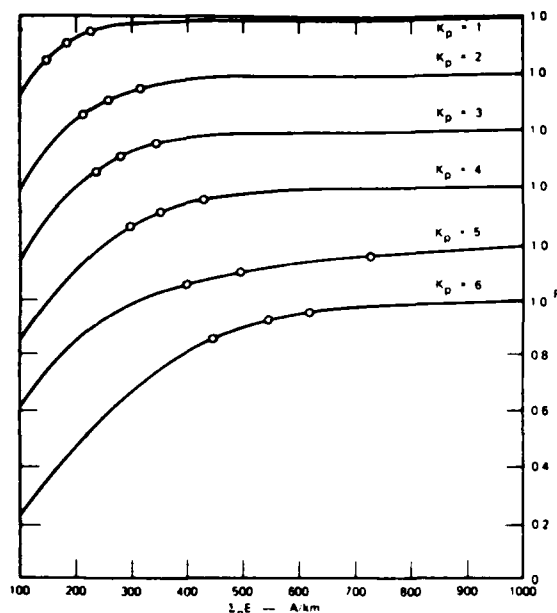


Fig. 5. The fraction  $F$  of data above any given value of  $\Sigma_p E$  for six  $K_p$  intervals. The circles indicate the currents below which 85, 90, and 95% of the measurements were contained.

purposes, we shall assume that the limit of the Pedersen current for each  $K_p$  interval is defined by the current below which 90% of the points are found. The uncertainty in the limit found in this way we define as the difference in the limit when the percentage varies by 5% in either direction. The 85%, 90%, and 95% values for each  $K_p$  interval are designated by circles in Figure 5.

In Figure 6 we plot these values as a function of  $K_p$ . The solid line is a linear least-squares fit through the data. In performing the fit, the data were weighted by the lengths of the bars in the figure. Note that the lengths of the bars are inversely related to the number of data points in each  $K_p$  bin.

The results in Figure 6 show that the maximum Pedersen current measured in the ionosphere increases approximately linearly with  $K_p$ . When this information is considered in relation to the model in Figure 1, we conclude that the change in the maximum Pedersen current results from the increase in the intensity of field-aligned currents. Note that this increase in intensity can result from an increase in field-aligned current density over part or all of the current sheet or simply a broadening of the current sheet with no change in current density. In either case, it represents an increase in the total current generated by the magnetospheric dynamo.

#### DISCUSSION

We have shown in Figure 6 that the magnitude of the ionospheric Pedersen current is statistically less than some value that depends on  $K_p$ . The least-squares fit to the data in Figure 6 is given by the following expression

$$(\Sigma_p E)_{\max} (\text{A/km}) = 97 + 71 \times K_p \quad (6)$$

Using a very simple model of field-aligned currents, we argue that this maximum Pedersen current is approximately equal to the intensity of the field-aligned currents. Thus the intensity of field-aligned currents  $J_0$  is related to  $K_p$  according to

$$J_0 (\text{A/km}) = 97 + 71 \times K_p \quad (7)$$

This result can be compared to that of *Iijima and Potemra* [1976] who used Triad magnetometer data to study the dependence of field-aligned current intensity on magnetic activity. For  $K_p$  between 2- and 4+ the average region 1 field-aligned current intensity is 300 A/km in the afternoon to midnight local time sector and 250 A/km in the midnight to forenoon local time sector. We use the region 1 values for this comparison because they are presumably the currents that are driven directly by the magnetospheric generator. The field-aligned current intensity determined by *Iijima and Potemra* [1976] for this  $K_p$  range agrees very well with that given by (7). For  $K_p = 3$ , (7) gives  $J_0 = 310$  A/km, slightly higher than the Triad results.

The good agreement with *Iijima and Potemra* [1976] is encouraging, especially considering the simplicity of our model. For example, the model contains the assumption that all the field-aligned currents close meridionally between the two sheets. In reality, some of the current may close zonally along the length of the sheet or meridionally into the polar cap. In these cases, the maximum ionospheric Pedersen current will be less than the field-aligned current intensity.

We also assumed in our model that the intensity of the field-aligned currents is independent of local time. Because Chatanika usually lies equatorward of the auroral zone during the daylight hours, the data are heavily weighted toward the evening and early morning sectors; therefore, the results in Figure 6 may not apply to the dayside field-aligned currents.

In addition to these problems a number of factors make the maximum Pedersen current expressed in (6) a poorly defined quantity. As discussed earlier, the radar electric field measurements have uncertainties up to 15 mV/m and the presence of

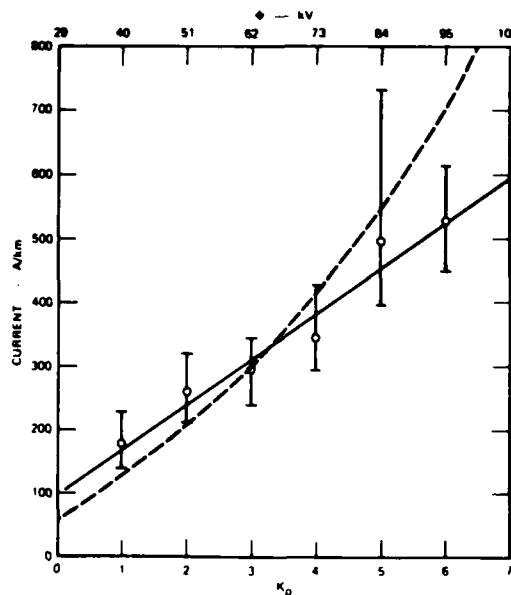


Fig. 6. The limiting Pedersen current in the ionosphere as a function of  $K_p$ . The circles represent the current below which 90% of the data were contained. The upper and lower extents of the error bars represent the currents below which 85 and 95% of the data were contained, respectively. The upper scale shows the value of the polar cap potential drop as deduced by *Reiff et al.* [1981]. The straight line is a weighted, linear least-squares fit to the six data points. The dashed curve represents a quadratic dependence of current on potential drop forced to agree for  $K_p = 3$ .

$E$  region neutral winds can result in comparable errors. In addition, the calculation of current requires the Pedersen conductivity, which depends on the ion-neutral collision frequency. This may be in error by as much as 30%. We chose to use the current that contained 90% of the data to take these effects into account. The error bars in Figure 6 reflect the resulting uncertainties in the maximum current so derived.

Even when these uncertainties are taken into account,  $\Sigma_p E$  often exceeds the limits defined by the hyperbolas in each  $Kp$  bin by rather large amounts. Many of these deviations are probably due to the 3-hour temporal resolution of the  $Kp$  index. However, in looking at the data more closely, we found that for about half of the cases where the Pedersen currents exceeded the limit, the east-west electric field was large (greater than 10 mV/m). The large east-west electric field definitely indicates that the simple model for field-aligned currents shown in Figure 1 may no longer be valid. An additional field-aligned current system may also be present. One possibility is that a substorm type field-aligned current system exists in which field-aligned currents connect to the ends of a substorm-associated westward electrojet. It is not clear, in this case, that the Pedersen current is limited to any definite value.

We can take the results in Figure 6 one step further by using the correlation between  $Kp$  and polar cap potential drop  $\Phi_0$  found by Reiff *et al.* [1981]. Using this relation, we can write (7) as

$$J_0(A/km) = 6.5 \times \Phi_0 - 90 \quad (8)$$

Equation (8) relates the polar cap potential drop to the resulting field-aligned current intensity. The polar cap potential drop as a function of  $Kp$  is given by the upper scale in Figure 6.

By interpreting our results in this manner we imply that for a given polar cap potential drop (or magnetospheric electric field), a unique field-aligned current intensity will result from the output of the magnetospheric dynamo. However, Fujii *et al.* [1981] analyzed Triad satellite magnetometer data and showed that statistically the field-aligned current intensity in the summer hemisphere is double that in the winter hemisphere. This is presumably due to the enhanced conductivity over the polar regions produced by solar EUV. The higher conductance results in a larger output current for a given applied voltage. Because our data were obtained during the winter the results in Figure 6 apply to the nonsunlit hemisphere only.

If such a dependence on overall conductance exists, we may argue that no unique current results from a given driving potential because the conductance produced by precipitating particles may vary for a given level of magnetic activity. However, several statistical studies of auroral zone conductance as a function of magnetic activity indicate that the magnitude and spatial distribution of auroral precipitation is fairly well defined for a given level of activity [Wallis and Budzinski, 1981; Spiro *et al.*, 1982]. Thus, only when an additional source of ionization is present such as solar EUV will the conductance increase enough to affect the resulting field-aligned current intensity.

The results in Figure 6 can be used to test proposed mechanisms for driving the field-aligned currents. For example, Rostoker and Bostrom [1976] have suggested a mechanism in which field-aligned currents are created by the deceleration of the radial component of plasma drift away from the earth-sun line. They predict a field-aligned current intensity given by

$$J_0 = A\Phi_0^2 \quad (9)$$

where  $A$  is a constant that depends on the geometry and magnitude of the field lines in the magnetotail and the mass density in the plasma sheet. In Figure 6, we have shown this function using a value of  $A$  such that the theoretical results equal the experimental results for  $Kp = 3$ . The quadratic dependence of  $J_0$  on  $\Phi_0$  is not clearly apparent in the data in Figure 6. There is a suggestion that the current increases more rapidly than the linear relationship for  $Kp = 5$ . The method we have used to determine  $J_0$  gives only a lower bound to the current. For  $Kp = 6$  the auroral oval may possibly have been expanded to such an extent that the radar did not sample the region of maximum Pedersen current. In addition, the quadratic dependence may be concealed because the correlation between  $Kp$  and polar cap potential found by Reiff *et al.* [1981] used a linear fit to the data. Note that the model of Rostoker and Bostrom [1976] implies a rather severe dependence of the current generated on local time away from midnight. This dependence on local time is not apparent in our data. In spite of this, it is interesting to note that the theoretically derived current-voltage relationship agrees well with the data even though no changes in the geometry and magnitude of the tail magnetic field with  $Kp$  are included in the model. Thus the observed changes in potential drop and field-aligned current intensity can be accommodated by a change in convection velocity alone.

As a further application of the results in Figure 6, we can estimate the maximum amount of Joule heating to be expected for any  $Kp$  value. The total Joule heat input  $Q_J$  between latitudes  $\lambda_1$  and  $\lambda_2$  is

$$Q_J = \int_{\lambda_1}^{\lambda_2} \Sigma_p E^2 d\lambda \quad (10)$$

Using the results of Figure 6, we can write

$$\Sigma_p E \leq J_0(Kp) \quad (11)$$

where  $J_0$  is the current plotted in the figure. Thus

$$Q_J \leq J_0(Kp) \int_{\lambda_1}^{\lambda_2} E d\lambda \quad (12)$$

$$Q_J \leq J_0(Kp)\Phi_{12}$$

where  $\Phi_{12}$  is the potential drop between  $\lambda_1$  and  $\lambda_2$ . If  $\lambda_1$  and  $\lambda_2$  bound the auroral zone,  $\Phi_{12}$  is approximately half the polar cap potential drop. The maximum Joule heating along any meridian is then

$$Q_{Jmax} = J_0(Kp)\Phi_0/2 \quad (13)$$

Using (8), this becomes

$$Q_{Jmax}(mW/km) = 1/2(6.5\Phi_0^2 - 90\Phi_0) \quad (14)$$

Thus for  $\Phi_0 \gg 15$  kV, the maximum Joule heating rate increases as the square of the polar cap potential. Assuming a circular auroral zone with a circumference of 16,000 km, (14) gives a power input between  $10^{11}$  and  $10^{12}$  W for  $\Phi_0 > 50$  kV. This estimate of the maximum Joule heating rate agrees with the estimate of Banks *et al.* [1981] based on an independent study using Chatanika radar data.

#### SUMMARY

We have used Chatanika radar measurements of electric field and conductivity to derive a relationship between the magnetic activity index  $Kp$  and the auroral zone field-aligned current intensity. When separated according to  $Kp$  the Pedersen current in the ionosphere is less than or equal to some

maximum current. We assume a simple model for field-aligned currents to show that this maximum current is equal to the intensity of the field-aligned currents generated in the magnetosphere. Because  $K_p$  is correlated with the polar cap potential drop, the current generated in the magnetosphere can be related to the applied voltage. We also use these results to estimate the maximum Joule heating rate as a function of  $K_p$ .

**Acknowledgments.** The author benefited from helpful discussions with Roland Tsunoda and Richard Vondrak. Bernice Bumbaca provided valuable programming assistance. The site crew of the Chatanika radar operated the radar during the experiments. This work was supported by the Air Force Office of Scientific Research under contract F49620-80-C-0014, the Defense Nuclear Agency under contract DNA001-83-C-0034, and the National Science Foundation under grant ATM78-23658.

The Editor thanks the two referees for their assistance in evaluating this paper.

#### REFERENCES

- Banks, P. M., J. C. Foster, and J. R. Doupnik, Chatanika radar observations relating to the latitudinal and local time variations of Joule heating, *J. Geophys. Res.*, **86**, 6869, 1981.
- Brekke, A., J. R. Doupnik, and P. M. Banks, A preliminary study of the neutral wind in the auroral  $E$  region, *J. Geophys. Res.*, **78**, 8235, 1973.
- de la Beaujardiere, O., R. Vondrak, and M. Baron, Radar observations of electric fields and currents associated with auroral arcs, *J. Geophys. Res.*, **82**, 5051, 1977.
- Fujii, R., T. Iijima, T. A. Potemra, and M. Sugiura, Seasonal dependence of large-scale field-aligned currents, *Geophys. Res. Lett.*, **8**, 1103, 1981.
- Iijima, T., and T. A. Potemra, The amplitude distribution of field-aligned currents at northern high latitudes observed by Triad, *J. Geophys. Res.*, **81**, 2165, 1976.
- Reiff, P. H., R. W. Spiro, and T. W. Hill, Dependence of polar cap potential drop on interplanetary parameters, *J. Geophys. Res.*, **86**, 7639, 1981.
- Robinson, R. M., E. A. Bering, R. R. Vondrak, H. R. Anderson, and P. A. Cloutier, Simultaneous rocket and radar measurements of currents in an auroral arc, *J. Geophys. Res.*, **86**, 7703, 1981.
- Rostoker, G., and R. Bostrom, A mechanism for driving the gross Birkeland current configuration in the auroral oval, *J. Geophys. Res.*, **81**, 235, 1976.
- Spiro, R. W., P. H. Reiff, and L. J. Maher, Jr., Precipitating electron energy flux and auroral zone conductances—An empirical model, *J. Geophys. Res.*, **87**, 8215, 1982.
- Wallis, D. D., and E. E. Budzinski, Empirical models of height-integrated conductivities, *J. Geophys. Res.*, **87**, 125, 1981.
- R. M. Robinson, SRI International, Radio Physics Laboratory, 333 Ravenswood Avenue, Menlo Park, CA 94025.

(Received May 9, 1983;  
revised October 20, 1983;  
accepted October 21, 1983.)

END

FILMED

8

24